

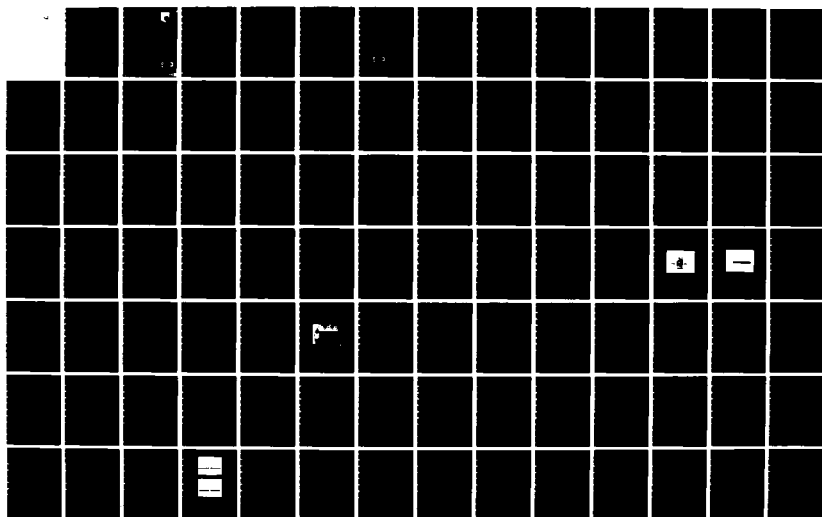
AD-A142 462

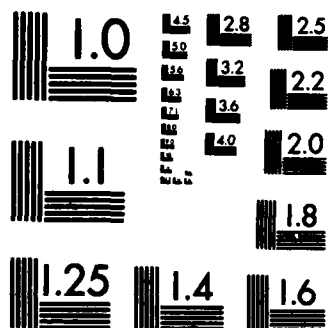
LARGE-SIGNAL CHARACTERIZATION OF NONLINEAR TWO-PORT
ACTIVE NETWORKS(U) MICHIGAN UNIV ANN ARBOR ELECTRON
PHYSICS LAB D C YANG APR 84 TR-163 AFWAL-TR-84-1034
F33615-81-K-1429 F/G 9/5

1/2

UNCLASSIFIED

NL



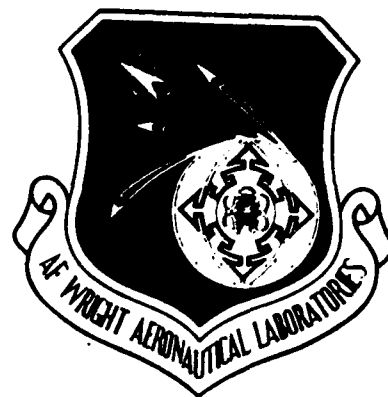


MICROCOPY RESOLUTION TEST CHART
NATIONAL BUREAU OF STANDARDS-1963-A

AD-A142 462

DTIC FILE COPY

AFWAL-TR-84-1034



(2)

LARGE-SIGNAL CHARACTERIZATION OF NONLINEAR TWO-PORT ACTIVE NETWORKS

One of a series of reports on Millimeter-Wave Circuit Analysis and Synthesis

D. C. Yang

Electron Physics Laboratory
Department of Electrical and Computer Engineering
The University of Michigan
Ann Arbor, Michigan 48109

April 1984

Interim Report for Period March 1, 1981-June 30, 1983

Approved for public release; distribution unlimited.

AVIONICS LABORATORY
AIR FORCE WRIGHT AERONAUTICAL LABORATORIES
AIR FORCE SYSTEMS COMMAND
WRIGHT-PATTERSON AIR FORCE BASE, OHIO 45433

DTIC
ELECTE
JUN 27 1984
B


84 06 26 07


NOTICE

When Government drawings, specifications, or other data are used for any purpose other than in connection with a definitely related Government procurement operation, the United States Government thereby incurs no responsibility nor any obligation whatsoever; and the fact that the government may have formulated, furnished, or in any way supplied the said drawings, specifications, or other data, is not to be regarded by implication or otherwise as in any manner licensing the holder or any other person or corporation, or conveying any rights or permission to manufacture use, or sell any patented invention that may in any way be related thereto.


This report has been reviewed by the Office of Public Affairs (ASD/PA) and is releasable to the National Technical Information Service (NTIS). At NTIS, it will be available to the general public, including foreign nations.

This technical report has been reviewed and is approved for publication.


ROBERT BLUMGOLD
Project Engineer
Microwave Techniques &
Applications Grp


ROBERT T. KEMERLEY, Acting Chief
Microwave Techniques and
Applications Grp
Microwave Technology Branch

FOR THE COMMANDER


DONALD S. REES, Chief
Microwave Technology Branch
Avionics Laboratory

"If your address has changed, if you wish to be removed from our mailing list, or if the addressee is no longer employed by your organization please notify AFWAL/AADM, W-PAFB, OH 45433 to help us maintain a current mailing list."

Copies of this report should not be returned unless return is required by security considerations, contractual obligations, or notice on a specific document.

SECURITY CLASSIFICATION OF THIS PAGE (When Data Entered)

REPORT DOCUMENTATION PAGE		READ INSTRUCTIONS BEFORE COMPLETING FORM
1. REPORT NUMBER AFWAL-TR-84-1034	2. GOVT ACCESSION NO. A142463	3. RECIPIENT'S CATALOG NUMBER
4. TITLE (and Subtitle) LARGE-SIGNAL CHARACTERIZATION OF NONLINEAR TWO-PORT ACTIVE NETWORKS		5. TYPE OF REPORT & PERIOD COVERED Interim Tech March 1, 1981-June 30, 1983
7. AUTHOR(s) D. C. Yang		6. PERFORMING ORG. REPORT NUMBER Tech. Report No. 163
9. PERFORMING ORGANIZATION NAME AND ADDRESS Electron Physics Laboratory The University of Michigan Ann Arbor, MI 48109		8. CONTRACT OR GRANT NUMBER(s) F33615-81-K-1429
11. CONTROLLING OFFICE NAME AND ADDRESS Avionics Laboratory (AFWAL/AADM-2) Air Force Wright Aeronautical Laboratories Wright-Patterson AFB, OH 45433		10. PROGRAM ELEMENT, PROJECT, TASK AREA & WORK UNIT NUMBERS 20020392
14. MONITORING AGENCY NAME & ADDRESS (if different from Controlling Office)		12. REPORT DATE April 1984
		13. NUMBER OF PAGES 135
		15. SECURITY CLASS. (of this report) Unclassified
		15a. DECLASSIFICATION/DOWNGRADING SCHEDULE N/A
16. DISTRIBUTION STATEMENT (of this Report) Approved for public release; distribution unlimited.		
17. DISTRIBUTION STATEMENT (of the abstract entered in Block 20, if different from Report)		
18. SUPPLEMENTARY NOTES The findings in this report are not to be construed as an official Department of the Air Force position, unless so designated by other authorized documents.		
19. KEY WORDS (Continue on reverse side if necessary and identify by block number) Large-signal characterization Nonlinear active two-port networks Large-signal properties of MESFETs GaAs MESFET Common drain MESFET oscillators Single-frequency oscillator Voltage-controlled oscillator		
20. ABSTRACT (Continue on reverse side if necessary and identify by block number) The objectives of this investigation include the development of a large-signal characterization procedure for nonlinear active two-port networks, analysis of the large-signal properties of MESFETs, and establishment of a large-signal MESFET equivalent circuit model. An approach for characterizing the single-frequency properties of a nonlinear two- port network is presented. The characterization results are useful in optimizing the external circuits for particular applications such as amplifiers and		

20.

oscillators. The information obtained regarding network properties can be used for establishing amplifier and oscillator design and stability criteria.

A GaAs MESFET was used as the nonlinear active two-port network, and its large-signal characteristics were measured. The nonlinear properties of the MESFET were investigated over the 7- to 13-GHz frequency range. The common drain configuration was studied extensively since this configuration is particularly advantageous for oscillator applications. The characterization results were applied to the design of common drain MESFET oscillators, and relationships between the output power and load impedances were established. The device performance as a voltage-controlled oscillator (VCO) was also investigated, with a single frequency oscillator built to verify the measurement results.

A large-signal equivalent circuit model of the MESFET is presented. This model can be established without extensive measurements and provides useful information in designing MESFET circuits for large-signal applications.

FOREWORD

This report describes the large-signal characterization of nonlinear two-port active networks carried out at the Electron Physics Laboratory, Department of Electrical and Computer Engineering, The University of Michigan, Ann Arbor, Michigan. The work was sponsored by the Air Force Systems Command, Avionics Laboratory, Wright-Patterson Air Force Base, Ohio under Contract No. F33615-81-K-1429.

The work reported herein was performed during the period March 1, 1981 to June 30, 1983 by Dr. Daniel C. Yang. The report was released by the author in June 1983.

The author wishes to thank Professor D. F. Peterson, his dissertation chairman, for his encouragement and guidance and Professor V. V. Liepa for his help in providing some of the equipment. He is also grateful to Dr. R. K. Mains and Messrs. J. R. East and C-K. Pao for their assistance in this investigation.

DTIC
ELECTE
S JUN 27 1984 D
B

Accession For	
NTIS GRA&I	<input checked="" type="checkbox"/>
DTIC TAB	<input type="checkbox"/>
Unannounced	<input type="checkbox"/>
Justification	
By	
Distribution/	
Availability Codes	
Dist	Avail and/or Special
A-1	

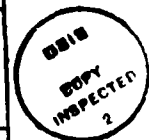


TABLE OF CONTENTS

CHAPTER

I. INTRODUCTION	1
1.1 Objective of the Present Study	1
1.2 Investigations Carried Out	4
1.2.1 Large-Signal Characterization of Nonlinear Two-Port Networks	4
1.2.2 Analysis of Experimental Results	4
1.2.3 Large-Signal MESFET Model	5
1.3 Summary	5
II. APPROACH FOR CHARACTERIZING THE SINGLE-FREQUENCY BEHAVIOR OF NONLINEAR TWO-PORT NETWORKS	6
2.1 Statement of the Problem and Network Description	6
2.2 Characterization Procedure	10
2.3 Amplifier and Oscillator Stability	18
2.3.1 Amplifier Stability	18
2.3.2 Oscillator Stability	23
2.4 Realization of Large-Signal Two-Port Characterization Technique	25
2.4.1 Measurement Setup	25
2.4.2 Measurement System Error	30
2.4.3 Test Fixture	33
2.4.4 Device Parameter Calculation	38
2.5 Summary	40
III. EXPERIMENTAL RESULTS	42
3.1 Introduction	42
3.2 Measurement Results	44
3.3 Common Drain MESFET Oscillator Design	50
3.3.1 Analysis of Measurement Results	50

3.3.2 Oscillator Design Using Characterization Results	54
3.4 Verification of Measurement Results	66
IV. LARGE-SIGNAL MESFET MODEL	72
4.1 Introduction	72
4.2 Large-Signal MESFET Equivalent Circuit Model	73
4.3 Summary	89
V. CONCLUSIONS	93
5.1 Summary and Conclusions	93
5.2 Suggestions for Further Study	95
APPENDICES	97
REFERENCES	121

LIST OF ILLUSTRATIONS

Figure		Page
2.1	A Nonlinear Two-Port Network and Its Terminal Conditions.	7
2.2	Single-Frequency Characterization of a Nonlinear Two-Port Network.	9
2.3	Terminal Conditions of an Active Nonlinear Two-Port Device.	12
2.4	Locus of b_1/a_1 of a Linear Device as a Function of the Phase Angle Between Incident Waves.	14
2.5	Nonlinear Active Two-Port Network as an Amplifier.	15
2.6	Nonlinear Active Two-Port Network as an Oscillator.	16
2.7	Characterization Results of a Nonlinear Two-Port Network for Amplifier Applications.	17
2.8	Characterization Results of a Nonlinear Two-Port Network for Oscillator Applications.	19
2.9	Amplifier Stability Viewed from Γ_{L2} Plane.	21
2.10	Amplifier Stability at Different Excitation Levels.	22
2.11	Termination of Harmonic Frequency Components by Using (a) Series Resonant Circuit, (b) Parallel Resonant Circuit.	27
2.12	Block Diagram of Two-Port Large-Signal Measurement Setup.	28
2.13	Sequence and Steps in Two-Port Large-Signal Measurement Program.	29

2.14	Polar Display Error.	31
2.15	GaAs MESFET Test Fixture.	35
2.16	GaAs MESFET Mounted on a Rib for Test.	36
2.17	Large-Signal Measurement Circuit Diagram.	39
3.1	500-mW Rated MESFET Chip.	43
3.2	Measured Gate and Source Terminal Impedances and Available Power at 7 GHz with Gate Test Signal at 160 mW.	46
3.3	Measured Gate and Source Terminal Impedances and Available Power at 7 GHz with Source Test Signal at 160 mW.	47
3.4	Measured Gate and Source Terminal Impedances and Available Power at 10 GHz.	48
3.5	Measured Gate and Source Terminal Impedances and Available Power at 13 GHz.	49
3.6	Gate and Source Loading Conditions for Constant Source Output Power of 100 mW at 7 GHz.	51
3.7	Gate and Source Loading Conditions for Constant Gate Output Power of 100 mW at 7 GHz.	52
3.8	Total Output Power vs. Gate Loss.	53
3.9	Gate and Source Load Impedance Regions for Maximum Power at Either Port at 7 GHz.	55
3.10	Source Output Power vs. Gate Loss.	56
3.11	Source Output Power vs. Source Load Impedance at 7 GHz.	57
3.12	Gate and Source Loading Conditions for a Constant Gate Loss of 3 Ω at 7 GHz	58
3.13	Gate and Source Loading Conditions for a Constant Gate Loss of 0.5 Ω at 7 GHz.	60

3.14	Gate and Source Loading Conditions for a Constant Gate Loss of 1.5 Ω at 7 GHz.	61
3.15	Gate and Source Loading Conditions for a Constant Gate Loss of 5 Ω at 7 GHz.	62
3.16	Gate and Source Loading Conditions for a Constant Gate Loss of 7.5 Ω at 7 GHz.	63
3.17	Gate and Source Loading Conditions for a Constant Gate Loss of 10 Ω at 7 GHz.	64
3.18	Gate and Source Loading Conditions vs. Output Power at 7 GHz.	65
3.19	Optimum Source Load, Output Power and Gate Reactance vs. Frequency for a 4 Ω Varactor Series Resistance.	67
3.20	Block Diagram of MESFET Oscillator Test Circuit.	68
3.21	Spectrum of a 7.2-GHz Common Drain MESFET Oscillator at (a) Fundamental Frequency, (b) Second-Harmonic Frequency.	69
3.22	Measured Gate, Source Impedance, Load Impedances Used in the Test Circuit.	71
4.1	MESFET Equivalent Circuit Model.	74
4.2	Equivalent Circuit Model of MESFET Package.	75
4.3	Simplified Common Drain MESFET Model.	77
4.4	Graphic Solution of Z_{gs} and g_m	80
4.5	Curve Fitted R_{gs} vs. RF Voltage $ V_{gs} $ at 7 GHz.	84
4.6	Curve Fitted C_{gs} vs. RF Voltage $ V_{gs} $ at 7 GHz.	85
4.7	Curve Fitted g_m vs. RF Voltage $ V_{gs} $ with $ V_2 = 5\text{ V}$ at 7 GHz.	86
4.8	Curve Fitted g_m vs. RF Voltage $ V_{gs} $ at 7 GHz.	87

4.9	Calculated vs. Measured Source Impedance and Output Power at 7 GHz.	88
4.10	Calculated vs. Measured Source Impedance and Output Power at 8 GHz.	90
4.11	Calculated vs. Measured Source Impedance and Output Power at 9 GHz.	91
A.1	Gate and Source Loading Conditions for a Constant Gate Loss of 0.5 Ω at 8 GHz.	93
A.2	Gate and Source Loading Conditions for a Constant Gate Loss of 7.5 Ω at 8 GHz.	99
A.3	Gate and Source Loading Conditions for a Constant Gate Loss of 10 Ω at 8 GHz.	100
A.4	Gate and Source Loading Conditions vs. Output Power at 8 GHz.	101
A.5	Gate and Source Loading Conditions for a Constant Gate Loss of 0.5 Ω at 9 GHz.	102
A.6	Gate and Source Loading Conditions for a Constant Gate Loss of 3 Ω at 9 GHz.	103
A.7	Gate and Source Loading Conditions for a Constant Gate Loss of 5 Ω at 9 GHz.	104
A.8	Gate and Source Loading Conditions for a Constant Gate Loss of 10 Ω at 9 GHz.	105
A.9	Gate and Source Loading Conditions vs. Output Power at 9 GHz.	106
A.10	Gate and Source Loading Conditions for a Constant Gate Loss of 0.5 Ω at 10 GHz.	107
A.11	Gate and Source Loading Conditions for a Constant Gate Loss of 3 Ω at 10 GHz.	108
A.12	Gate and Source Loading Conditions for a Constant Gate Loss of 5 Ω at 10 GHz.	109

A.13	Gate and Source Loading Conditions vs. Output Power at 10 GHz.	110
A.14	Gate and Source Loading Conditions for a Constant Gate Loss of 0.5 Ω at 11 GHz.	111
A.15	Gate and Source Loading Conditions for a Constant Gate Loss of 3 Ω at 11 GHz.	112
A.16	Gate and Source Loading Conditions vs. Output Power at 11 GHz.	113
B.1	Curve Fitted R_{gs} vs. RF Voltage $ V_{gs} $ at 8 GHz.	115
B.2	Curve Fitted C_{gs} vs. RF Voltage $ V_{gs} $ at 8 GHz.	116
B.3	Curve Fitted g_m vs. RF Voltage $ V_{gs} $ at 8 GHz.	117
B.4	Curve Fitted R_{gs} vs. RF Voltage $ V_{gs} $ at 9 GHz.	118
B.5	Curve Fitted C_{gs} vs. RF Voltage $ V_{gs} $ at 9 GHz.	119
B.6	Curve Fitted g_m vs. RF Voltage $ V_{gs} $ at 9 GHz.	120

LIST OF TABLES

Table		Page
4.1	MESFET and Package Parameters.	76
4.2	Calculated Values of Transconductance.	82
4.3	Calculated and Measured Source Impedances and Output Power.	92

LIST OF APPENDICES

Appendix	Page
A Additional Experimental Results at 8 to 11 GHz.	97
B MESFET Model Element Values at 8 and 9 GHz.	114

LIST OF SYMBOLS

A	Amplitude of oscillation.
A_0	Amplitude of steady-state oscillation.
a_1, a_2	Incident wave variables at port 1 and port 2, respectively.
b_1, b_2	Reflected wave variables at port 1 and port 2, respectively.
C_0	Drain to source capacitance.
C_1, C_2	MESFET package capacitances.
C_{gd}	Gate to drain capacitance.
C_{gs}	Gate to source capacitance.
d	Bonding wire diameter.
E_C	RF signal source voltage.
g_m	Transconductance.
I_1, I_2	Terminal currents at port 1 and port 2, respectively.
$L_{11}, L_{12}, L_{21}, L_{22}$	MESFET package inductances.
L_s	Bonding wire inductance.
l	Bonding wire length.
P_{D1}, P_{D2}	Delivered powers at port 1 and port 2, respectively.
P_{dev}	Delivered power.
P_g	Available power at gate.
P_{in1}, P_{in2}	Incident power levels at port 1 and port 2, respectively.
P_s	Available power at source.
R_0	Drain to source resistance.

R_1, R_2	MESFET package resistances.
R_D	Device resistance.
R_{gd}	Gate to drain resistance.
R_{gs}	Gate to source resistance.
R_S	Varactor series resistance.
s_0	Complex frequency at steady-state oscillation.
s	Complex oscillation frequency.
V_1, V_2	Terminal voltages at port 1 and port 2, respectively.
$ V_1 , V_2 $	Magnitudes of RF voltage at port 1 and port 2, respectively.
V_{ds}	Drain to source voltage.
V_{gs}	Gate to source voltage.
$ V_{gs} $	Magnitude of gate to source RF voltage.
X_D	Device reactance.
Z_0	Characteristics impedance.
Z_D	Device impedance.
Z_G	RF signal source impedance.
Z_{gs}	Gate to source impedance.
Z_L	Load impedance.
Z_{L1}, Z_{L2}	Load impedances at port 1 and port 2, respectively.
Z_{Lg}	Gate load impedance.
Z_{Ls}	Source load impedance.
Z_{T1}, Z_{T2}	Terminal impedances at port 1 and port 2, respectively.
Z_{Tg}	Gate terminal impedance.
Z_{Ts}	Source terminal impedance.
Γ_1, Γ_2	Reflection coefficients at port 1 and port 2, respectively.

Γ_{L1}, Γ_{L2}	Reflection coefficients of loads at port 1 and port 2, respectively.
δA	Perturbation of oscillation amplitude.
δs	Perturbation of complex oscillation frequency.
σ	Growth rate.
τ	Source to drain time delay.
φ	Phase angle between incident waves at port 1 and port 2.
ω	Angular frequency.
ω_0	Angular frequency for steady-state oscillation.

CHAPTER I

INTRODUCTION

1.1. Objective of the Present Study

Optimum performance of microwave solid-state circuits requires accurate knowledge of the device network parameters as a function of frequency and excitation level. One method of obtaining this information is by device characterization, where the device network properties are measured directly. Device modeling relates the characterization information into equivalent circuits useful for better understanding and more accurate prediction of the device behavior. The characterization of nonlinear devices is particularly difficult since the device cannot be described by simple relationships among the device terminal quantities.

For years, information about two-port networks was obtained exclusively from small-signal measurements. The circuit designer used the small-signal S-parameters to design large-signal circuits by first determining the load at one port using the small-signal device information, and then using either a cut-and-try method or simple measurement to match the load at the other port.¹⁻⁵ For nonlinear devices such as BJTs (Bipolar Junction Transistors) and FETs (Field Effect Transistors), small-signal S-parameters cannot satisfactorily describe the device nonlinear performance nor can they provide necessary information for designing any circuit operating under large-signal conditions. A number of approaches are available to overcome the difficulties caused by the nonlinear behavior of these devices. One such method is the load-pull technique.⁶⁻¹¹ The

load-pull measurement employs separate tuning circuits at the input and the output ports, and the device performance is recorded under variable load conditions. Usually the load at the input port is kept constant to reduce measurement complexity while loci of load impedances for a constant parameter such as power or efficiency are recorded. This process is very tedious since each load has to be disconnected for measurement of its impedance value. Because the load at one port is predetermined, it is difficult to optimize the terminal conditions at both ports. An optimum design requires both ports to be optimized.

Since it is difficult to experimentally characterize a nonlinear network, efforts have been made to establish an empirical large-signal device model, and to use this model in circuit design.¹¹⁻¹⁶ Due to the limited amount of information that can be obtained by measurement, these empirical device models can only approximate the device characteristics. Other attempts to deal with the large-signal circuit design were only of limited success. Rauscher¹⁷ modified a small-signal device model and used it for designing fixed frequency oscillators. Rector and Vandelin¹⁸ used small-signal S-parameters in combination with simple measurements to predict the large-signal FET performance for oscillator design. Mitsui et al.^{19,20} used S-parameters measured at high power levels for their MESFET (MEtal Semiconductor Field Effect Transistor) circuit design. Scanlan and Young²¹ discussed the errors introduced by using simplified linear MESFET models, but did not offer any solution to reduce these errors. Johnson²² used the large-signal measurement results obtained with 50- Ω terminations to design MESFET oscillators. Although all these papers recognized the need of accurate knowledge of large-signal properties of nonlinear devices to design amplifiers and oscillators, none provided a good characterization method. The need to establish a large-signal characterization technique has become crucial to improved nonlinear circuit design.

The device characteristics are functions of bias, frequency, power levels, and load impedances. Under a given bias and frequency, the device performance is a function of the terminal conditions at both ports. In order to characterize the device accurately, the device terminal conditions have to be varied during the course of measurement to cover the entire device operating range. The conventional large-signal measurement using a $50\text{-}\Omega$ system characteristic impedance as the termination will not yield the necessary information in designing a circuit where the load is most likely other than $50\text{ }\Omega$. A two-signal method, as reported by Mazumder and Van Der Puije,²³ was an initial attempt in the proper direction to characterize nonlinear devices.

The characterization technique presented in this report uses two coherent variable amplitude and phase signals at the two ports of the network. By adjusting the magnitude and relative phase of these two test signals and injecting them into both ports simultaneously, any set of terminal conditions for the device under test can be established and are readily varied. In practice, two network analyzers are used in this study to monitor the terminal conditions at both ports simultaneously. The measurement results give the available power and equivalent load impedance at each port. Such information is essential in the design of any solid-state microwave circuit with active two-port nonlinear networks.

Although accurate device information can be obtained through large-signal characterization, it is not practical to make such measurements each time the information is needed. For this reason, a large-signal device model is useful because, once established, it can predict the device performance accurately without extensive measurements. Determining such a large-signal device model is an important part of this study.

1.2. Investigations Carried Out

1.2.1. Large-Signal Characterization of Nonlinear Two-Port Networks In Chapter II, the problems of characterizing a nonlinear two-port network under large-signal conditions are defined and the proposed solutions are discussed. The implementation of this characterization technique is also presented.

In order to characterize a nonlinear two-port network, a set of parameters which can uniquely describe the network must be identified. A set of incident and reflected wave variables are used to establish the network terminal conditions. The characterization procedure is developed based on this approach. Since the network is nonlinear, the stability criteria of amplifiers and oscillators are different from those of linear networks. Discussions of the stability of two-port amplifiers and oscillators are presented.

To realize this large-signal characterization technique, a measurement setup controlled by a desk-top calculator was developed. During the development of the measurement technique some special calibration and error correction problems were encountered. Such problems include the errors caused by the non-linearity of the network analyzer measurement system and the calibration to the device terminals. Each of these problems is discussed and the solution presented. The characterization procedures are presented in detail, as well as the calculations of all relevant device terminal parameters.

1.2.2. Analysis of Experimental Results The characterization results and their applications are presented in Chapter III. GaAs MESFETs were used as the two-port device for large-signal characterization. The MESFETs were measured in the common drain configuration for their potential use in a simple oscillator configuration. In this configuration, the device can be used as an oscillator without the need of additional feedback.

The characterization results were analyzed for the design of common drain MESFET oscillators including applications as wideband voltage controlled oscillators. A single-frequency oscillator was built and tested to verify the measurement results.

1.2.3. Large-Signal MESFET Model A large-signal MESFET equivalent circuit model was established from the characterization results. In this model the non-linear element values were expressed as functions of the device terminal RF voltages. To improve the modeling accuracy, the device package parasitics were modeled and their values were taken into account during the calculation of the device model. It is possible to establish the device model without extensive measurements. This model facilitates the design of various MESFET circuits and can be used for investigating the amplifier and oscillator stability criteria.

1.3. Summary

The theory, measurement procedures, and experimental results of the two-port large-signal characterization technique and a large-signal MESFET equivalent circuit model are discussed in detail in the following chapters. In the final chapter, the conclusions of the study and suggestions for further study are presented.

CHAPTER II
APPROACH FOR CHARACTERIZING THE SINGLE-FREQUENCY
BEHAVIOR OF NONLINEAR TWO-PORT NETWORKS

2.1. Statement of the Problem and Network Description

The objective of characterizing a nonlinear two-port network is to obtain the optimum operating conditions for applications such as in power amplifiers and oscillators. Previous attempts to characterize such networks were only of limited success because such characterizations did not provide enough information about the nonlinear networks.^{23,24} A nonlinear two-port network can be described by its terminal voltages and currents as shown in Fig. 2.1. two-port network can be described by its terminal voltages and currents. The purpose of network characterization is to determine the relationships among these terminal quantities. At microwave frequencies, it is more convenient to express the terminal conditions in terms of wave variables, because the wave variables are directly related to the incident and the reflected signal power levels and can be readily measured. The incident wave variables at ports 1 and 2 are represented by a_1 and a_2 , respectively, while b_1 and b_2 represent the reflected wave variables. The relationships between the wave variables and the terminal voltages and currents are described as follows:

$$a_1 = \frac{1}{2} \left(\frac{V_1}{\sqrt{Z_0}} + \sqrt{Z_0} I_1 \right) \quad . \quad (2.1)$$

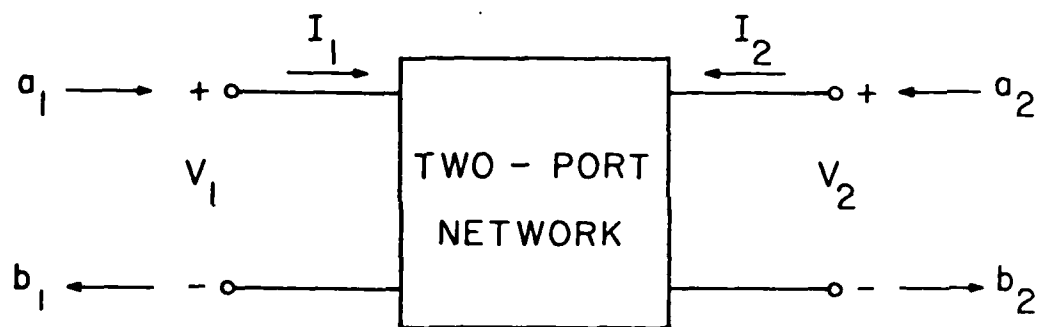


Fig. 2.1 A Nonlinear Two-Port Network and Its Terminal Conditions.

$$b_1 = \frac{1}{2} \left(\frac{V_1}{\sqrt{Z_0}} - \sqrt{Z_0} I_1 \right) \quad (2.2)$$

$$a_2 = \frac{1}{2} \left(\frac{V_2}{\sqrt{Z_0}} + \sqrt{Z_0} I_2 \right) \quad (2.3)$$

and

$$b_2 = \frac{1}{2} \left(\frac{V_2}{\sqrt{Z_0}} - \sqrt{Z_0} I_2 \right) \quad (2.4)$$

where Z_0 is the characteristic impedance of the measurement setup.

A nonlinear two-port network excited at each port by independent single-frequency incident wave variables a_1 and a_2 as shown in Fig. 2.2 is considered. In general the response to the test signals a_1 and a_2 generates additional harmonic components. An ideal bandpass filter is presented at each port to trap all harmonic frequency components such that the measured terminal conditions are at the fundamental frequency only. The dependent reflected wave variables b_1 and b_2 at the same frequency depend on the incident wave variables and are expressed as

$$b_1 = f_1(a_1, a_2) \quad (2.5)$$

and

$$b_2 = f_2(a_1, a_2) \quad (2.6)$$

These expressions can be transformed into more useful quantities, such as the reflection coefficient, at each port as

$$\Gamma_1 = \frac{b_1}{a_1} = \gamma_1(|a_1|, |a_2|, \varphi) \quad (2.7)$$

and

$$\Gamma_2 = \frac{b_2}{a_2} = \gamma_2(|a_1|, |a_2|, \varphi) \quad (2.8)$$

where φ is the phase between a_1 and a_2 . Since the reflection coefficient is the

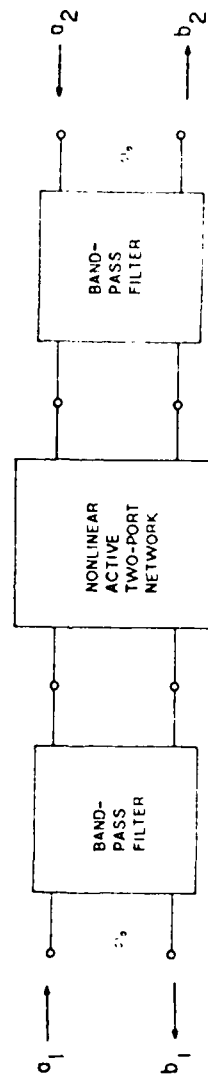


Fig. 2.2 Single Frequency Characterization of a Nonlinear Two-Port Network.

ratio between the reflected and the incident wave variables at that port, it is a function of the magnitudes of the two incident wave variables and the phase angle between them. The network can thus be characterized by Γ_1 , Γ_2 , $|a_1|$, $|a_2|$, and φ . The reflection coefficients determine the load impedance at each port while the wave variables are closely related to the available or dissipated power at each port.

2.2. Characterization Procedure

Many previous attempts have been reported to characterize the large-signal behavior of nonlinear two-port networks. None of these methods could address the problem correctly nor could they provide satisfactory results. One such method is the load-pull technique. Load-pull measurements require the termination of one port while the other is measured. Since the terminal conditions at two ports depend upon each other as indicated in Eqs. 2.5 and 2.6, the loads at both ports have to be optimized at the same time. This is difficult to achieve while one port has already been terminated with some predetermined load.

Some attempts were also made to use the S-parameters for large-signal applications.²⁴ As S-parameters only characterize linear devices, restrictive assumptions must be made in order to use these parameters. These assumptions often limit the application to certain special cases and cannot represent the large-signal device behavior in general.

To implement the large-signal two-port characterization technique, a two-signal method as reported by Yang and Peterson in Reference 25 was used in this study. By varying the excitation signal levels and their relative phase, the reflection coefficients at both ports change according to Eqs. 2.7 and 2.8. The reflection coefficients in turn specify the terminal impedances and excitation levels of the network. Because the test signals are presented at both ports,

terminal conditions can be measured simultaneously. It is not necessary to disassemble or switch the test circuit to measure the reflection coefficients.

The terminal conditions of an active nonlinear two-port network are shown in Fig. 2.3. Because of the small physical size of some two-port devices, the device terminals are not directly accessible by the network analyzer. Coupling networks must be built to connect the device terminals to the network analyzer measurement ports. The circuit parameters of the coupling network is predetermined such that any quantity measured can be transferred to the device terminals.

The incident test signal power levels P_{in1} and P_{in2} and the delivered power at each port P_{D1} and P_{D2} are expressed in terms of the wave variables as

$$P_{in1} = |a_1|^2 \quad , \quad (2.9)$$

$$\begin{aligned} P_{D1} &= |a_1|^2 - |b_1|^2 \\ &= P_{in1}[1 - |\Gamma_1|^2] \quad , \end{aligned} \quad (2.10)$$

$$P_{in2} = |a_2|^2 \quad , \quad (2.11)$$

and

$$\begin{aligned} P_{D2} &= |a_2|^2 - |b_2|^2 \\ &= P_{in2}[1 - |\Gamma_2|^2] \quad . \end{aligned} \quad (2.12)$$

From Eqs. 2.7 and 2.8, the reflection coefficient is a function of $|a_1|$, $|a_2|$ and φ . By varying the two test signal power levels and their relative phase angle, different values of reflection coefficient and the corresponding net power crossing each port can be obtained.

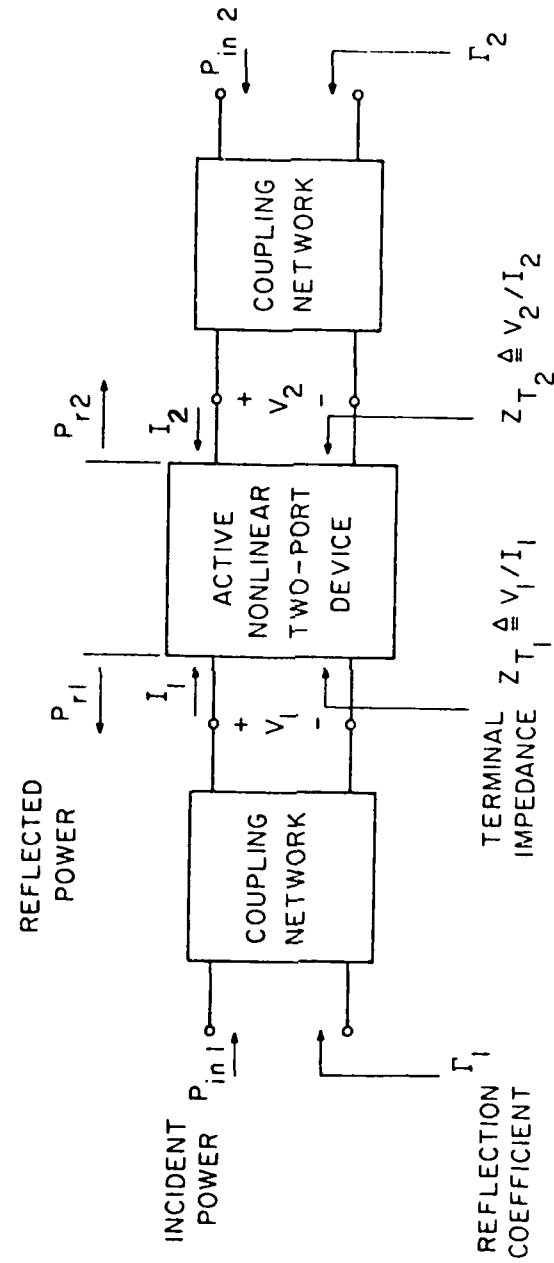


Fig. 2.3 Terminal Conditions of an Active Nonlinear Two-Port Device.

For a linear device, the reflection coefficient is a function of $|a_1|$, $|a_2|$, and φ . If the ratio between $|a_1|$ and $|a_2|$ remains constant while φ varies, the loci of the reflection at port 1, $|\Gamma_1|$, forms a circle as shown in Fig. 2.4. The radius of the circle is determined by the quantity $|a_2/a_1|$, and the center represents the reflection coefficient at port 1 with no incident wave at port 2 reaching port 1. Because the parameters of a linear device are constant over its entire operating range, a single measurement is sufficient to characterize the device properties under all operating conditions.

In the case of a nonlinear device, the parameters change as the terminal conditions vary. The device must be characterized under various power and loading conditions. Depending on the application, different criteria are set for characterizing the devices. For applications such as amplifiers the goal is to find the optimum terminal conditions for either maximum output power, maximum added power, or maximum gain. It is desired to have a passive input port, $|\Gamma_1| < 1$, and an active output port, $|\Gamma_2| > 1$. A conjugate match is used at the input port, i.e., $\Gamma_{L1} = \Gamma_1^*$. While at the output port a load of the reflection coefficient $\Gamma_{L2} = 1/\Gamma_2^*$ is used.

For oscillator applications the goal could be either maximum output power or maximum tuning bandwidth. In this case both ports must be active which means $|\Gamma_1| > 1$ and $|\Gamma_2| > 1$. The reflection coefficient of the load has to be the reciprocal of that at each port, i.e., $\Gamma_{L1} = 1/\Gamma_1$ and $\Gamma_{L2} = 1/\Gamma_2$. Figures 2.5 and 2.6 show a nonlinear two-port network used as an amplifier and an oscillator, respectively.

Typical nonlinear characterization results of a MESFET in common source configuration are shown in Fig. 2.7. These results were obtained by keeping $|a_1|$ and $|a_2|$ constant and varying the phase φ from 0 to 2π rad. Since the drain

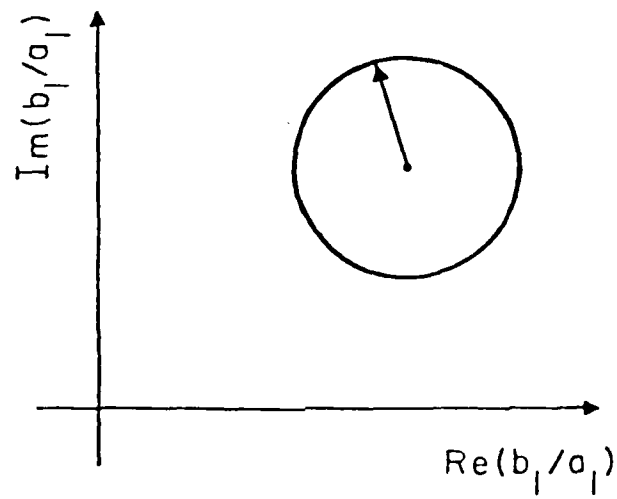
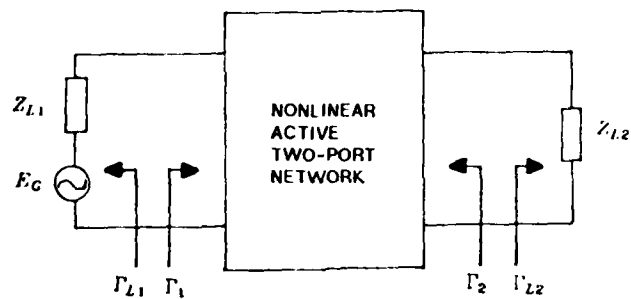


Fig. 2.4 Locus of b_1/a_1 of a Linear Device as a Function of the Phase Angle Between Incident Waves.



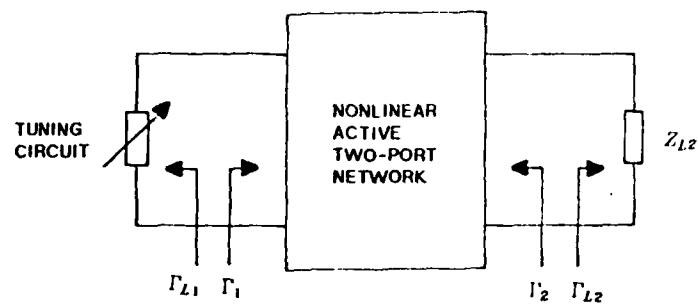
CHARACTERIZATION GOALS:

1. MAXIMUM OUTPUT POWER
2. MAXIMUM ADDED POWER
3. MAXIMUM GAIN

CIRCUIT REQUIREMENTS:

1. $|\Gamma_1| < 1, |\Gamma_2| > 1$
2. $\Gamma_{L1} = \Gamma_1^*$ $\Gamma_{L2} = \frac{1}{\Gamma_2}$

Fig. 2.5 Nonlinear Active Two-Port Network as an Amplifier.



CHARACTERIZATION GOALS:

1. MAXIMUM OUTPUT POWER
2. MAXIMUM TUNING BANDWIDTH

CIRCUIT REQUIREMENTS:

1. $|\Gamma'_1| > 1$, $|\Gamma'_2| > 1$
2. $\Gamma_{L1} = \frac{1}{\Gamma'_1}$, $\Gamma_{L2} = \frac{1}{\Gamma'_2}$

Fig. 2.6 Nonlinear Active Two-Port Network as an Oscillator.

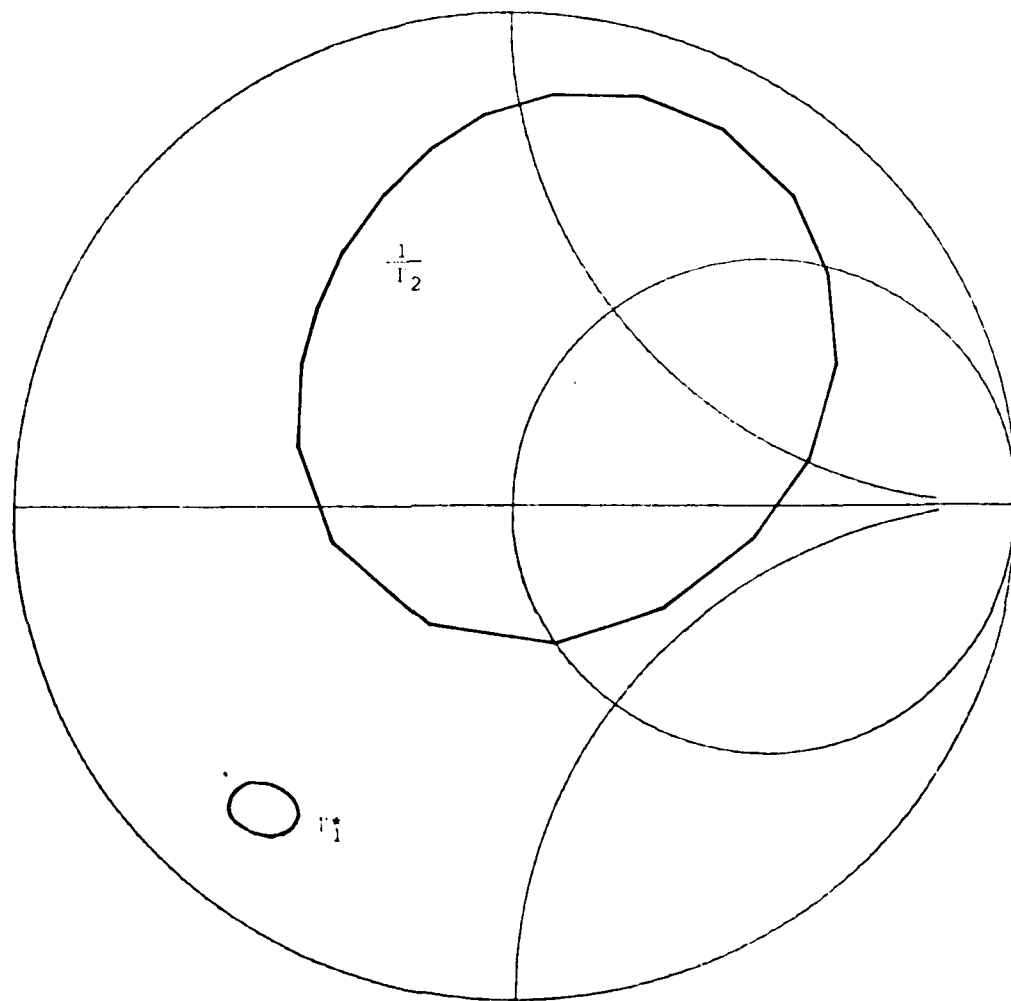


Fig. 2.7 Characterization Results of a Nonlinear Two-Port Network for Amplifier Applications.

side is active, the inverse of the reflection coefficients are plotted on a Smith chart. This gives the desired load impedances required to achieve the measured conditions. The gate port was passive and the desired load impedance as plotted was the complex conjugate of the terminal impedance. It is noted that because of the device nonlinearity, the locus of both terminal impedances are not circular as would be in the case of a linear device.

To characterize the device for oscillator applications, it is necessary to connect the device in a different configuration such that both ports are active. Figure 2.8 shows an example of characterization results for a common drain MES-FET. Because both ports were active the inverse of the measured reflection coefficients were plotted on a Smith chart, directly indicating the desired load impedances to achieve the measured conditions. Both $|a_1|$ and $|a_2|$ were kept constant and φ was varied from 0 to 2π rad, but only the portion where both ports were active was plotted. The nonlinear behavior of the device is apparent in this plot.

2.3. Amplifier and Oscillator Stability

2.3.1. Amplifier Stability The amplifier design is simplified when the two-port device is unconditionally stable. In this case the large-signal characterization provides information leading to the optimum design of amplifiers. However, these characterization results must meet the stability criterion. For a stable amplifier, it is required to have the magnitude of the input port reflection coefficient less than unity, i.e., $|\Gamma_1| < 1$. The case where the output port is terminated with a load Z_{L2} is considered. The reflection coefficient of the load is then

$$\Gamma_{L2} = \frac{a_2}{b_2} \quad (2.13)$$

From Eq. 2.5, the reflected wave at port 1, b_1 , then becomes a function of the

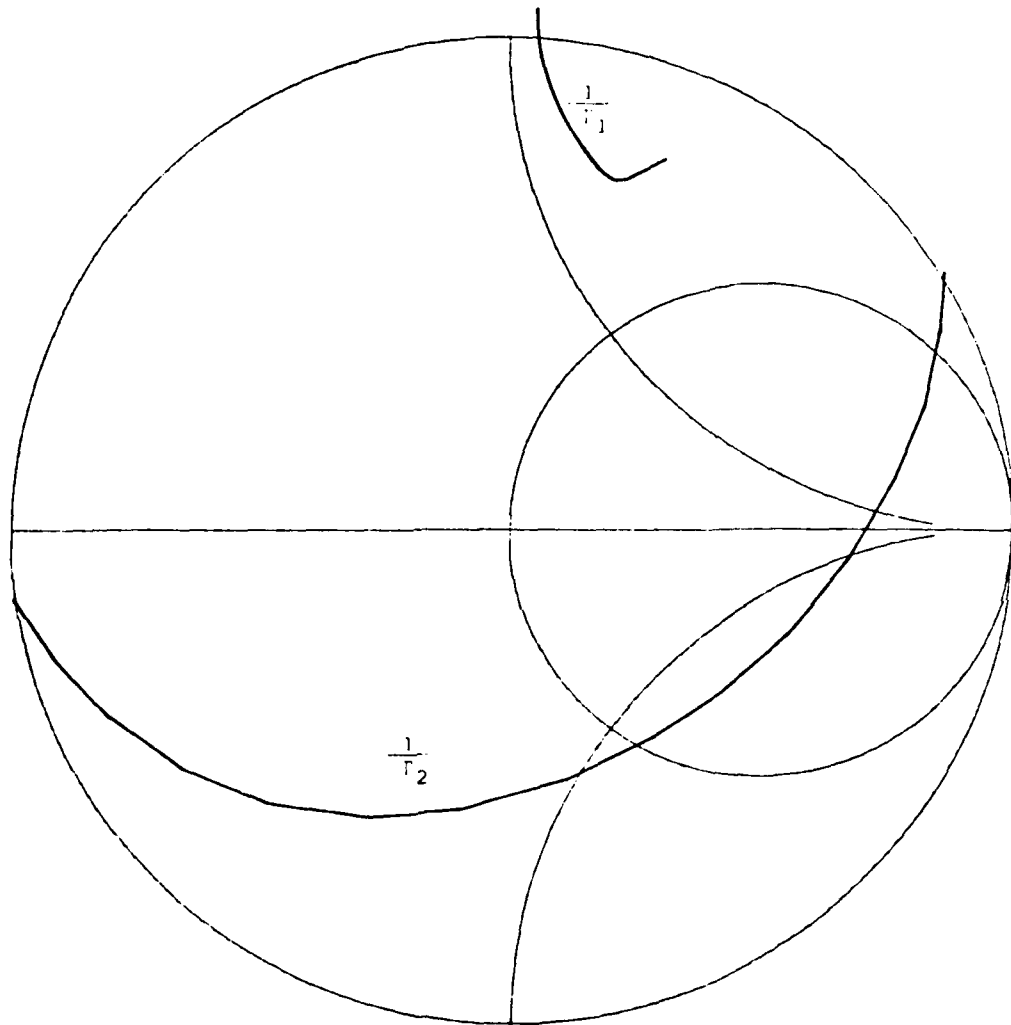


Fig. 2.8 Characterization Results of a Nonlinear Two-Port Network for Oscillator Applications.

Incident wave a_1 and the reflection coefficient of the load at port 2, Γ_{L2} , as

$$b_1 = f_1(a_1, \Gamma_{L2}) \quad (2.14)$$

The reflection coefficient at port 1, Γ_1 , is

$$\Gamma_1 = \gamma_1(a_1, \Gamma_{L2}) \quad (2.15)$$

For a given excitation level $|a_1|$, it is necessary to find the values of Γ_{L2} to keep the amplifier stable. The stability conditions are indicated by mapping the $|\Gamma_1| = 1$ circle onto the Γ_{L2} plane as shown in Fig. 2.9. Because the relationship expressed in Eq. 2.15 is nonlinear, the locus of the $|\Gamma_1| = 1$ may not be circular. Once a mathematical relationship is established between Γ_1 and Γ_{L2} , the unstable region in Fig. 2.9 can be identified. For illustration purposes, it is assumed that the area encircled by the mapping of $|\Gamma_1| = 1$ is the unstable region. The output port of the amplifier is usually terminated by a stable load, i.e., $|\Gamma_{L2}| < 1$, represented by the area inside the $|\Gamma_{L2}| = 1$ circle. The amplifier is unconditionally stable if the areas enclosed by $|\Gamma_{L2}| = 1$ and the $|\Gamma_1| = 1$ mapping do not overlap. This means that all load impedances with $\text{Re}(Z_L) > 0$ satisfy the stability criterion. If two areas overlap, the load impedances corresponding to the overlapped area will cause unstable conditions for the amplifier and should be avoided. This is called conditionally stable situation.

Because of the device nonlinearity, the relationship between the $|\Gamma_1| = 1$ mapping and the $|\Gamma_{L2}| = 1$ circle is different at each excitation level. To study the stability at various excitation levels, a three-dimensional illustration is constructed with the third axis representing $|a_1|$, as shown in Fig. 2.10. This gives the whole picture of amplifier stability under large-signal conditions. If the unstable region does not overlap the $|\Gamma_{L2}| = 1$ circle for all values of a_1 , then the amplifier circuit is unconditional stable over its entire operating region.

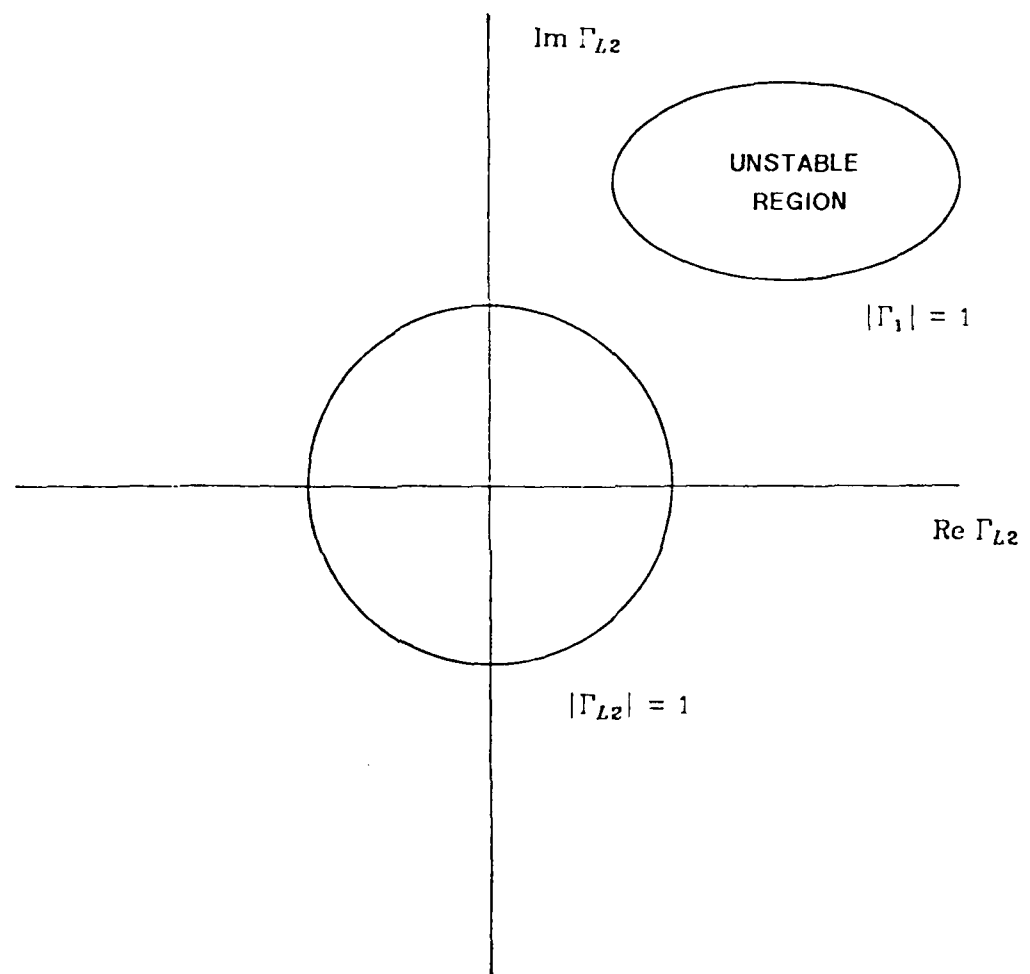


Fig. 2.9 Amplifier Stability Viewed from Γ_{L2} Plane.

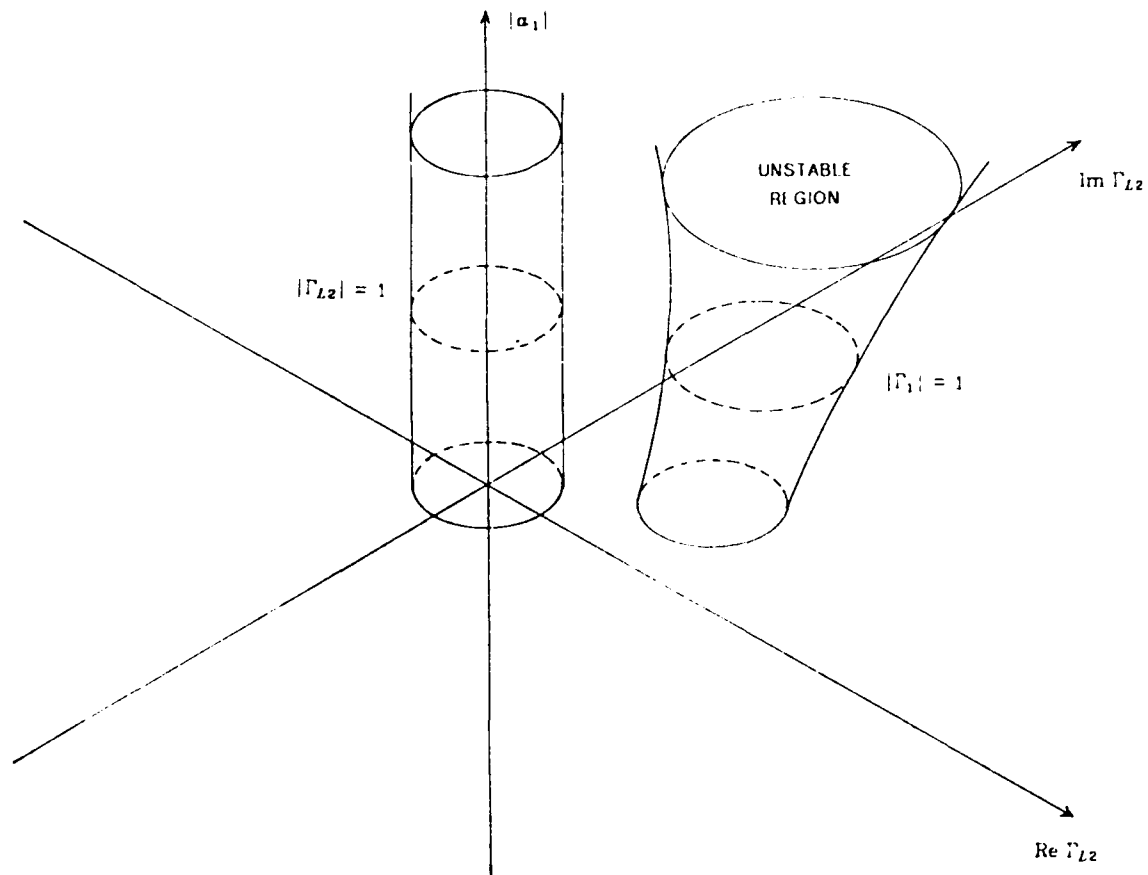


Fig. 2.10 Amplifier Stability at Different Excitation Levels.

2.3.2. Oscillator Stability Oscillator stability criteria can be used to determine whether the proposed loading circuits will permit a steady state oscillation. A stable oscillator means that any perturbation of the amplitude of the oscillation from the steady state value decays with time. The condition for oscillation for a one-port active network terminated in a passive circuit is given by

$$\Gamma_D(|a|, s) = \frac{1}{\Gamma_L(s)} \quad (2.16)$$

where $\Gamma_D(|a|, s)$ is the reflection coefficient of the active network, $\Gamma_L(s)$ is the reflection coefficient of the external circuit, $|a|$ is the amplitude of oscillation and s is the complex frequency. In general, the complex frequency is expressed by

$$s = \sigma + j\omega \quad (2.17)$$

The real part, σ , is the growth rate and ω is the angular frequency. When the oscillator reaches steady state, the following conditions exist

$$|a| = a_0 \quad (2.18)$$

$$\sigma = 0 \quad (2.19)$$

and

$$\omega = \omega_0 \quad (2.20)$$

such that

$$s_0 = j\omega_0 \quad (2.21)$$

The stability criterion is given by

$$\operatorname{Re} \left[\frac{ds}{d|a|} \right] \bigg|_{a_0, s_0} < 0 \quad (2.22)$$

For a two-port circuit this criterion can be applied to either port when the other

is terminated. The reflection coefficient presented at one port depends on the load at the other such that the reflection coefficient Γ_1 can be represented by either Γ_1 or Γ_2 when the other port is terminated. The input port reflection coefficient is then a function of both amplitude and frequency while the reflection coefficient of the circuit is a function of frequency only.

If δa is an amplitude perturbation at port 1 and δs is the associated change in s from the steady state, then for port 1 Eq. 2.16 gives

$$\Gamma_1(a_0 + \delta |a_1|, s_0 + \delta s) - \frac{1}{\Gamma_{L1}(s + \delta s)} = 0 \quad (2.23)$$

where Γ_{L1} is the reflection coefficient of the external circuit at port 1 as previously shown in Fig. 2.6. A Taylor series expansion of Eq. 2.23 gives

$$\begin{aligned} \Gamma_1(a_0 + s_0) + \left[\delta |a_1| \frac{\partial}{\partial |a_1|} + \delta s \frac{\partial}{\partial s} \right] \Gamma_1(|a_1|, s) \Big|_{a_0, s_0} \\ = \frac{1}{\Gamma_{L1}(s_0)} + \delta s \frac{\partial}{\partial s} \frac{1}{\Gamma_{L1}(s)} \Big|_{s_0} \end{aligned} \quad (2.24)$$

where only the first order terms are retained. Canceling the steady state terms gives

$$\delta |a_1| \frac{\partial}{\partial |a_1|} \Gamma_1(|a_1|, s) \Big|_{a_0, s_0} = \delta s \frac{\partial}{\partial s} \left[\frac{1}{\Gamma_{L1}(s)} - \Gamma_1(|a_1|, s) \right] \Big|_{a_0, s_0} \quad (2.25)$$

and

$$\frac{\delta s}{\delta |a_1|} \Big|_{port 1} = \frac{\frac{\partial \Gamma_1(|a_1|, s)}{\partial |a_1|}}{\frac{\partial}{\partial s} \left[\frac{1}{\Gamma_{L1}(s)} - \Gamma_1(|a_1|, s) \right]} \Big|_{a_0, s_0} \quad (2.26)$$

In Eq. 2.26, Γ_1 is the reflection coefficient at port 1 with port 2 terminated, i.e.

$$\Gamma_1 = \gamma_1[|a_1|, s, \Gamma_{L2}(s)] \quad (2.27)$$

A similar expression for port 2 can be obtained as

$$\left. \frac{\delta s}{\delta |a_2|} \right|_{\text{port 2}} = \frac{\frac{\partial \Gamma_2(|a_2|, s)}{\partial |a_2|}}{\frac{\partial}{\partial s} \left[\frac{1}{\Gamma_{L2}(s)} - \Gamma_2(|a_2|, s) \right]} \bigg|_{s=s_0} \quad (2.28)$$

and

$$\Gamma_2 = \gamma_2[|a_2|, s, \Gamma_{L1}(s)] \quad (2.29)$$

During the oscillation, the condition of $\Gamma_{L1} = 1/\Gamma_1$ and $\Gamma_{L2} = 1/\Gamma_2$ must always be satisfied. Since both ports are coupled, any unstable condition at one port will show up at the other port. Thus, it is only necessary to investigate the stability at one port by using either Eq. 2.26 or 2.28.

2.4. Realization of Large-Signal Two-Port Characterization Technique

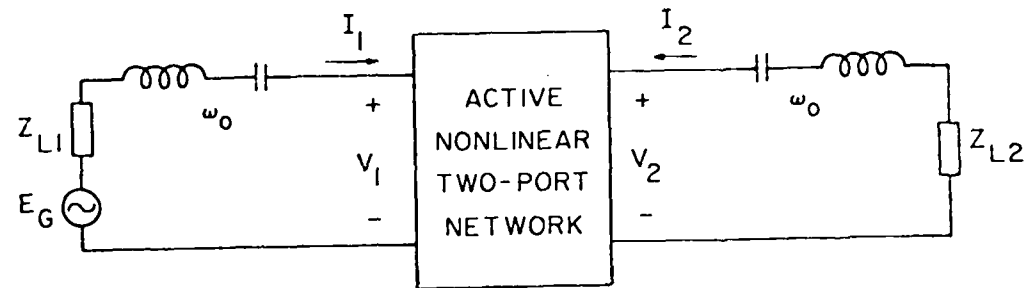
2.4.1. Measurement Setup The goal of characterization is to determine the terminal conditions of the device under test and express these quantities in useful terms such as impedances and power levels. For a nonlinear two-port device, it is necessary to determine the terminal impedances and their corresponding available or dissipated power levels. From Eqs. 2.7 and 2.8, the reflection coefficients Γ_1 and Γ_2 are functions of $|a_1|$, $|a_2|$, and φ . The values of $|a_1|$ and $|a_2|$ are controlled by the test signal power at port 1 and port 2, respectively, while φ can be varied by a phase shifter. The exact value of φ is necessary only when feedback circuits are used around the device. If only the power levels and terminal impedances are of interest in the characterization, the knowledge of φ is not important because the relative phase of the signals at the two ports need not be known.

For single-frequency measurement, it is essential to maintain only the fundamental frequency in the measurement setup and to suppress the harmonic frequency components. For this either series or parallel resonant circuits or ideal

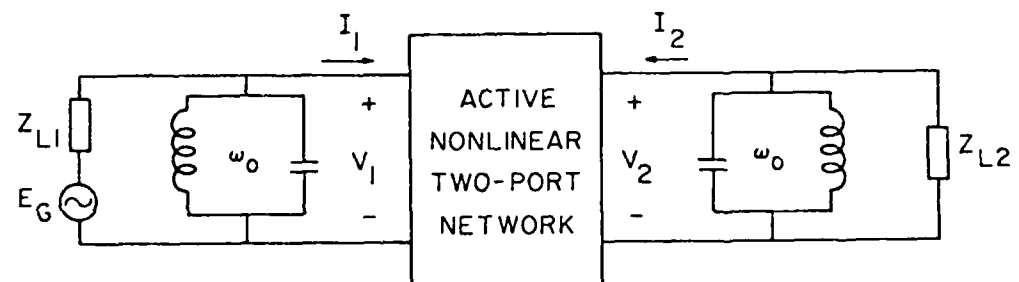
bandpass filters can be used to block or terminate the harmonic frequency components as shown in Figs. 2.11a and 2.11b. In the actual measurements the use of a resonant circuit may not be necessary if the equipment used in the setup provides sufficient attenuation at the harmonic frequencies. It was also found that no significant harmonics were generated in this setup. The second-harmonic frequency power level measured more than 20 dB down from that of the fundamental frequency.

A measurement system for providing Γ_1 , Γ_2 , $|a_1|$, and $|a_2|$ is shown in Fig. 2.12. The RF test signal power level is first amplified by a traveling-wave tube amplifier and then power divided to provide the required two signals. The phase between these two signals is varied using a phase shifter, and the power level of each test signal is controlled by variable attenuators. These attenuators can be further controlled by a feedback loop to keep the power level constant throughout the course of measurement. Test signal power is also monitored by a power meter through a directional coupler. The test signal is then fed to the device through the reflection test unit.

The measurement system uses two network analyzers. An HP-9825A desk-top calculator is used to control and acquire data from the measurement system. A flow chart of the large-signal two-port measurement program is shown in Fig. 2.13. Because of the limited capacity of calculator memory, the actual measurement program was divided into two parts. The measurement system was first calibrated with the error coefficients stored on a data cartridge. Then, the measurement part of the program was loaded into the calculator along with the coupling network parameters and error coefficients. The characterization consisted of two measurements of the reflection coefficients, one for each port. Specification of the test signal power levels allowed the terminal impedances, RF voltages and currents, and reflected powers to be determined. The results were



(a)



(b)

Fig. 2.11 Termination of Harmonic Frequency Components by Using
 (a) Series Resonant Circuit, (b) Parallel Resonant Circuit.

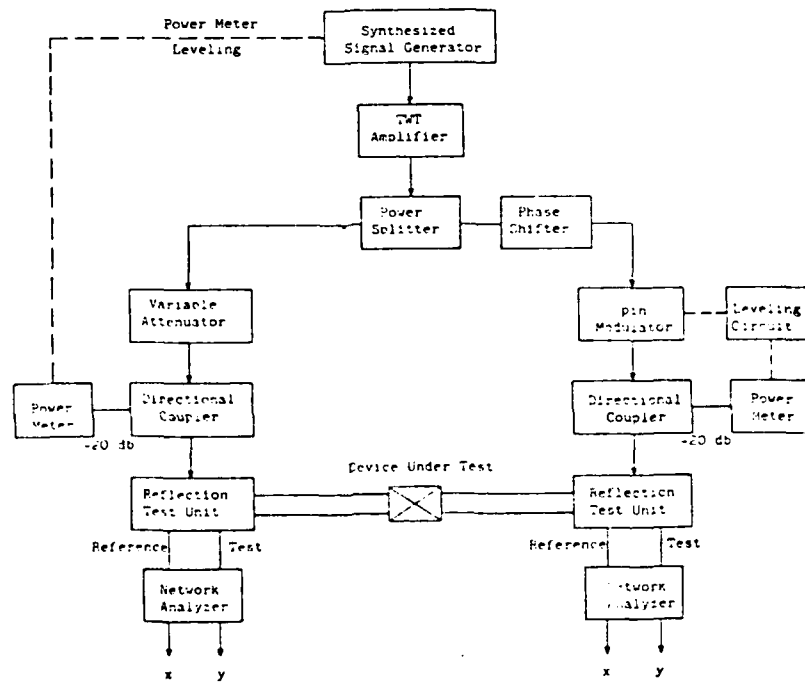


Fig. 2.12 Block Diagram of Two-Port Large-Signal Measurement Setup

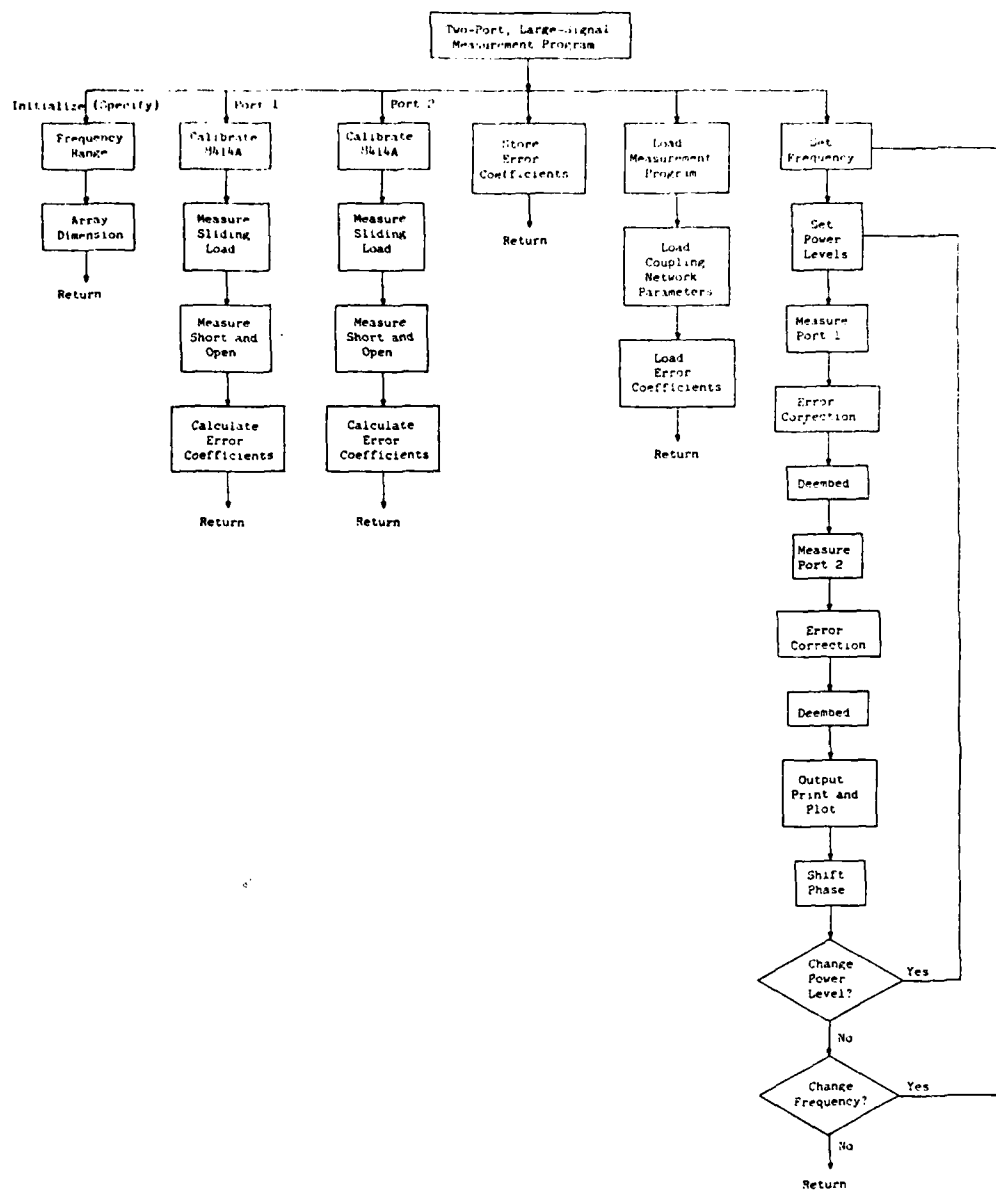


Fig. 2.13 Sequence and Steps in Two-Port Large-Signal Measurement Program.

usually stored on data cartridges for further analysis.

2.4.2. Measurement System Error In any measurement system inevitably there are errors preventing measured data from being a true representation of an unknown. In a network analyzer measurement system, the basic errors are the measurement errors and the display unit errors. The measurement errors occur while the measurement is being made and are caused by directivity, frequency response, source mismatch, drift, and noise. During the measurement the data are displayed and sampled by an interface unit for storage in the calculator. The display may have some nonlinearity and will introduce errors. The measurement errors and their correction procedures are already well known.²⁶ The display unit error is the subject of discussion in this section.

Measurement results from the HP-8410 network analyzer are available through one of the following display units: a phase-magnitude display, a phase-gain indicator, and a polar display. The polar display was used in the actual measurement system because it provides visual impedance display on a Smith chart and continuous horizontal and vertical voltage outputs corresponding to the real and imaginary parts of the reflection coefficient. Due to the errors in the signal processing circuits, the polar display cannot provide true readings and the results must be error corrected.

Figure 2.14 shows a $|\Gamma| = 1$ circle on the reflection plane as compared to the loci of the same circle distorted by unequal gain and cross coupling between the horizontal (real) and vertical (imaginary) channels. The horizontal and vertical values of the reflection coefficient expressed in the distorted $x'-y'$ plane in terms of the actual x and y values are

$$x' = \alpha x + \beta y \quad (2.30)$$

and

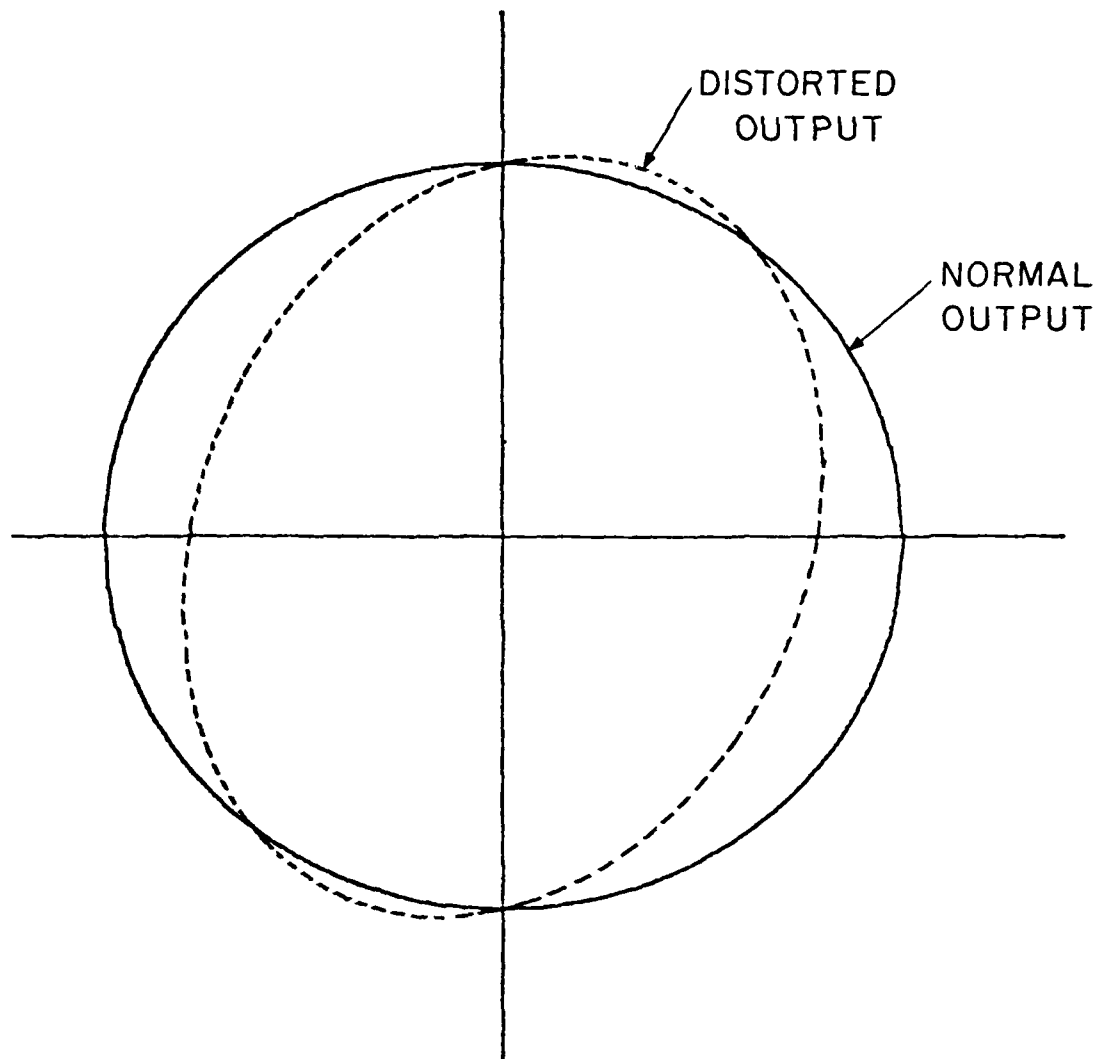


Fig. 2.14 Polar Display Error.

$$y' = \gamma x + \eta y \quad (2.31)$$

where x and y are the actual values while x' and y' are measured values. A perfect circle in the $x-y$ plane can be expressed in terms of x' and y' as

$$a + bx' + cy' + dx'^2 + ey'^2 + fx'y' = 0 \quad (2.32)$$

If y and y' axes coincide and scale y' such that $\beta = 0$ and $\eta = 1$, from Eqs. 2.30 and 2.31 the following is obtained:

$$x'^2 = \alpha^2 x^2 \quad (2.33)$$

$$y'^2 = \gamma^2 x^2 + y^2 + 2\gamma xy \quad (2.34)$$

and

$$x'y' = \alpha\gamma x^2 + \alpha xy \quad (2.35)$$

When Eqs 2.33 through 2.35 are substituted into Eq. 2.32 and the results are compared to the equation of a circle, the coefficients of the x^2 and y^2 terms should be equal to one and there should be no xy cross product term. This requires

$$2e\gamma + f\alpha = 0 \quad (2.36)$$

$$d\alpha^2 + e\gamma^2 + f\alpha\gamma = 1 \quad (2.37)$$

and

$$e = 1 \quad (2.38)$$

From Eqs. 2.36 and 2.38

$$\alpha = \frac{-2\gamma}{f} \quad (2.39)$$

which, when substituted into Eq. 2.37, gives

$$4d \frac{\gamma^2}{f^2} - \gamma^2 = 1 \quad (2.40)$$

or

$$\gamma^2 = \frac{1}{\frac{4d}{f^2} - 1} \quad (2.41)$$

Substituting Eq. 2.41 into Eq. 2.39 gives

$$\alpha = \frac{2}{\sqrt{4d - f^2}} \quad (2.42)$$

and

$$\gamma = \frac{-f}{\sqrt{4d - f^2}} \quad (2.43)$$

Using α and γ , Eqs. 2.30 and 2.31 become

$$x = \frac{\sqrt{4d - f^2}}{2} x' \quad (2.44)$$

and

$$y = y' + \frac{f}{\sqrt{4d - f^2}} x' \quad (2.45)$$

The values of a , b , c , d , e , and f can be obtained by measuring many points along the $|\Gamma| = 1$ circle using a sliding short and fitting the data to Eq. 2.32. Thus, measured results can be corrected for unequal channel gains and cross coupling in the polar display unit.

2.4.3. Test Fixture Due to the small size of microwave MESFETs, it is necessary to build a test fixture to hold the device and provide a transition from the device terminals to the network analyzer measurement ports. A microstrip test fixture was designed to permit establishing the reference plane right at the transistor terminals. The microstrip circuit was selected because this environment, with its inherent small size, light weight, and ease of fabrication, is well-suited for applications such as amplifiers and oscillators. Device

characterization in microstrip test fixtures avoids certain device-circuit interface parasitics which would be present if the device were characterized in another medium. The test fixture was designed to provide a 50- Ω environment to match with the 50- Ω measurement system.

The test fixture shown in Fig. 2.15 consists of two end pieces, two OSM tab connectors, and a rib. Each end piece accommodates an OSM connector and a microstrip circuit which is made of 0.025 inch thick 99.5 percent Al_2O_3 (alumina) substrate. For 0.025 inch thick alumina substrates, the width of a 50- Ω microstrip line is 0.025 inch and matches the width of the package leads of the transistor which is mounted on the rib by silver epoxy as shown in Fig. 2.16. The surface of the rib is lowered such that the transistor lead lays on the microstrip line. The fixture can be taken apart easily to test different transistors.

As explained earlier, at microwave frequencies it is often impossible to directly measure devices such as diodes and transistors at the device terminals. In such case, a test fixture is used and the measurements are made at a convenient point some distance away from the device. The plane where measurements are made is called the measurement plane and the two-port network connecting this plane and the device is called the coupling network. In this case the coupling network consists of the microstrip circuit, OSM connector, and necessary adapters to connect to the network analyzer measurement port. Since sample to sample variations contribute to errors, all connectors and adapters were individually labeled and all parts were assembled in the same manner each time. The coupling network could be characterized by the untermination process, and measurement results were transferred to the device terminal level by deembedding as outlined in Reference 27.

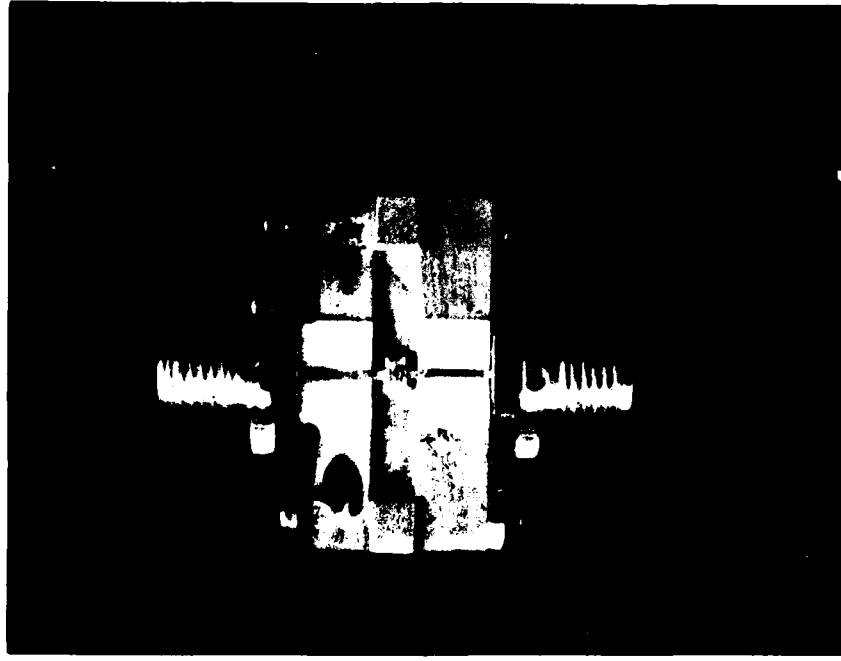


Fig. 2.15 GaAs MESFET Test Fixture.

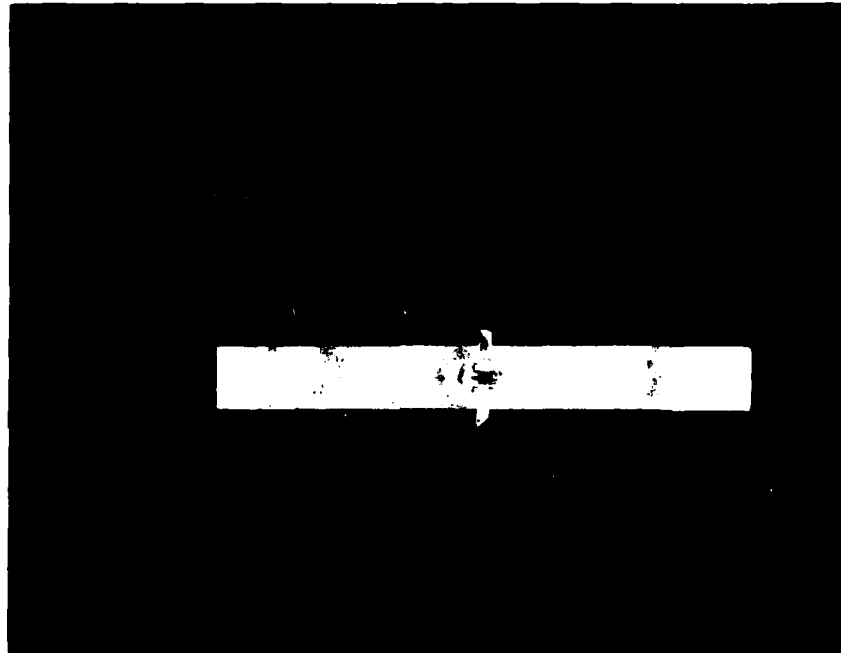


Fig. 2.16 GaAs MESFET Mounted on a Rib for Test.

A varactor was used as the known load at the reference plane because of its comparable size to the MESFET. The varactor was first measured for its capacitance vs. bias voltage on a capacitance meter. Then, it was mounted on a rib similar to that for the MESFETs and wire bonded to the test fixture. The varactor capacitance was set to a predetermined value by adjusting bias voltage through a bias tee connected at the input port of the reflection test unit and measured by the network analyzer. Since the varactor series resistance R_s and bonding wire inductance L_s from the microstrip to the varactor were not taken into account in this measurement, they were compensated for.

During the first step of untermination, the varactor was assumed lossless. A series resistance of $-R_s$ was in the embedding network and needed to be removed. By extending the bonding wire to the ground forming a short circuit and measuring the input impedance of the test circuit, the amount of series resistance could be determined. The real part of this input impedance is equal to $-R_s$ and the series inductance introduced by the bonding wire is calculated by

$$L = 5.08 \times 10^{-3} l \left(\ln \frac{4l}{d} - 1 \right) \quad (2.46)$$

where L is the inductance in nanohenries, l is the length of the bonding wire in thousandths of an inch, and, d is the diameter of the bonding wire in thousandths of an inch. The length of the bonding wire was measured accurately under a microscope. Once these terms are removed from the embedding network, a reference plane is established. It is not necessary to measure the device parameters at the chip level because the package is an integral part of the device.

2.4.4. Device Parameter Calculation The objective of large-signal device characterization is to determine the terminal conditions at each port. This can be achieved by measuring the reflection coefficient at each port. By using the deembedding process, the measured reflection coefficients can be transformed easily into the device terminal impedances. The power level at each port can be calculated from the amount of incident power. As described earlier, the incident power is monitored through a 20-dB directional coupler in the measurement setup. A circuit diagram showing the relationship between the incident power and the power delivered to the device under test is as shown in Fig. 2.17. The incident power P_{in} is

$$P_{in} = \frac{\left| \frac{E_G}{2} \right|^2}{Z_G + Z_o} \quad (2.47)$$

where E_G is the peak RF amplitude of the source voltage. With a matched source where

$$Z_G = Z_o \quad (2.48)$$

the incident power is expressed as

$$P_{in} = \frac{|E_G|^2}{8 Z_o} \quad (2.49)$$

The RF voltage at the measurement plane is

$$V_1 = E_G \frac{Z_1}{Z_1 + Z_o} \quad (2.50)$$

or

$$\frac{V_1}{E_G} = \frac{Z_1}{Z_1 + Z_o} \quad (2.51)$$

By using the ABCD parameters, the ratio between the voltages at the measurement plane V_1 and the reference plane V_2 is given by

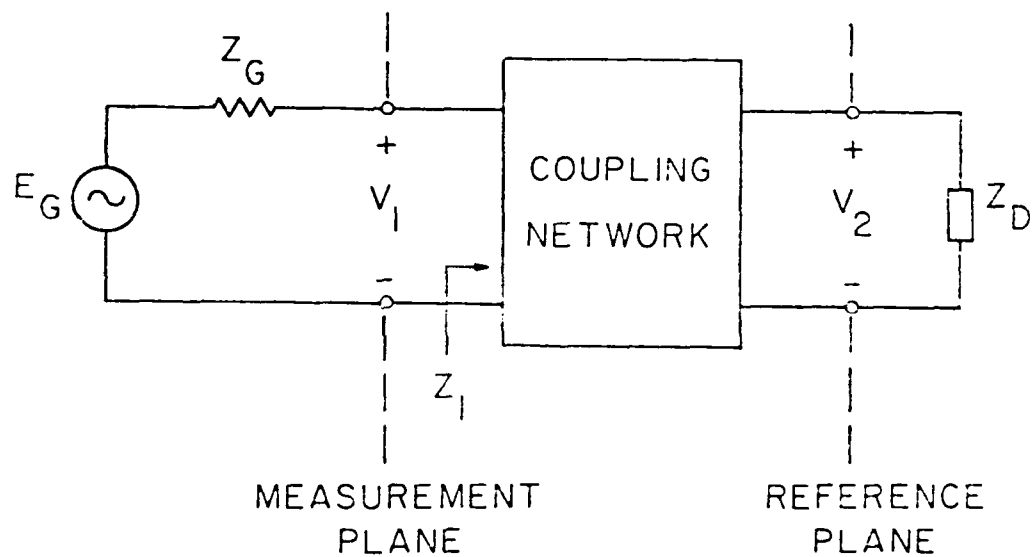


Fig. 2.17 Large-Signal Measurement Circuit Diagram.

$$\frac{V_2}{V_1} = \frac{Z_D}{(CZ_D + D) Z_1} \quad (2.52)$$

Thus from Eqs 2.51 and 2.52 the RF voltage across the device is calculated from

$$\frac{V_2}{E_G} = \frac{Z_D}{(CZ_D + D) (Z_1 + Z_o)} \quad (2.53)$$

When the incident power P_{inc} is known, the source voltage E_G can be obtained from Eq. 2.49 as

$$|E_G| = \sqrt{8Z_o P_{inc}} \quad (2.54)$$

From Eq. 2.53, V_2 is obtained as

$$V_2 = \frac{Z_D}{(CZ_D + D) (Z_1 + Z_o)} (8Z_o P_{inc})^{1/2} \quad (2.55)$$

The RF current at the device terminal is

$$I_2 = \frac{V_2}{(R_D^2 + X_D^2)^{1/2}} \quad (2.56)$$

and the power delivered is

$$P_{dev} = \frac{|I_2|^2 R_D}{2} \quad (2.57)$$

If the device is active, R_D is negative and Eq. 2.57 gives generated power. The impedance Z_D is found by deembedding.

2.5. Summary

The measurement technique presented was proven to be very effective in characterizing the large-signal properties of the two-port nonlinear devices. Although accurate measurement results can only be obtained through an automatic measurement system, it is possible to obtain a general view of the device behavior manually on the polar display by inverting the harmonic frequency converters. The harmonic frequency converter monitors both the incident and the reflected wave from the test unit, converts these two signals down from

the microwave frequency, and sends them to the network analyzer. For a reflection measurement, the ratio between the reflected and the incident waves at that port determines the reflection coefficient Γ as

$$\Gamma = \frac{b}{a} \quad (2.58)$$

where b is the reflected wave variable and a is the incident wave variable. If the harmonic frequency converter is inverted, the incident (reference) and reflected channels are interchanged such that a/b is measured, and the result provides the reciprocal of the reflection coefficient. The reflection coefficient Γ is expressed in terms of Z_L and Z_o as

$$\Gamma = \frac{Z_L - Z_o}{Z_L + Z_o} \quad (2.59)$$

or

$$\begin{aligned} \frac{1}{\Gamma} &= \frac{Z_L + Z_o}{Z_L - Z_o} \\ &= \frac{(-Z_L') - Z_o}{(-Z_L') + Z_o} \end{aligned} \quad (2.60)$$

When comparing Eqs. 2.59 and 2.60, it is found that by inverting the harmonic frequency converter, the impedance information given on the polar display is $-Z_L$, which is the desired load impedance of an active port. The insertion loss due to the coupling network can be compensated for by adjusting the network analyzer gain control, and the phase shift can be compensated for by varying the length of the line stretcher in the reflection test unit. Due to the difficulties in calibrating the network analyzer in this configuration, the full accuracy of the automatic system was not available while the harmonic converter was inverted.

CHAPTER III

EXPERIMENTAL RESULTS

3.1. Introduction

In this chapter the experimental results of the large-signal performance of the MESFETs are presented. Power MESFETs rated at 250 and 500 mW were used since these devices typically operate under large-signal nonlinear conditions. The MESFETs under test consist of several parallel cells to achieve the rated power capability. Shown in Fig. 3.1 is a 500-mW rated MESFET chip which has 12 gates connected in parallel, while a 250 mW device has six gates. The GaAs MESFET used in this measurement employs a flip-chip configuration. The device is mounted on a metal base which includes alumina standoffs and leads to provide ease of installation in the microstrip circuits. These devices typically operate at $V_{ds} = 5V$ and $V_{gs} = -2V$. Although a higher drain to source voltage was suggested by the manufacturer, this lower voltage is preferred to reduce the device failure rate during measurement. It was found that increasing the drain to source bias voltage had no significant effect on the device performance.

In order to show the large-signal properties of the MESFETs and to illustrate the application of such characterization results, the devices were measured and the results were used in designing an oscillator. It was found that in the common drain configuration both ports of the MESFET were active. This common drain configuration is ideal for oscillator applications. The tuning and output matching circuits can be designed without the complexity of a feedback loop. For this

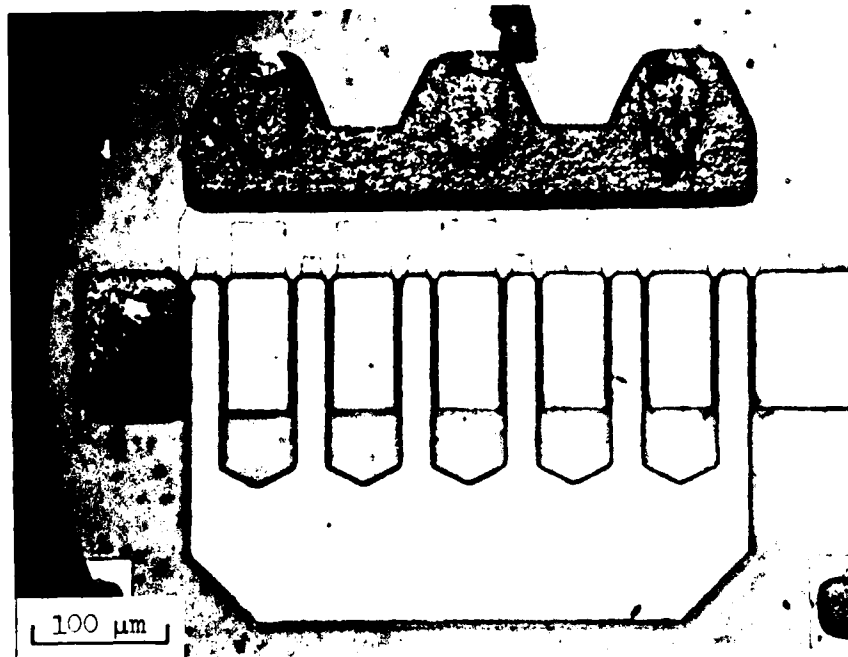


Fig. 3.1 500-mW Rated MESFET Chip.

reason, the MESFETs were characterized in this configuration. The devices were measured from 7 to 13 GHz at 1-GHz intervals under various power levels and loading conditions.

A substantial amount of data was generated by the measurement technique. These data were analyzed and are presented in this chapter. In Section 3.3 the design of a common drain MESFET oscillator is discussed. An oscillator was also built to verify the measurement results.

3.2. Measurement Results

The goal of the measurements is to determine the MESFET terminal conditions at both ports, specified by the terminal impedances, the terminal RF voltages and currents, and the net power crossing each port. During the measurements, the two test signals were first kept constant and the phase between them was varied. After making measurements at various phase settings, the test signal power levels were then changed. The power levels were varied from 10 to 300 mW for the 250 mW rated MESFETs and higher for the 500 mW rated devices. Since the measurement results were used to design a common drain MESFET oscillator, results were useful only when both ports were active. As the test signal power level increases, the device becomes saturated and the available power decreases gradually. The test signal power was increased until the gain diminished at either port.

The characterization technique used as many measurements as possible to cover the entire operating range. Many points were measured at each frequency and the results were stored on data cartridges for further analysis. Some typical measurement results are shown to illustrate the change of the device performance at different test signal power and phase settings. Measurement results are always presented in impedance pairs along with the corresponding available

power levels. Since the two terminal impedances depend on each other, they exist only in pairs and should never be separated. Because both ports were active, the real parts of their terminal impedances were negative and thus could not be plotted on a regular Smith chart. Therefore, the negative of these terminal impedances $-Z_{Tg}$ and $-Z_{Ts}$ were plotted. These impedances $-Z_{Tg}$ and $-Z_{Ts}$ are hence the load impedances required to achieve the measured device performances and thus can also be called the load impedances.

Figure 3.2 shows the loci of $-Z_{Tg}$ and $-Z_{Ts}$ at different source test signal levels at 7 GHz. The gate test signal was held constant at $P_{in1} = 160$ mW throughout this measurement. On each set of curves, three impedance pairs were marked and their corresponding available power levels were given. Curves 1 and 1' show the results as keeping the source test signal $P_{in2} = 240$ mW and varying φ . The source test signal was at 160 mW for curves 2 and 2' and at 100 mW for curves 3 and 3'.

Figure 3.3 shows the results obtained with the source test signal at $P_{in2} = 160$ mW and 7 GHz. Curves 1 and 1' indicate the loci of $-Z_T$ and $-Z_{Ts}$ with $P_{in1} = 100$ mW. Curves 2 and 2' are the results for $P_{in1} = 20$ mW and curves 3 and 3' are for $P_{in1} = 240$ mW. Typical measurement results at 10 GHz are as shown in Fig. 3.4. The source test signal was 10 mW for both sets of curves. For curves 1 and 1', the gate test signal was $P_{in1} = 30$ mW and curves 2 and 2' were measured with $P_{in1} = 20$ mW. Figure 3.5 shows two sets of measurements at 13 GHz. Both test signals were of 30 mW for curves 1 and 1' and 20 mW for curves 2 and 2'.

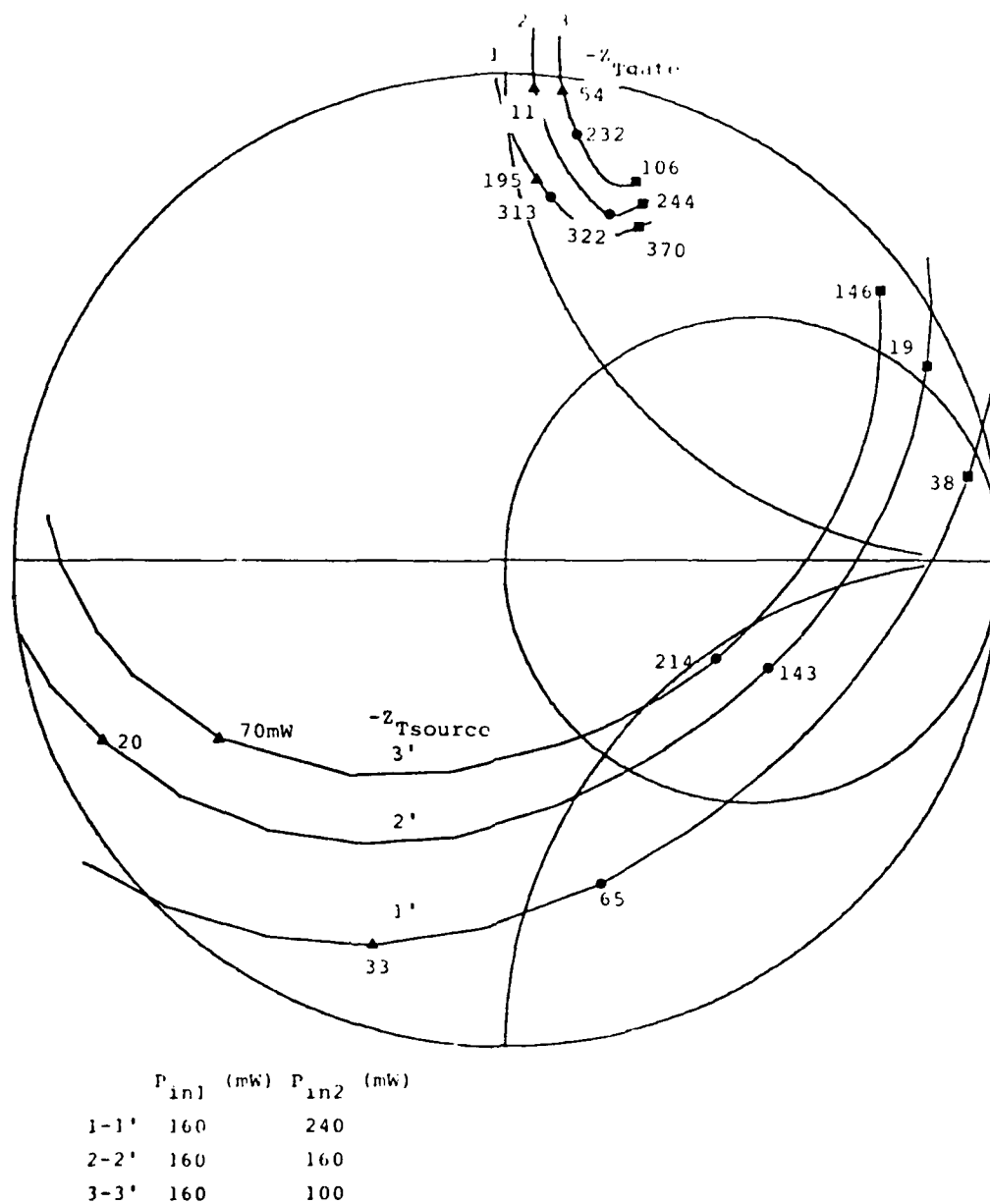


Fig. 3.2 Measured Gate and Source Terminal Impedances and Available Power at 7 GHz with Gate Test Signal at 160 mW.

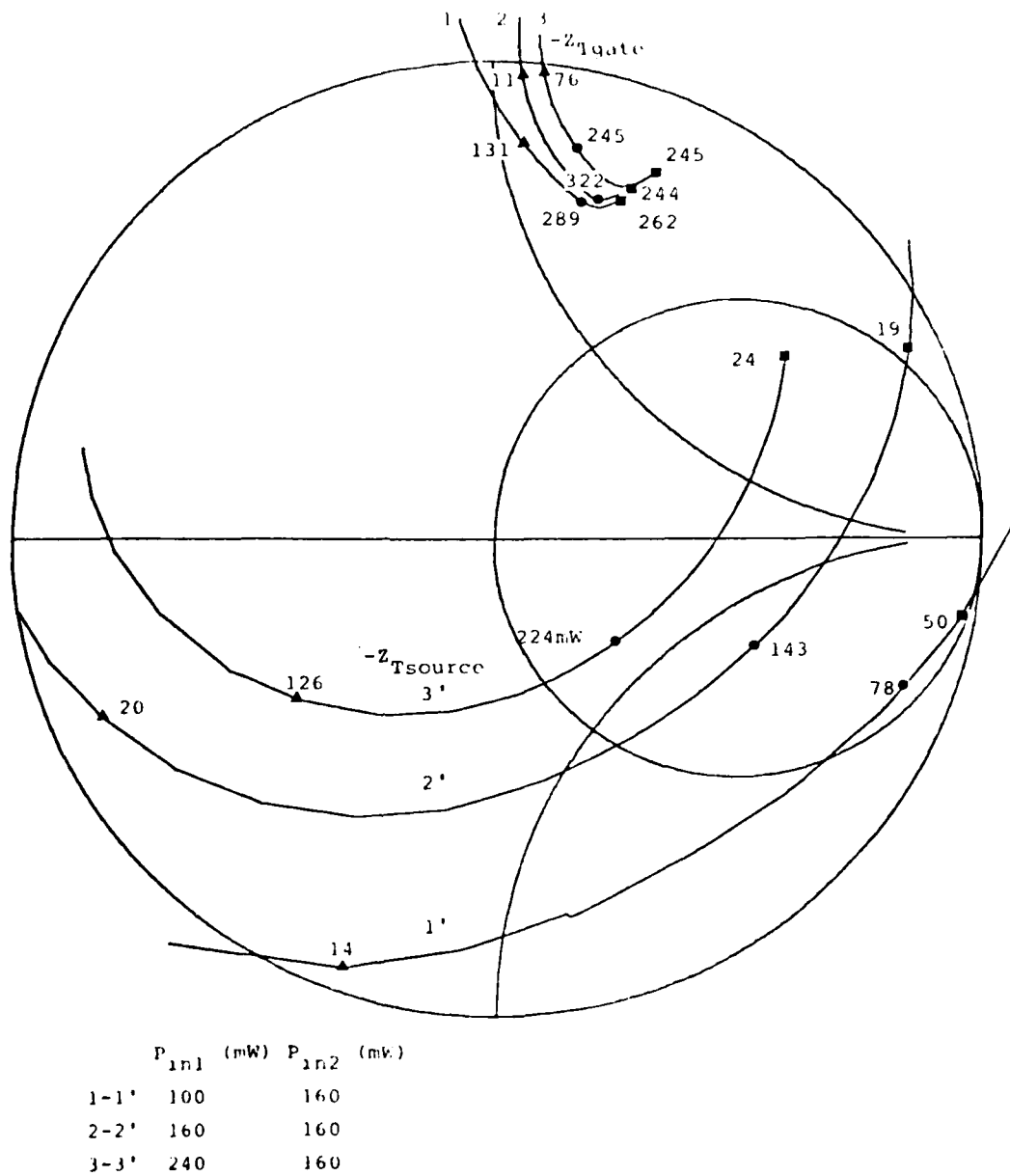
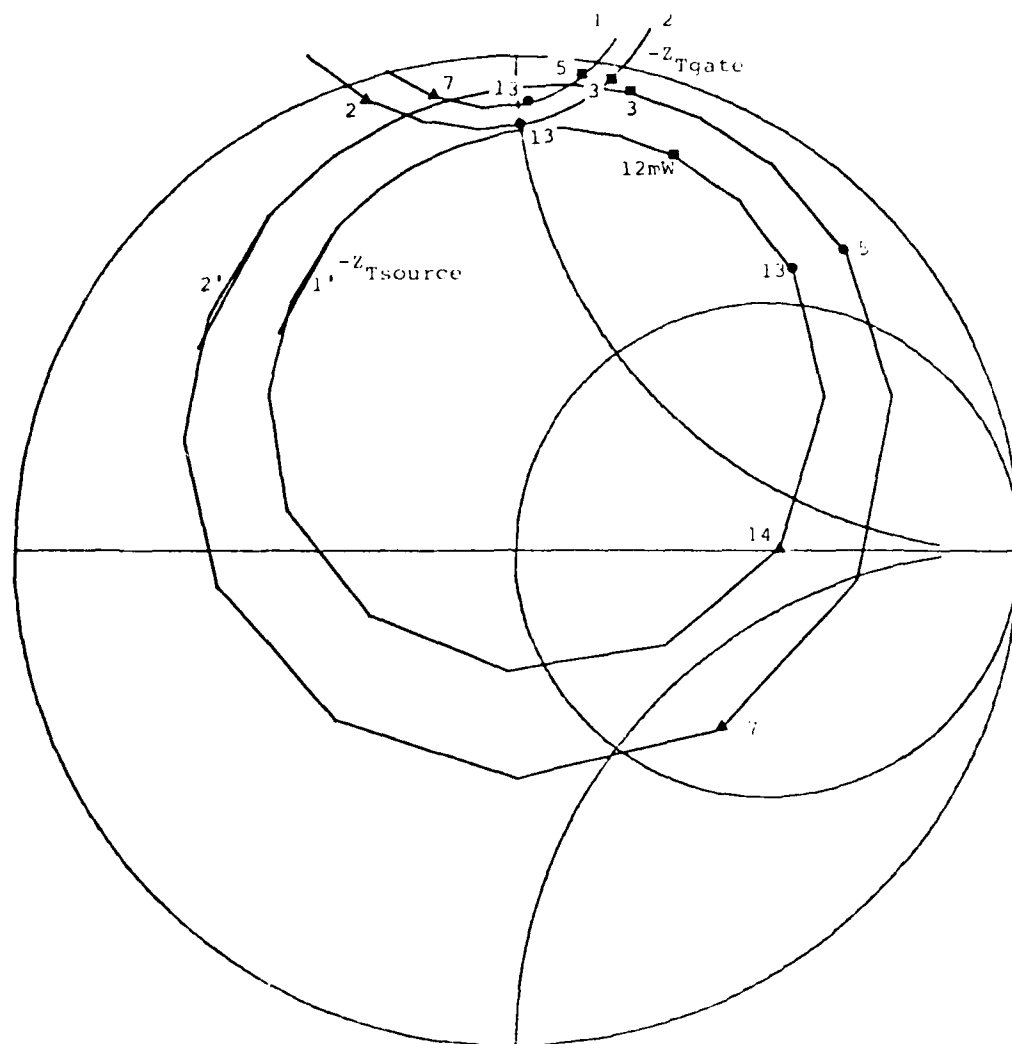


Fig. 3.3 Measured Gate and Source Terminal Impedances and Available Power at 7 GHz with Source Test Signal at 160 mW.



	P_{in1} (mW)	P_{in2} (mW)
1-1'	30	10
2-2'	20	10

Fig. 3.4 Measured Gate and Source Terminal Impedances and Available Power at 10 GHz.

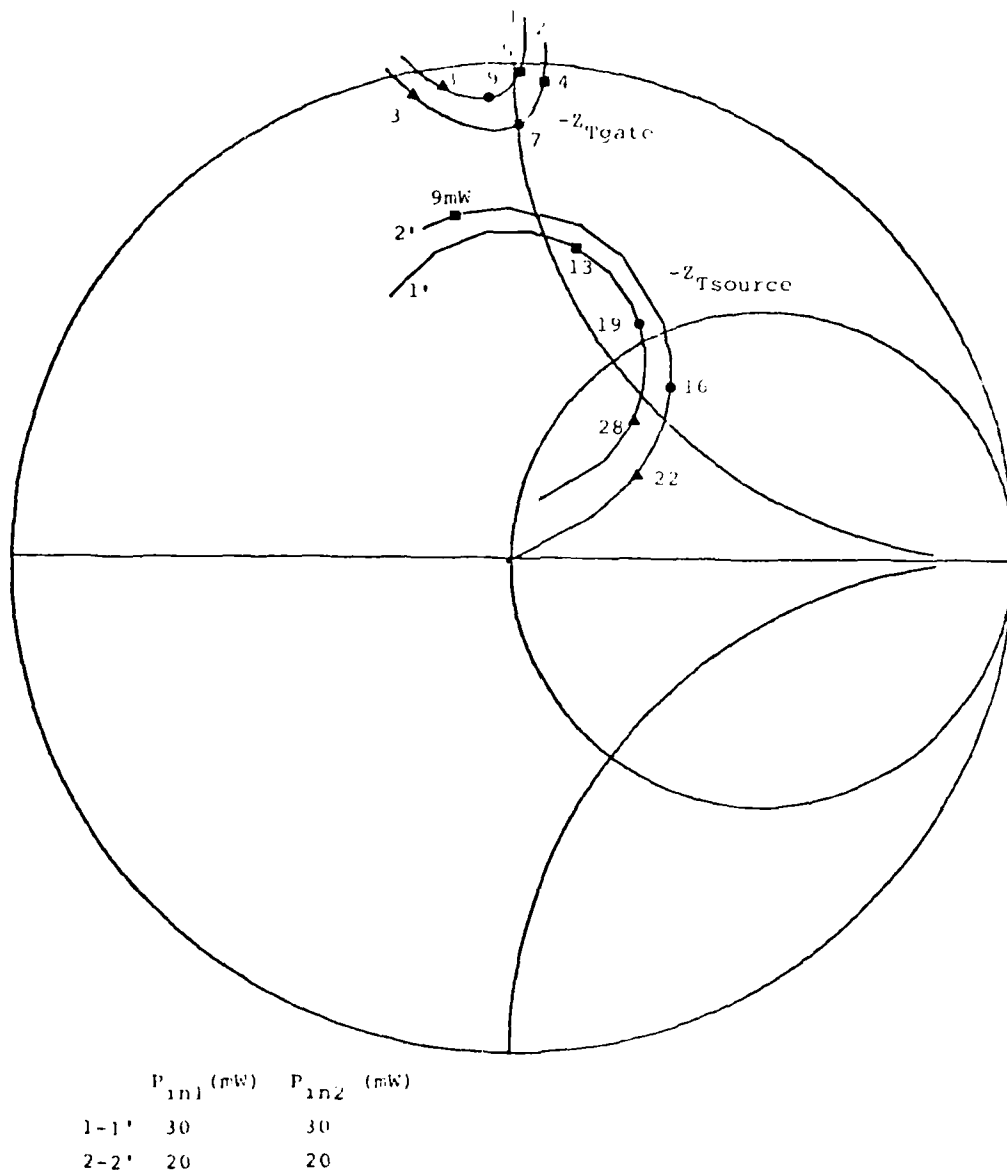


Fig. 3.5 Measured Gate and Source Terminal Impedances and Available Power at 13 GHz.

3.3. Common Drain MESFET Oscillator Design

3.3.1. Analysis of Measurement Results In the previous section, the measurement procedure and some sample results were presented. Since many measurements were made at each frequency, it is necessary to analyze and present the measured data in a systematic manner. The 250-mW rated devices were measured and presented for studying the large-signal device property. Because of sample to sample differences, all data used in this section for illustrating oscillator design were obtained from the same device.

From the measured results, it is observed that the MESFET tested is capable of delivering significant power either from the source or the gate side. Although the amount of power available from both ports are comparable, the optimum loading conditions for each case is different. The choice of output port depends on the requirements of the external circuitry. The test results revealed that the optimum gate load impedance was of low loss, while the source load impedance had a high resistive component. For most applications, it is preferred to have a low loss tuning circuit at the gate and a high impedance level at the source which is easier to match the standard $50\ \Omega$ system. Figure 3.6 shows the load impedance pairs needed to provide 100 mW output power at 7 GHz from the source. The same amount of power can also be obtained from the gate provided the load impedances shown in Fig. 3.7 are given.

Shown in Fig. 3.8 is the total output power $P_s + P_g$ vs. gate loss level at 7 GHz. The highest total power occurs for a lossless gate termination and essentially all the power is available from the source. As the loss in the gate circuit increases, the total power drops, with more of it dissipated in the gate termination. At high enough gate loss, the total power becomes dominated by gate power, and the source power drops substantially with a corresponding large

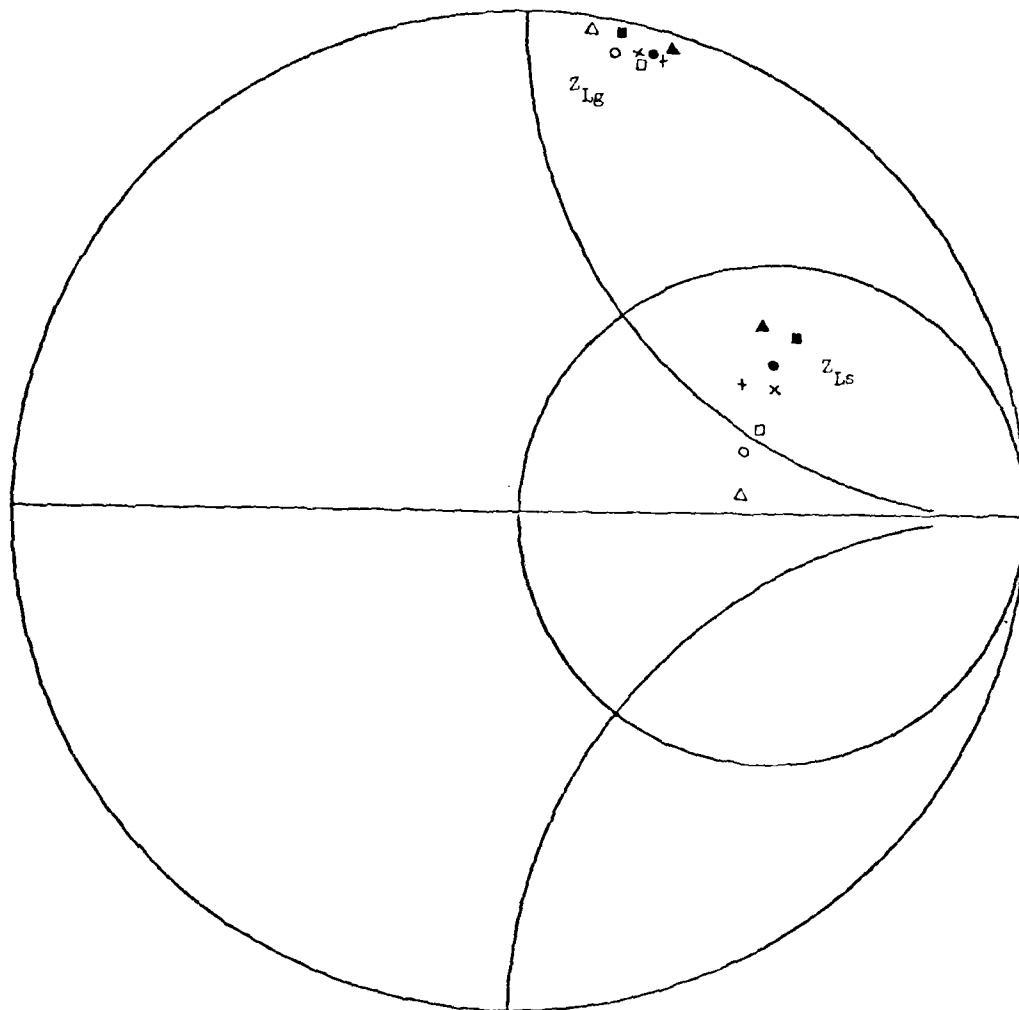


Fig. 3.6 Gate and Source Loading Conditions for Constant Source Output Power of 100 mW at 7 GHz.

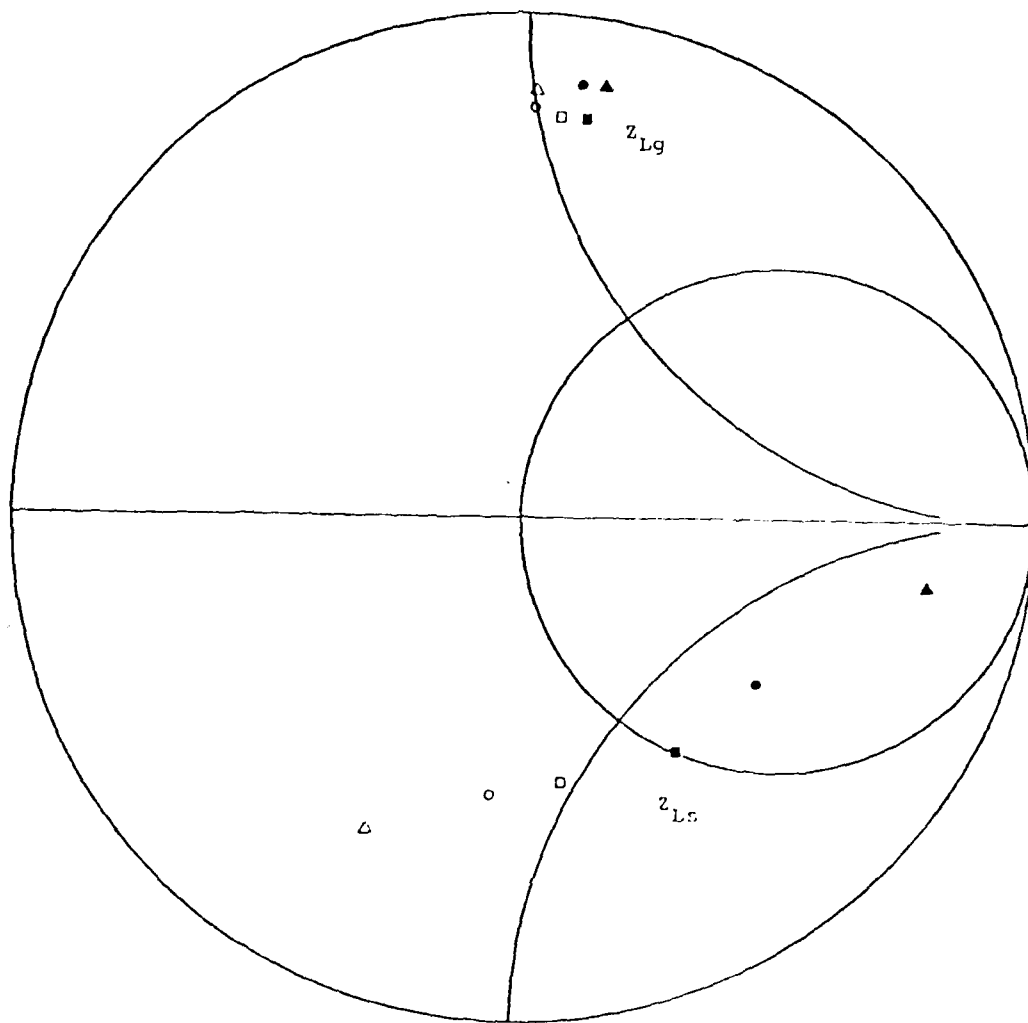


Fig. 3.7 Gate and Source Loading Conditions for Constant Gate Output Power of 100 mW at 7 GHz.

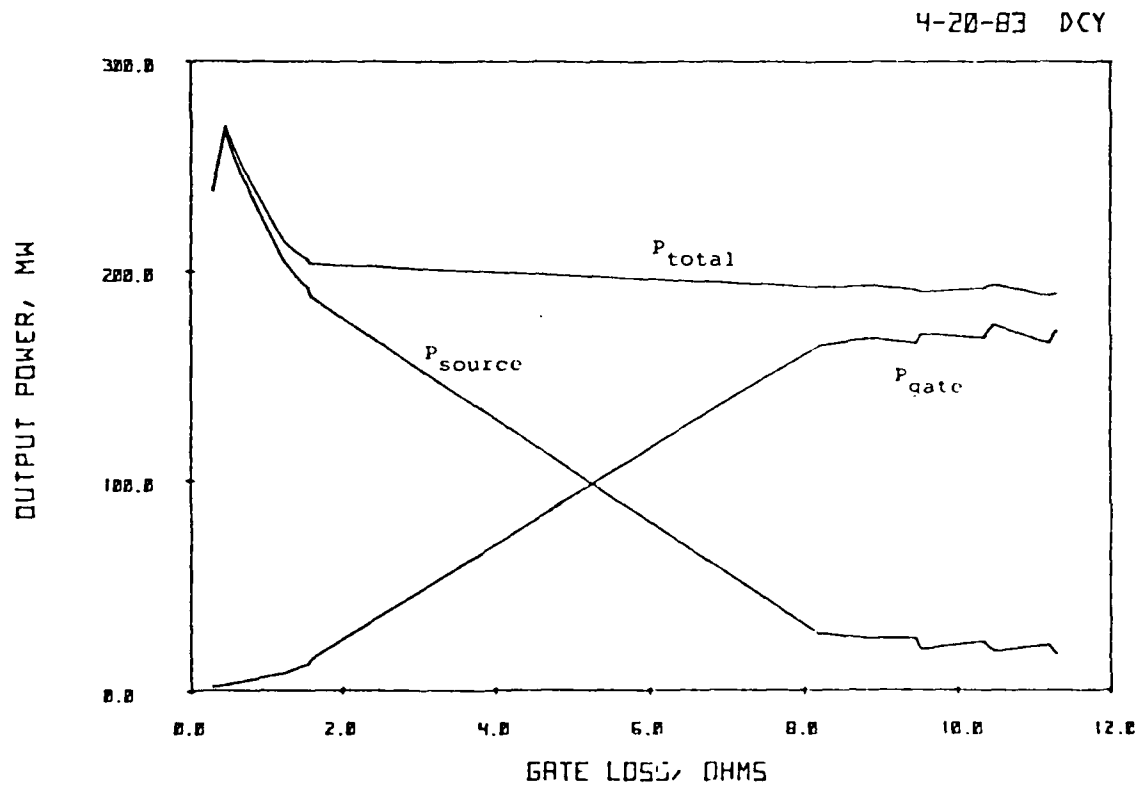


Fig. 3.8 Total Output Power vs. Gate Loss.

change in source load impedance. Shown in Fig. 3.9 are the source and gate load impedance regions corresponding to either the highest source power, Region A, or the highest gate power, Region B.

Figure 3.10 shows the source output power at 7 GHz as a function of the optimum gate load with increasing levels of gate loss resistance, i.e., tuning circuit loss. Hence for a varactor tuning circuit on the gate, the power output of the source and corresponding source load impedance can be specified for any given varactor resistance. As indicated for a series resistance of approximately $3\ \Omega$, the maximum power from the source has been halved to approximately 130 mW.

3.3.2. Oscillator Design Using Characterization Results The advantage of using the large-signal data for designing the oscillator is that these data provide accurate load impedance and available power information at both ports. In addition to the maximum power point, it also predicts the change of device performance while the load is varied. The measured data show that it is easier to use the gate as a tuning port and extract power from the source. From the measured data, it shows that maximum power can be obtained if the tuning circuit loss is minimized. Inevitably loss does exist. Therefore, in optimizing an oscillator circuit the first step is to design a low loss tuning circuit and then optimize the output circuit.

For each load at the gate, a different source load provides different output power. Figure 3.11 shows an example. With the gate load impedance set at $Z_{Lg} = 3 + j50\ \Omega$ and the source load impedances as indicated, the available power at the source ranges from 16 to 43 mW at 7 GHz as marked. The reactance part of the tuning circuit can be optimized easily to obtain the maximum power. As shown in Fig. 3.12, the same curve as in Fig. 3.11 was plotted at five

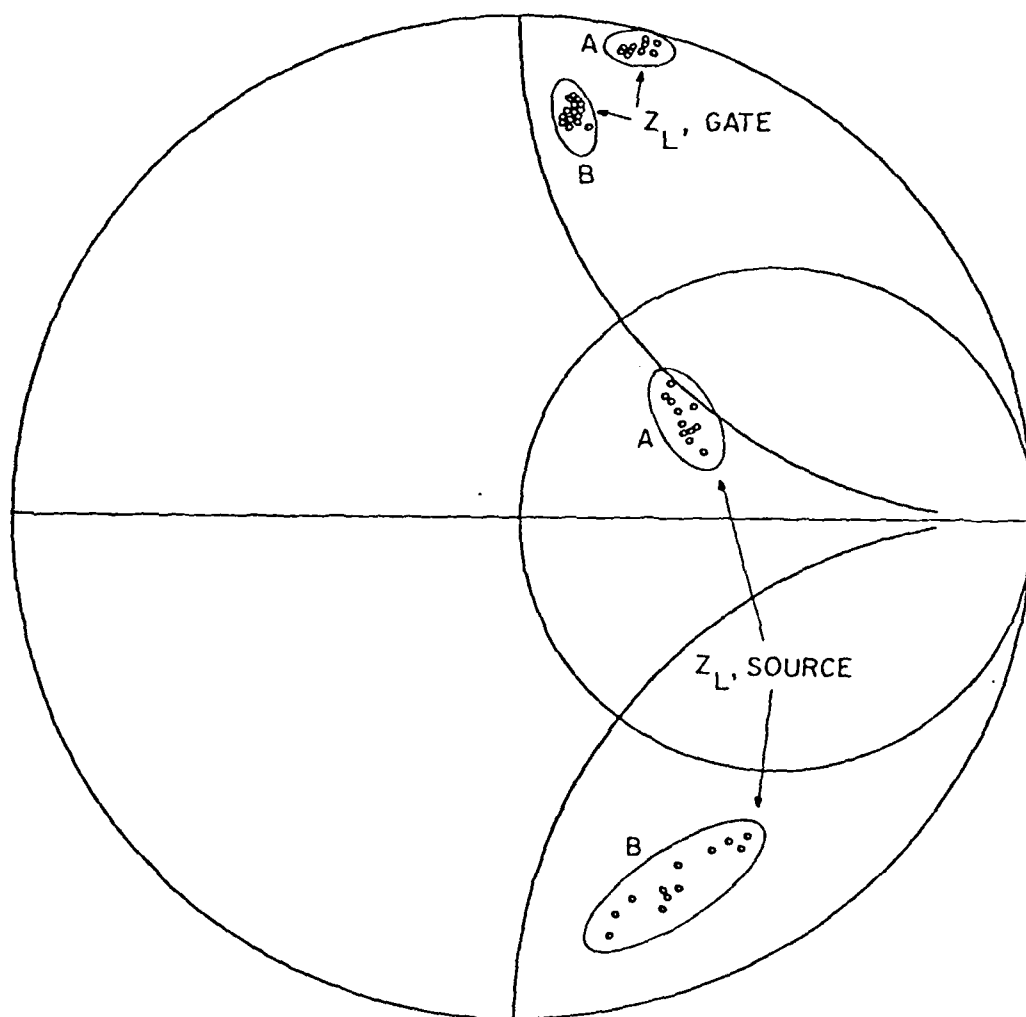


Fig. 3.9 Gate and Source Load Impedance Regions for Maximum Power at Either Port at 7 GHz.

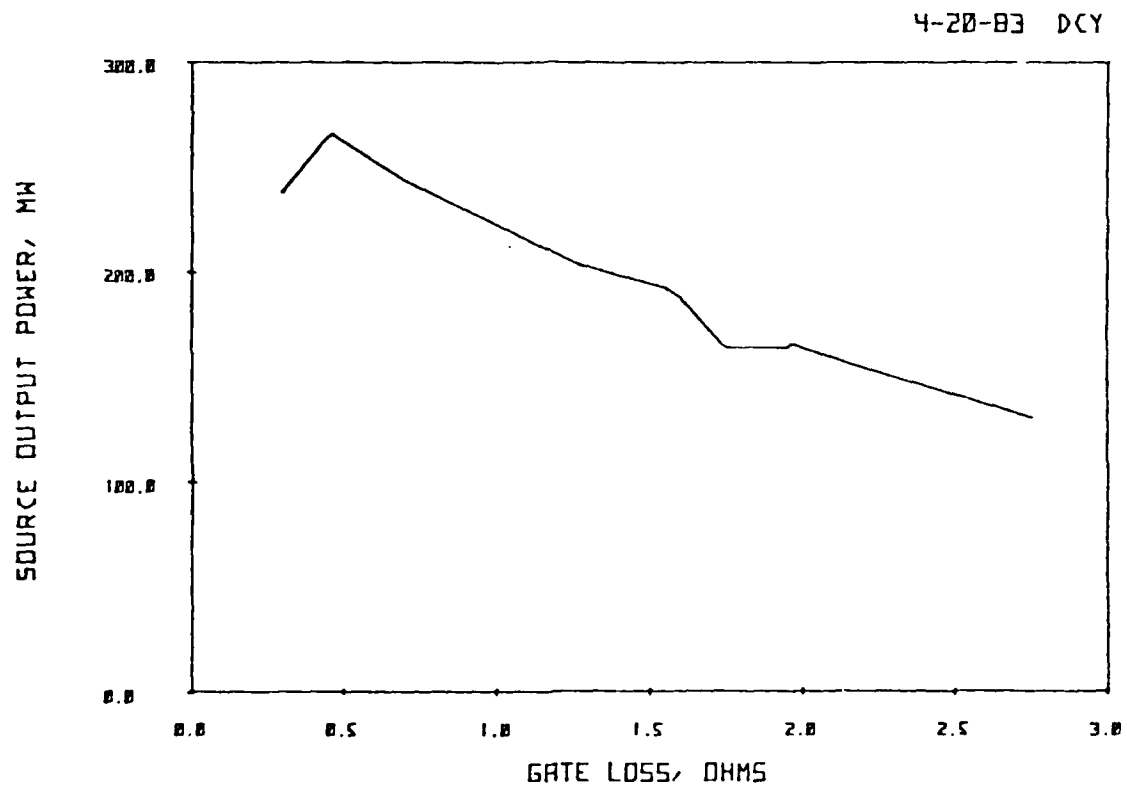


Fig. 3.10 Source Output Power vs. Gate Loss.

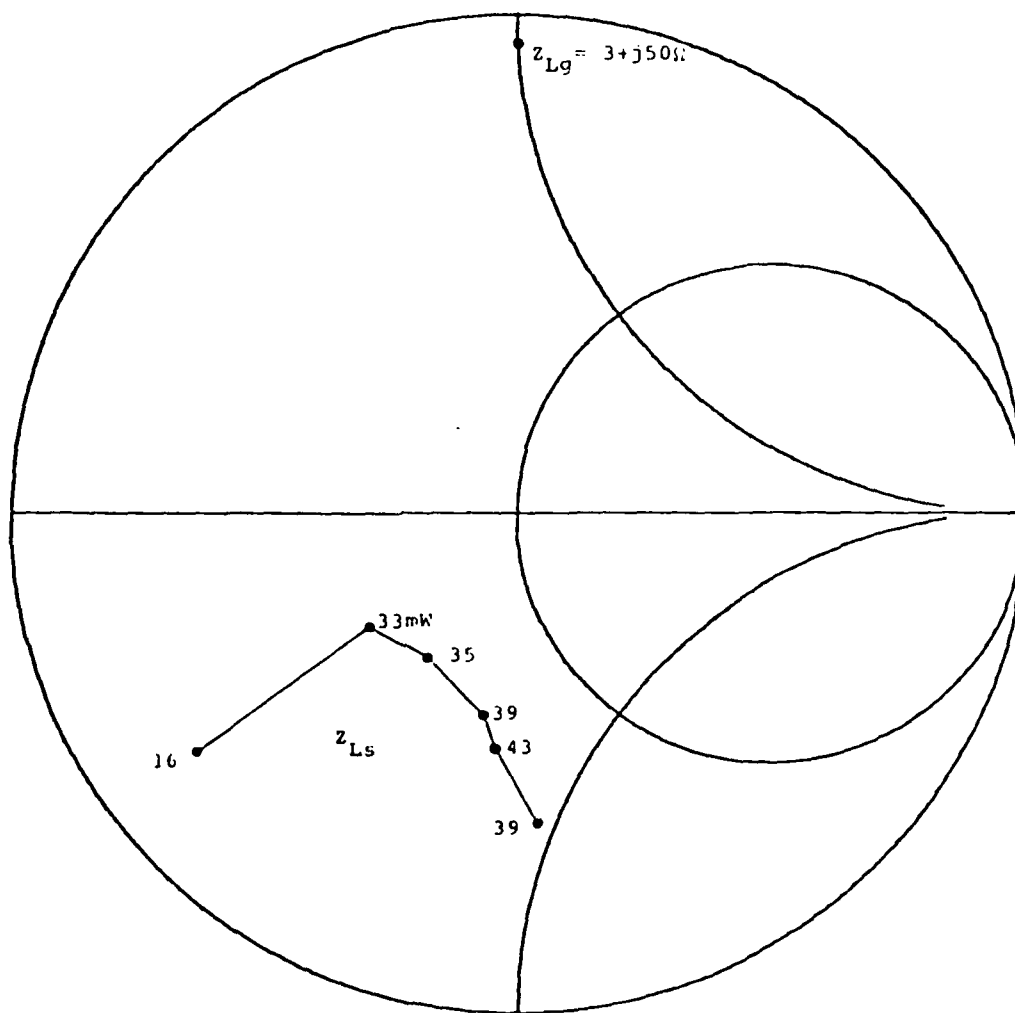


Fig. 3.11 Source Output Power vs. Source Load Impedance at 7 GHz.

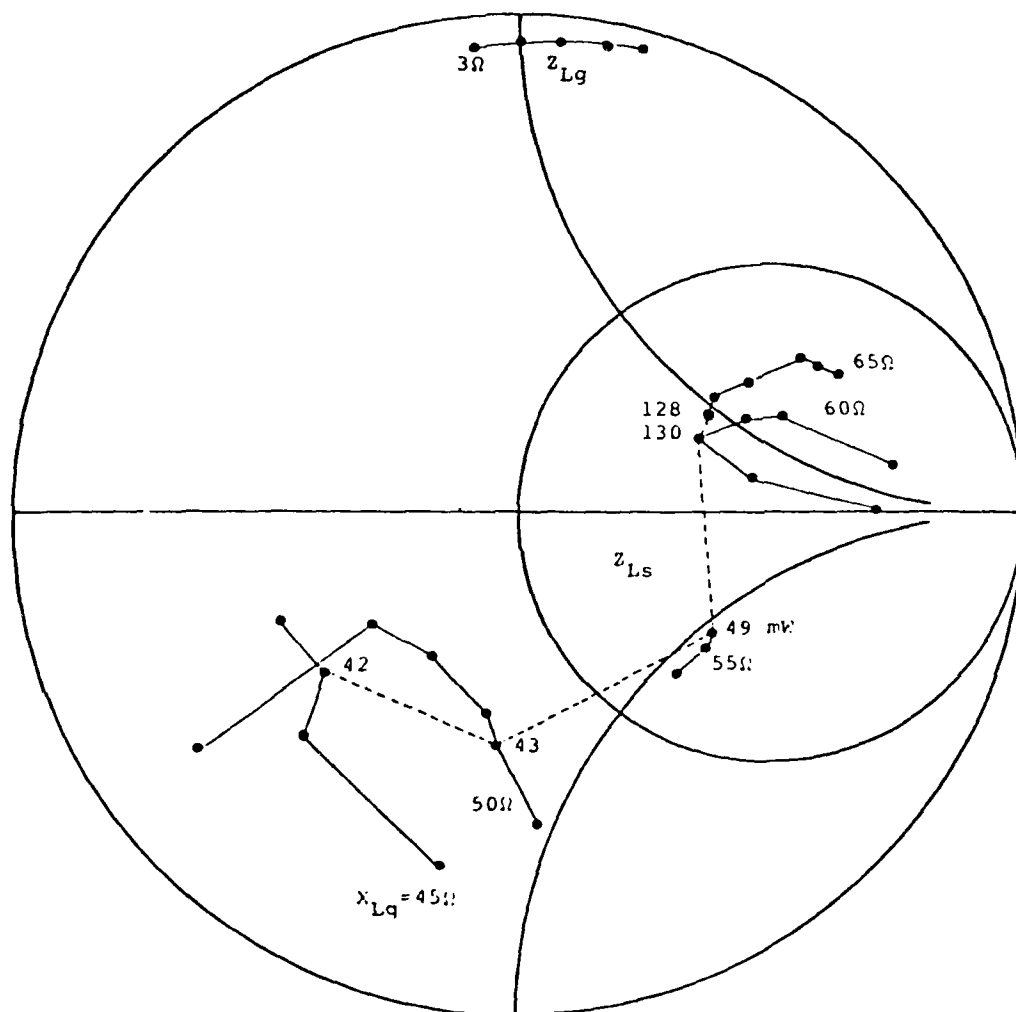


Fig. 3.12 Gate and Source Loading Conditions for a Constant Gate Loss of $3\ \Omega$ at 7 GHz.

different reactance levels with the resistive part constant at $3\ \Omega$. The maximum power point for each curve was labeled and all these points were connected to show the maximum output power available for each level of gate loss. Such curves were also obtained for gate loss levels of 0.5, 1.5, 5, 7.5 and $10\ \Omega$ at 7 GHz as shown in Figs. 3.13 through 3.17, respectively. These figures show that the maximum available power for each level of gate loss drops as the loss in the gate circuit increases. For a 0.5- Ω minimal loss at the gate, the maximum power is 266 mW, while the power decreases to 84 mW at $5\ \Omega$ and only 34 mW with a 10- Ω loss. By combining the maximum power curve at all gate loss levels, a graph as shown in Fig. 3.18 was constructed. It instantly reveals the maximum available power of the device at 7 GHz as a function of gate loss. The optimum gate and source load impedances are also indicated. By the same process, measured data at 8 to 11 GHz were analyzed and plotted. These results are presented in Appendix A.

Because of the broadband negative resistance available, MESFETs are widely used in voltage-controlled oscillators (VCOs). In designing an oscillator circuit, if both ports of the device are active, separate tuning and output circuits can be used, otherwise, a feedback loop is usually needed. For a broadband VCO, adding a feedback circuit to the tuning and output ports increases the complexity of the oscillator circuit. It is easier to use separate circuits for each port. According to the characterization results, the common drain configuration makes both gate and source ports active and is suitable for VCO applications.

After studying the gate and source impedances, it is obvious that the gate is preferred for tuning and the source, for output. A varactor is normally used for fast and wideband tuning of the VCO. By varying the the varactor bias voltage, the reactance of the tuning circuit changes and thus tunes the oscillator. For a given level of varactor series resistance (gate loss), the available source

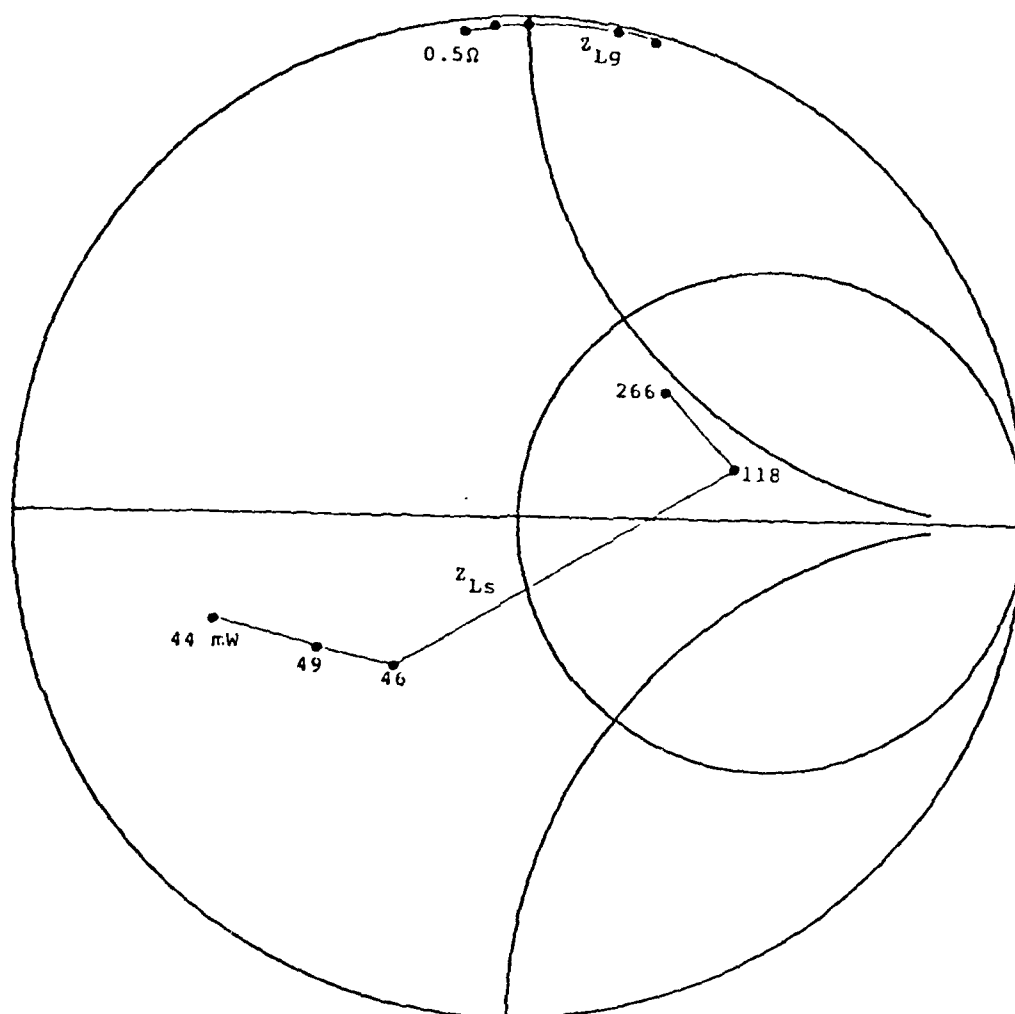


Fig. 3.13 Gate and Source Loading Conditions for a Constant Gate Loss of 0.5Ω at 7 GHz.



100

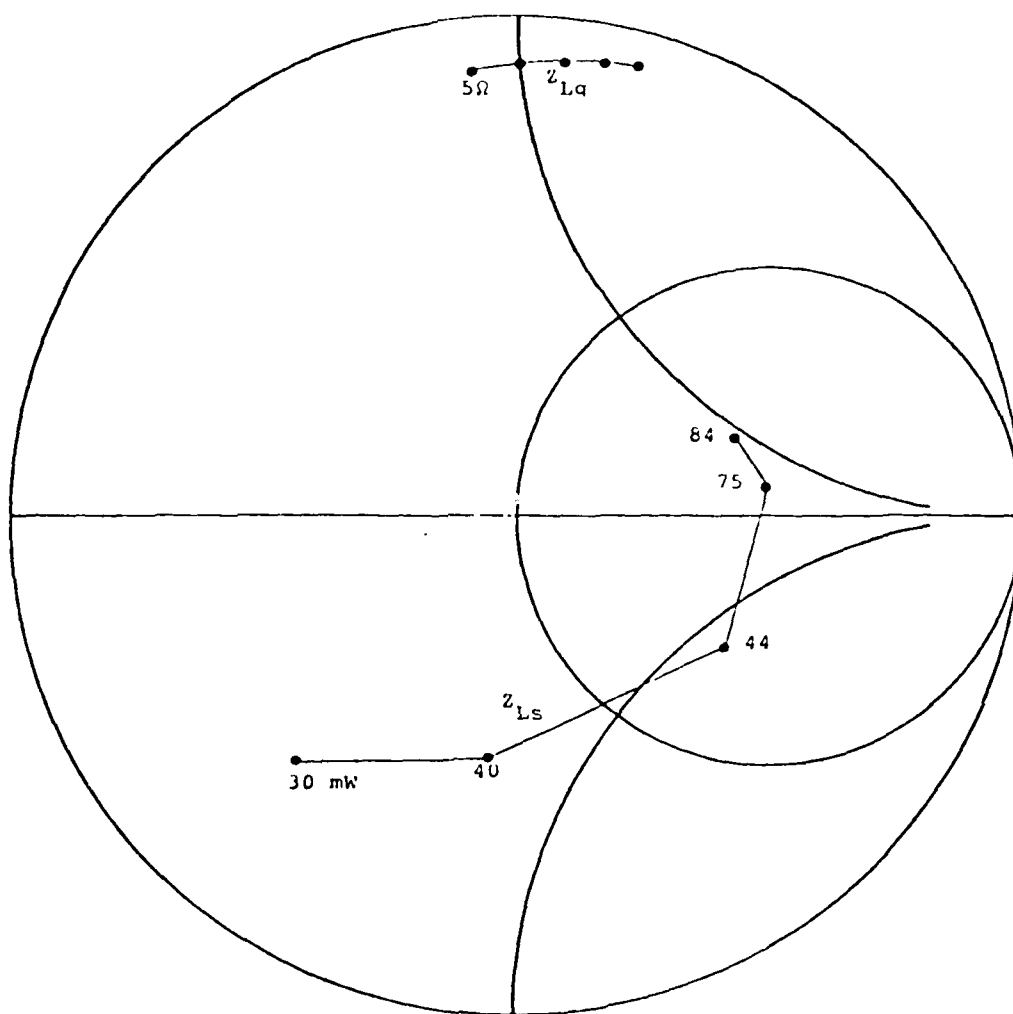


Fig. 3.15 Gate and Source Loading Conditions for a Constant Gate Loss of 5Ω at 7 GHz.

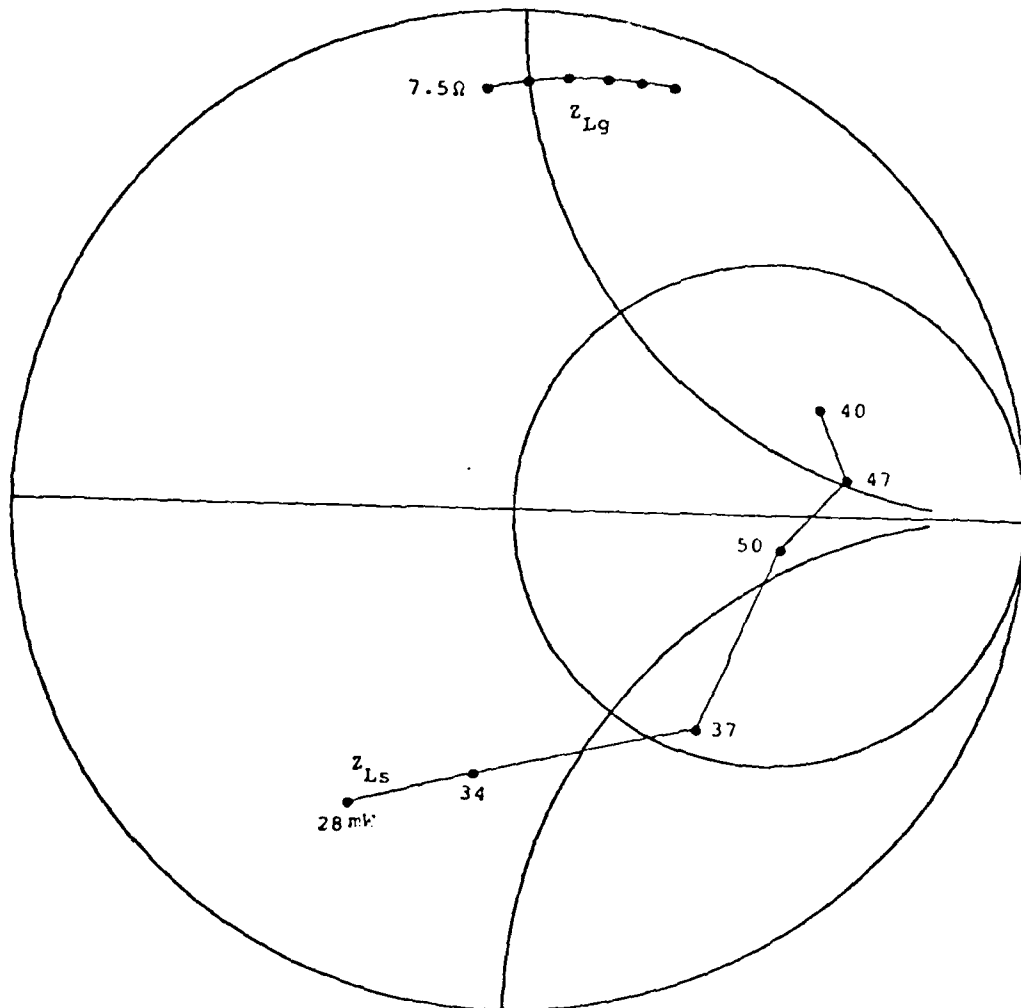


Fig. 3.16 Gate and Source Loading Conditions for a Constant Gate Loss of 7.5Ω at 7 GHz.

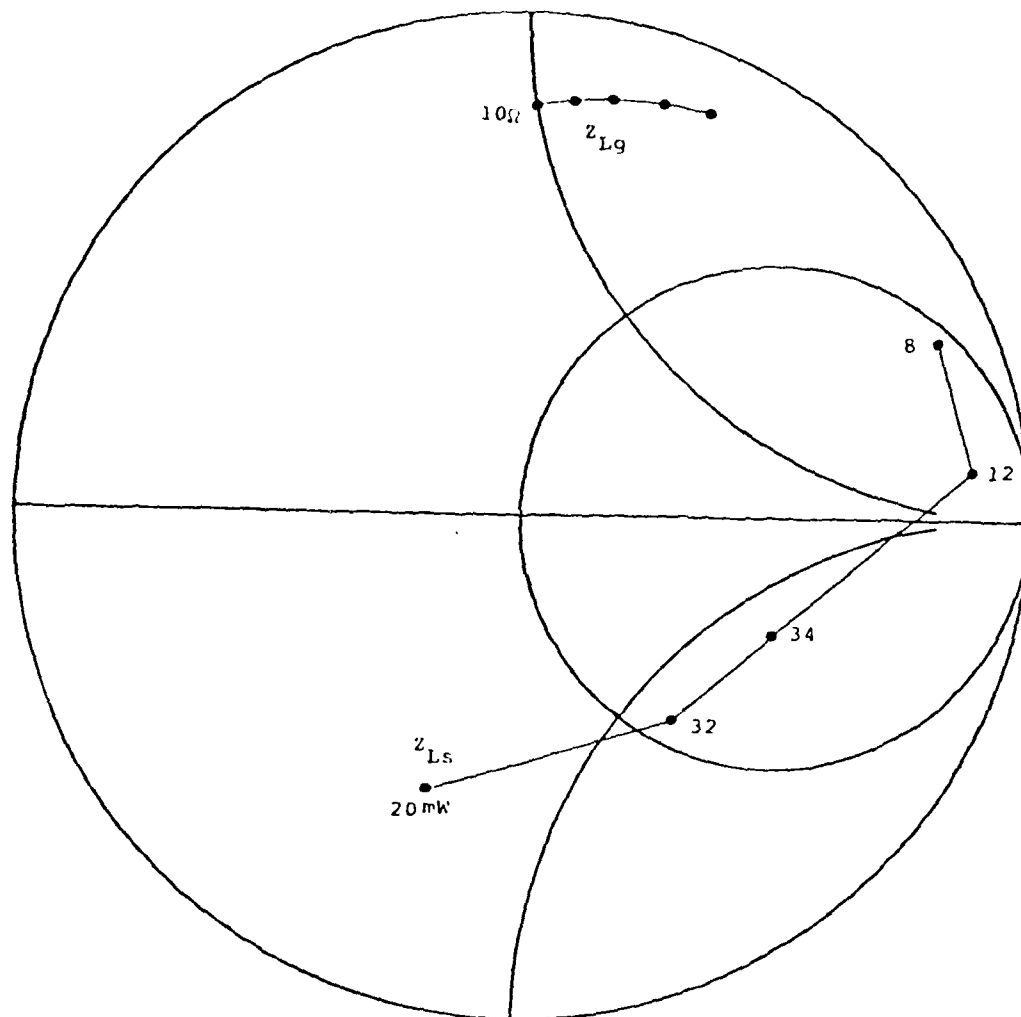


Fig. 3.17 Gate and Source Loading Conditions for a Constant Gate Loss of $10\ \Omega$ at 7 GHz.

power, the optimum source load, and the optimum gate reactance as a function of frequency can be determined thus leading to optimum VCO design. Shown in Fig. 3.19 is the optimum source load impedance and corresponding power output versus frequency for a $4\ \Omega$ level of gate resistance (varactor series resistance). The points along the $4\ \Omega$ contour indicate the optimum gate reactance necessary for tuning maximum power at each frequency. It is evident that the power output falls quite rapidly with frequency. Given the source load impedance characteristics which approximate the optimum, the VCO performance can be predicted and the gate circuitry can be specified.

3.4. Verification of Measurement Results

In the previous section, the oscillator design procedure by using the large-signal two-port measurement results was presented. However, the work is not complete without actually building an oscillator to verify the measurement results. The inventory of the type of device used for the measurement was exhausted before an oscillator could be constructed. A similar MESFET was used instead to build the oscillator. This device was then characterized by the same procedure at the frequency of oscillation and compared to the load impedances of the oscillator. A block diagram of the oscillator test circuit is shown in Fig. 3.20. The gate tuning circuit consists of a $50\text{-}\Omega$ microstrip line trimmed to the desired length and a bias circuit. A double stub tuner and a bias tee were used in the source output circuit. The oscillation frequency was measured at 7.2 GHz and the output power was 125 mW from the source. The oscillator circuit was then taken apart and the load impedances were measured on a network analyzer. The load impedances were $Z_{lg} = 0.5 + j2.5\ \Omega$ at the gate and $Z_{ls} = 21.85 - j40.18\ \Omega$ at the source. The output displayed on the spectrum analyzer is as shown in Fig. 3.21a, and Fig. 3.21b shows the second harmonic of

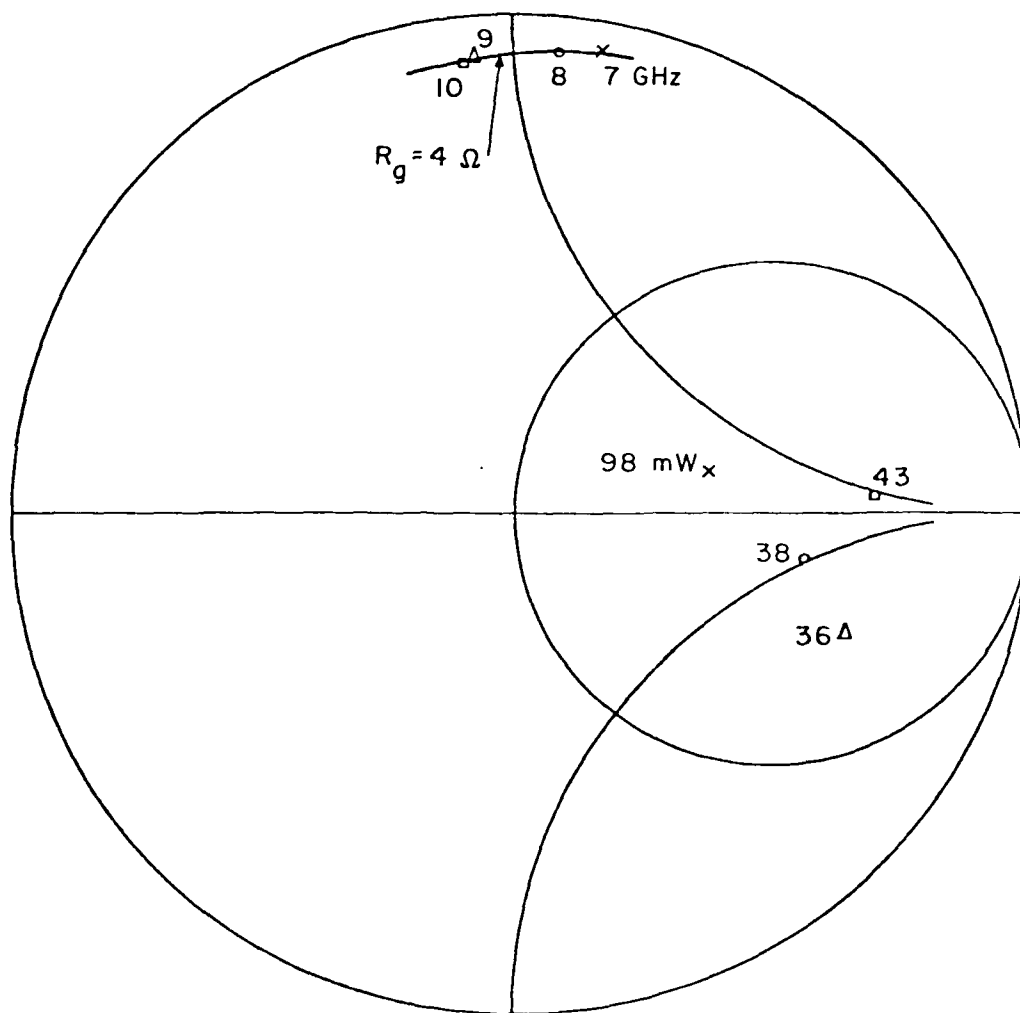


Fig. 3.19 Optimum Source Load, Output Power and Gate Reactance vs. Frequency for a 4-Ω Varactor Series Resistance.

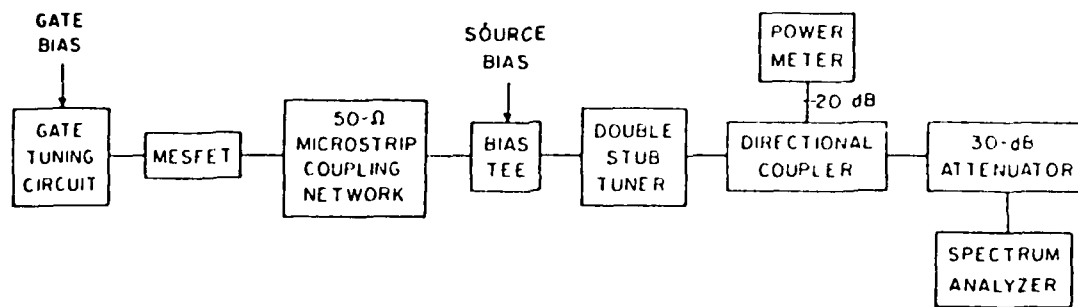
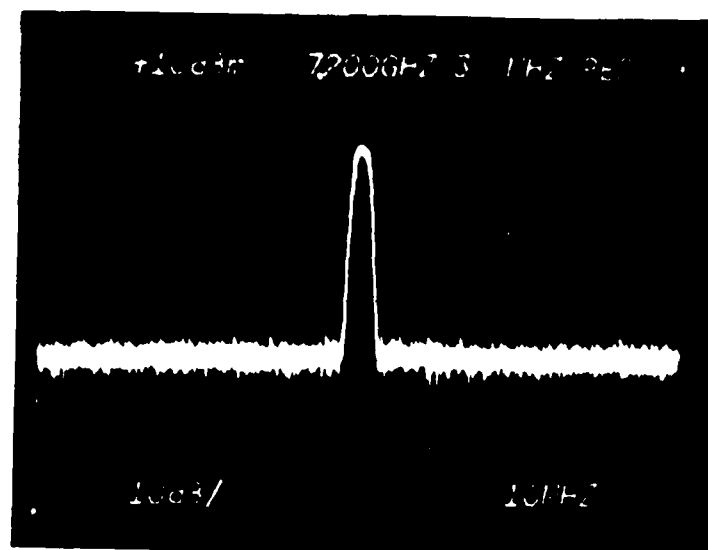
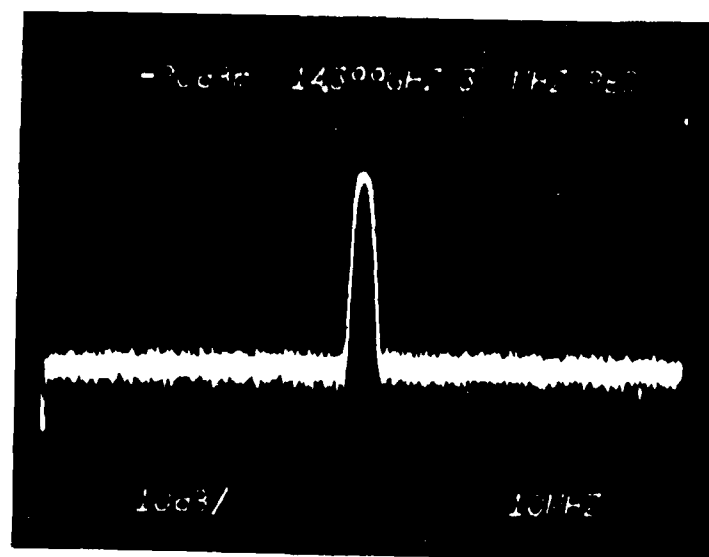


Fig. 3.20 Block Diagram of MESFET Oscillator Test Circuit.



(a)



(b)

Fig. 3.21 Spectrum of a 7.2-GHz Common Drain MESFET Oscillator at
(a) Fundamental Frequency, (b) Second-Harmonic Frequency.

the output, which is 32 dB lower than the fundamental. The impedance measurement results are illustrated in Fig. 3.22. The results show that the predicted loads from the measurement are very close to the loads actually used in the oscillator circuit. The differences between the two results are caused by the resolution and the error limits of the network analyzer measurement system. Therefore, this verifies that the large-signal two-port measurement can provide accurate information of the large-signal performance of two-port nonlinear networks.

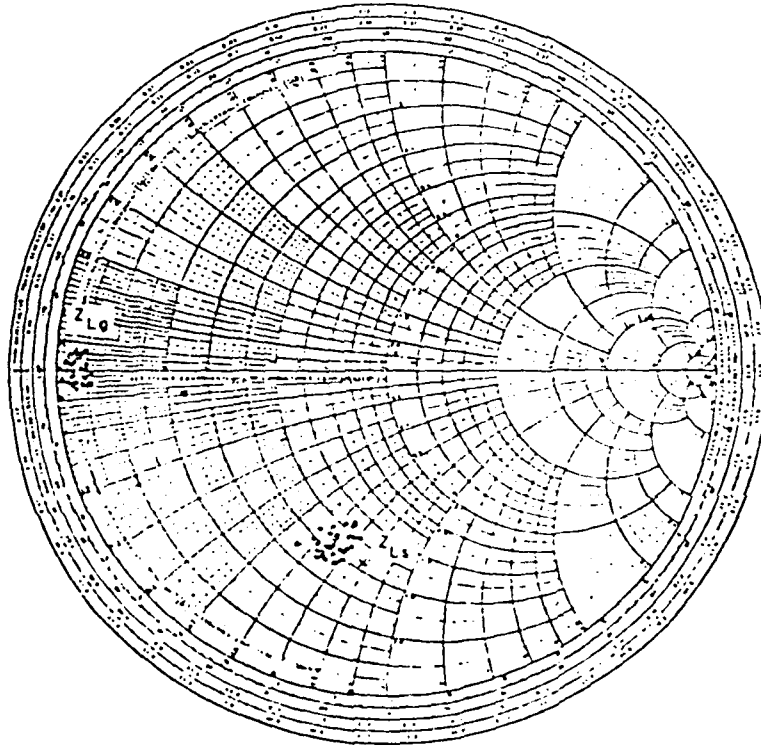


**Fig. 3.22 Measured Gate, Source Impedance, and Load Impedance Used
in the Test Circuit.**

CHAPTER IV

LARGE-SIGNAL MESFET MODEL

4.1. Introduction

In the previous chapters, the large-signal two-port characterization procedure and results were presented. Although accurate device information can be obtained through measurement, it requires substantial effort. An equivalent circuit model would be useful in predicting the large-signal device performance, if such a model and its parameters could be established easily. The available large-signal MESFET models are derived either from physical principles or measured data taken in a 50- Ω system. As such, they are not based on the actual device operating conditions.

The model reported by Tajima et al.,²⁸ for example, is based on the measured dc characteristics of the device. The nonlinear element values were calculated from dc measurement results. The drawback of this model is that the use of dc characteristics cannot always predict large-signal RF performance accurately. Madjar et al.²⁹ used the device geometry and semiconductor parameters to derive a device model. It is suitable for analyzing device physical parameters, but does not provide enough large-signal device information for circuit design. All these models require lengthy integration to calculate the element values.

In this chapter, the large-signal MESFET model element values are expressed as functions of the device terminal RF voltages. This model is easy to use because the device performance is directly related to the RF voltage values.

By using the large-signal characterization results, the accuracy of the model is also greatly enhanced.

4.2. Large-Signal MESFET Equivalent Circuit Model

The large-signal equivalent circuit model presented in this chapter is based on a simple model as reported in Reference 30 and is as shown in Fig. 4.1. Under large-signal operation, element values of the MESFET model vary with the driving levels and become dependent on terminal RF voltages. In order to limit the complexity of the model, the number of nonlinear elements was limited to three, namely: a transconductance g_m , a gate to source capacitance C_{gs} , and resistance R_{gs} . Because of the series connection of a large R_{gd} and a small C_{gd} , the impedance between the gate and the drain is high and large-signal effects from this branch are ignored. The drain to source resistance R_o and capacitance C_o are assumed constant. In a power MESFET the time delay τ is large and can be treated as a constant. The values of these five constant elements can be determined through small-signal measurements.

Since the device is packaged, the accuracy of the model is maximized by taking careful account of the package parasitics. Shown in Fig. 4.2 is the equivalent circuit used for package parasitics. Although a direct RF measurement of these package parasitics was not possible, their physical dimensions could be measured accurately with a microscope allowing reasonable values to be calculated. Table 4.1 shows the values of the device and the package parameters. Because the package and the linear model elements are constant they can be absorbed into the load at each port. The model is then simplified to that shown in Fig. 4.3.

The large-signal measurements were made in the common drain configuration and provided terminal impedance, RF voltage and available power at each port.

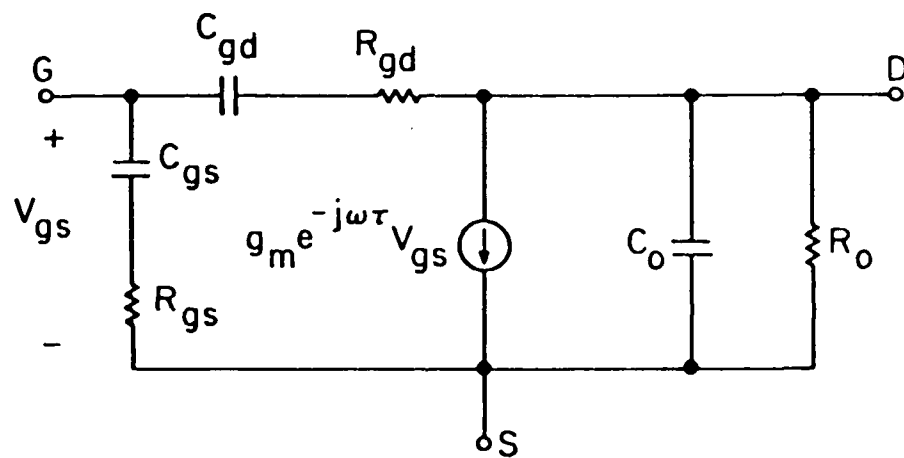


Fig. 4.1 MESFET Equivalent Circuit Model.

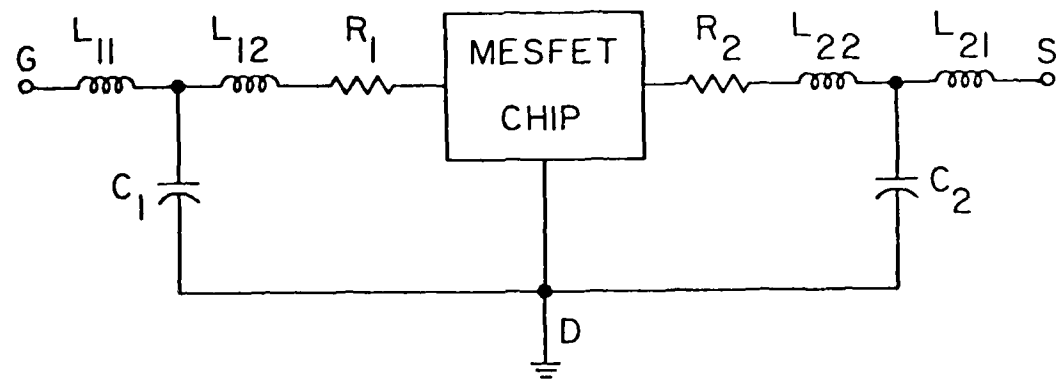


Fig. 4.2 Equivalent Circuit Model of MESFET Package.

TABLE 4.1

MESFET and Package Parameters

Drain Bias (V)	5.00
Gate Bias (V)	-2.00
R_{gd} (Ω)	71.05
C_{gd} (pF)	0.04
R_o (Ω)	25.0
C_o (pF)	0.03
τ (ps)	15.0
L_{11} (nH)	0.1
L_{12} (nH)	0.13
L_{21} (nH)	0.1
L_{22} (nH)	0.13
C_1 (pF)	0.045
C_2 (pF)	0.045
R_1 (Ω)	0.5
R_2 (Ω)	0.5

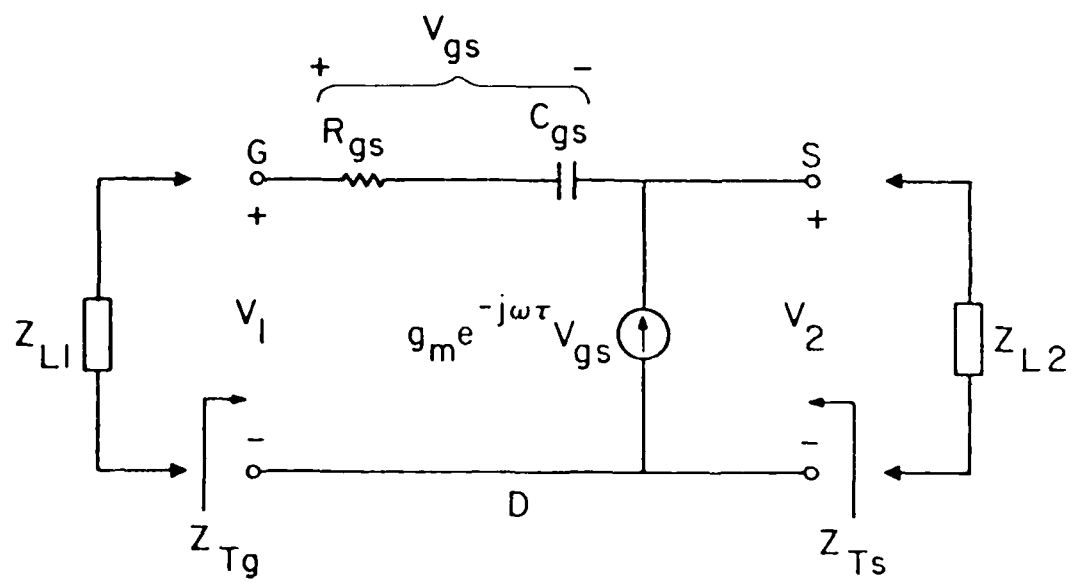


Fig. 4.3 Simplified Common Drain MESFET Model.

Based on the model in Fig. 4.3, the terminal impedances at the gate and source can be expressed as

$$Z_{Tg} = Z_{gs} - (1 + g_m e^{-j\omega\tau} Z_{gs}) Z_{Ts} \quad (4.1)$$

and

$$Z_{Ts} = \frac{-Z_{Tg} + Z_{gs}}{1 + g_m e^{-j\omega\tau} Z_{gs}} \quad (4.2)$$

The information obtained from measurements includes the simultaneous terminal impedances and the magnitude of the RF voltage at each port. Because the terminal impedance at the gate Z_{Tg} and the source Z_{Ts} depend upon each other, only one equation can be established and that is

$$\begin{aligned} Z_{gs} &= \frac{-Z_{Tg} - Z_{Ts}}{g_m e^{-j\omega\tau} Z_{Ts} - 1} \\ &= \frac{Z_{Tg} + Z_{Ts}}{1 - g_m e^{-j\omega\tau} Z_{Ts}} \end{aligned} \quad (4.3)$$

In order to solve Z_{gs} , the phase relationship between the two ports must be determined. Although this phase relationship was not available from the measurement results, additional required information can be extracted from the RF voltages $|V_1|$ and $|V_2|$. An iteration method was employed to solve these unknowns. The relationship between $|V_1|$ and $|V_2|$ is given by

$$\frac{|V_2|}{|V_1|} = \left| 1 + \frac{Z_{gs}}{Z_{L1}} \right| \quad (4.4)$$

where

$$Z_{L1} = -Z_{Tg} \quad (4.5)$$

An initial value was given to g_m and it was used to calculate Z_{gs} by Eq. 4.3. Then Eq. 4.4 was used to check the values of Z_{gs} until the conditions set by both equations were satisfied. When using this iteration method, the solution

must be to determine if it is unique or otherwise correct. Equation 4.4 can be written as

$$Z_{gs} = |Z_{f1}| |V| e^{j\theta} - Z_{f1} \quad (4.6)$$

where $|V|$ is the ratio between $|V_2|$ and $|V_1|$. Both Eqs. 4.3 and 4.6 can be plotted in the Z_{gs} plane and the intersection is the solution for Z_{gs} and g_m as shown in Fig. 4.4. By using bilinear transformation, circles and lines always transform into circles and lines.³¹ From Eq. 4.3, the locus of Z_{gs} , as a function of a real number g_m , forms a circle which goes through the origin as g_m approaches $+\infty$ or $-\infty$. To find the radius and the center of the locus both the numerator and the denominator of Eq. 4.3 are divided by $e^{-j\omega\tau} Z_{Ts}$ which yields

$$\begin{aligned} Z_{gs} &= \frac{-\frac{(Z_{Tg} + Z_{Ts})}{Z_{Ts}} e^{j\omega\tau}}{g_m - \frac{e^{j\omega\tau}}{Z_{Ts}}} \\ &= \frac{a + jb}{g_m + c + jd} \end{aligned} \quad (4.7)$$

where

$$a = \operatorname{Re} \left[-\frac{(Z_{Tg} + Z_{Ts})}{Z_{Ts}} e^{j\omega\tau} \right] \quad (4.8)$$

$$b = \operatorname{Im} \left[-\frac{(Z_{Tg} + Z_{Ts})}{Z_{Ts}} e^{j\omega\tau} \right] \quad (4.9)$$

$$c = \operatorname{Re} \left[-\frac{e^{j\omega\tau}}{Z_{Ts}} \right] \quad (4.10)$$

and

$$d = \operatorname{Im} \left[-\frac{e^{j\omega\tau}}{Z_{Ts}} \right] \quad (4.11)$$

Since the locus of Z_{gs} goes through the origin, the diameter of the circle is

AD-A142 462

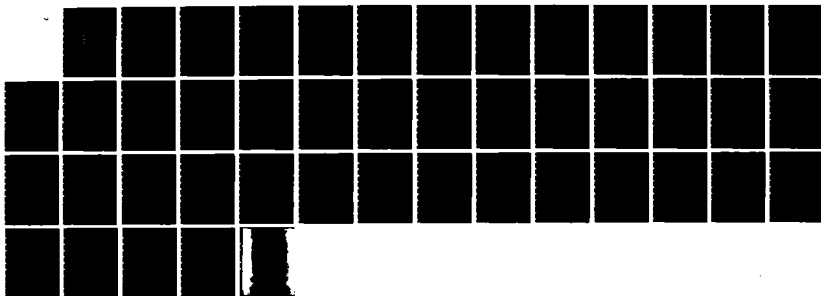
LARGE-SIGNAL CHARACTERIZATION OF NONLINEAR TWO-PORT
ACTIVE NETWORKS(U) MICHIGAN UNIV ANN ARBOR ELECTRON
PHYSICS LAB D C VANG APR 84 TR-163 AFMNL-TR-84-1034
F33615-81-K-1429

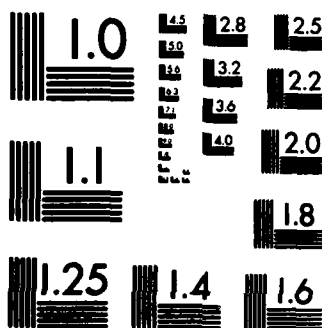
2/2

UNCLASSIFIED

F/G 9/5

NL





MICROCOPY RESOLUTION TEST CHART
NATIONAL BUREAU OF STANDARDS-1963-A

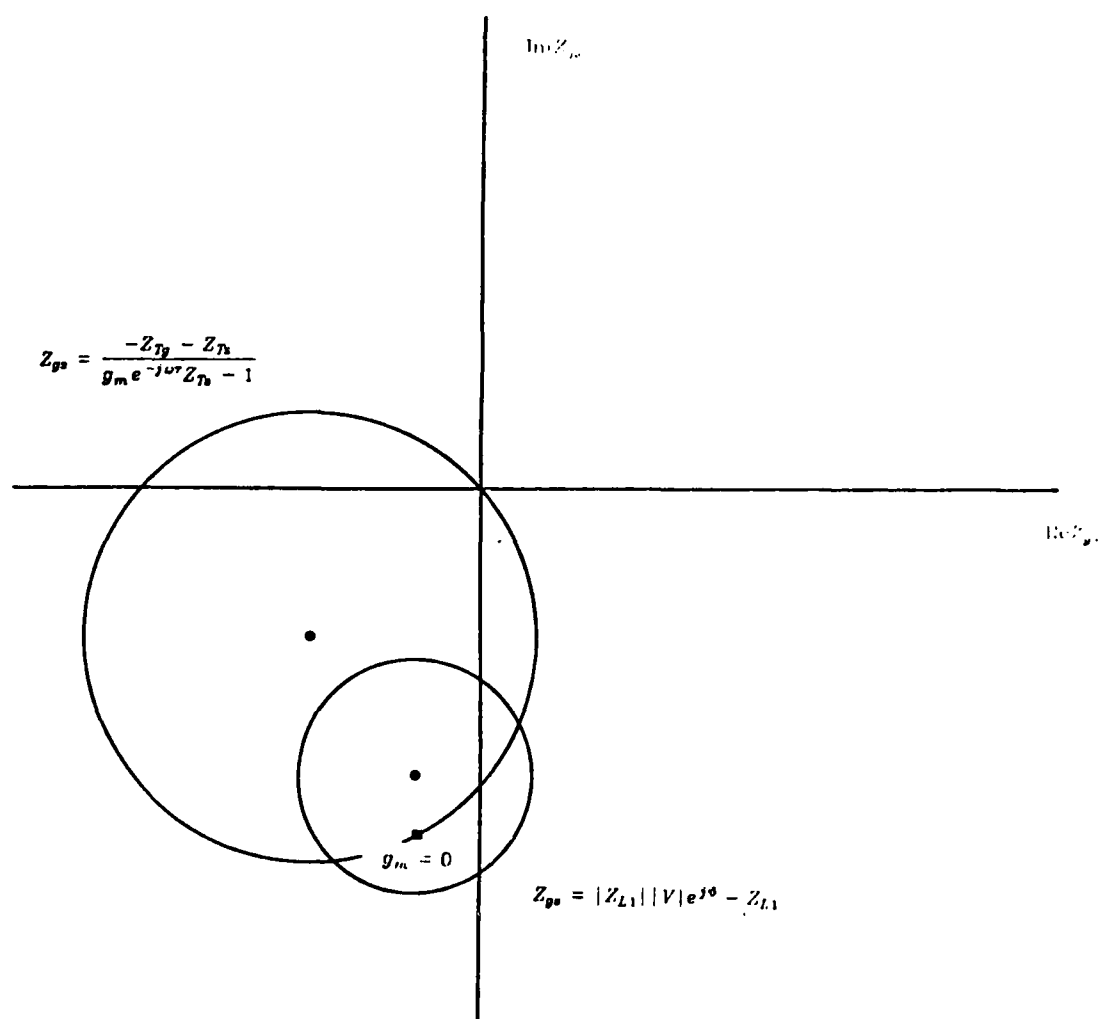


Fig. 4.4 Graphic Solution of Z_{gs} and g_m .

$|Z_{gs}|_{\max}$, where $|Z_{gs}|$ is

$$|Z_{gs}| = \frac{(a^2 + b^2)^{1/2}}{[(g_m + c)^2 + d^2]^{1/2}} \quad (4.12)$$

By observing Eq. 4.12, $|Z_{gs}|$ reaches its maximum at $g_m = -c$. Thus, the radius is $(a^2 + b^2)^{1/2}/d$. The center is half way between the origin and the $g_m = -c$ point, which is $a + jb/2jd$. The actual values can be obtained by equating Eqs. 4.8 through 4.11.

The locus of Eq. 4.6 also forms a circle as a function of ϑ , with the center located at $-Z_{L1}$ and a radius of $|Z_{L1}||V|$. Unless these two circles coincide, there are at most two solutions of these two equations. Since the solution must be unique, quantities obtained from this numerical method must be studied and the correct solution identified. In order to obtain the appropriate solutions for both Z_{gs} and g_m , the following criteria were established. The constraint for Z_{gs} is that it must be passive and capacitive, i.e., $Re(Z_{gs}) > 0$ and $Im(Z_{gs}) < 0$. This solution requires one intersection in the fourth quadrant as shown in Fig. 4.4. The transconductance must be real and positive where the value of $\omega\tau$ is given. In addition, g_m should not be greater than its small-signal value of 200 *mmho*. Even with these constraints it is still not possible to determine whether the solution will be unique. For this reason, during the calculation of Z_{gs} and g_m , both solutions were tested and only those meeting the above criteria were kept. Almost all the measured data gave one positive and one negative g_m as the sample printout shows in Table 4.2.

The results showed that both R_{gs} and C_{gs} are functions of the magnitude of the RF voltage between the gate and source $|V_{gs}|$ which is defined by

$$|V_{gs}| = |V_1 - V_2| \quad (4.13)$$

The values of R_{gs} and C_{gs} can be curve fitted. A polynomial of second degree

TABLE 4.2

Calculated Values of Transconductance

Positive Solutions		Negative Solutions	
trk	0	trk	0
file	1	file	1
F =	70000000000	F =	70000000000
	0.028		-0.004
	0.028		-0.003
	0.028		-0.003
	0.029		-0.004
	0.030		-0.004
	0.032		-0.006
	0.165		-0.041
	0.086		-0.031
	0.061		-0.024
	0.046		-0.018
	0.039		-0.013
	0.036		-0.011
	0.033		-0.008
	0.031		-0.007
	0.030		-0.006
	0.181		-0.042
	0.090		-0.032
	0.067		-0.026
	0.051		-0.020
	0.044		-0.016
	0.040		-0.014
	0.035		-0.010
	0.034		-0.008
	0.032		-0.007
	0.030		-0.005
	0.029		-0.004
	0.028		-0.002
	0.030		-0.002
	0.163		-0.041
	0.087		-0.031
	0.050		-0.020
	0.040		-0.014
	0.034		-0.010
	0.031		-0.006
	0.029		-0.004
	0.028		-0.003
	0.031		-0.004
	0.160		-0.041

in V_{gs} as shown in Fig. 4.5 was used to fit R_{gs} where the dots represent the calculated values from the measurement results. Since C_{gs} decreases with increasing $|V_{gs}|$, it was fitted to an exponential function and is as shown in Fig. 4.6. It was found that the transconductance g_m is a function of both $|V_{gs}|$ and $|V_2|$. Thus the g_m was fitted to exponential functions in V_{gs} for different values of $|V_2|$. Figure 4.7 shows the calculated values from measurements and the fitted curve at 7 GHz with $|V_2| = 5$ V. A complete set of g_m for various $|V_2|$ levels is shown in Fig. 4.8.

Element values of this model were also calculated at 8 and 9 GHz. These results are presented in Appendix B. It was noticed that the values of these nonlinear elements have similar values and vary in the same direction vs. RF voltage for all three frequencies.

This model can be used in a number of different ways. For example, the output load impedance and the input excitation level can be specified and this model can be used to predict the output power and the device input terminal impedance. It can also be used to search for the optimum device operating conditions. Also, it is useful in examining the oscillator stability.

The model was tested to verify its accuracy by comparing the calculated results to measured data. Different gate tuning circuit impedance as well as RF voltages were given. The source load impedances and output power were calculated. At 7 GHz, a gate impedance of $Z_{L1} = 1.5 + j62.5 \Omega$ was used. The calculated source load impedances and output power at different RF voltages were obtained by using the model and are plotted in Fig. 4.9. For each case the calculated power and impedance were very close to the measured values. The maximum measured power for the given gate tuning circuit was 203 mW while the calculated power was 212 mW.

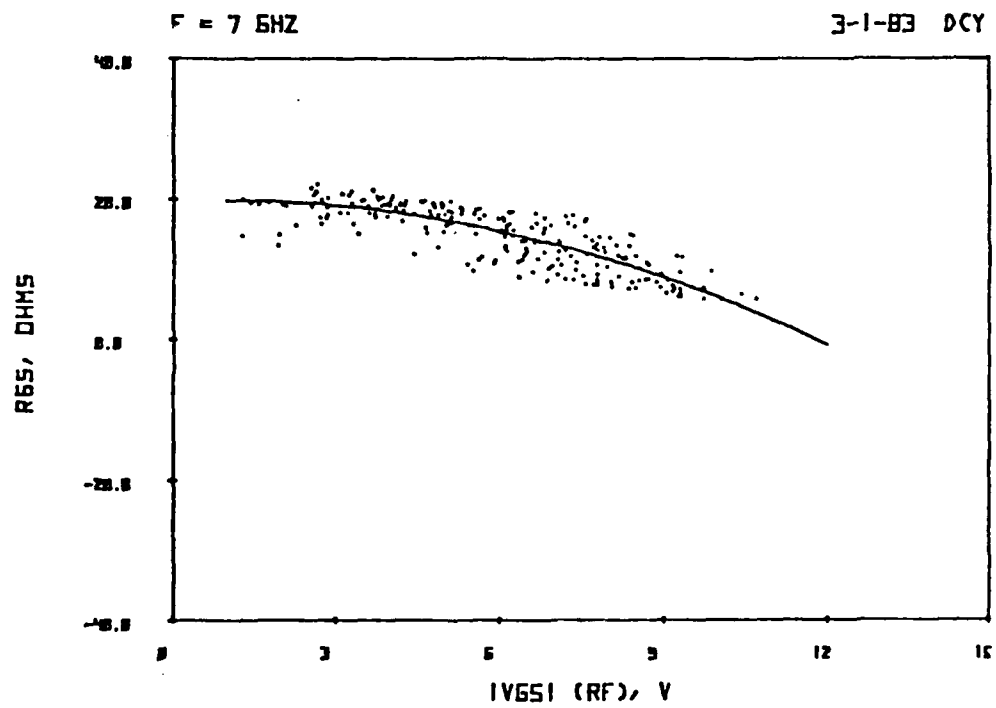


Fig. 4.5 Curve Fitted R_{gs} vs. RF Voltage $|V_{gs}|$ at 7 GHz.

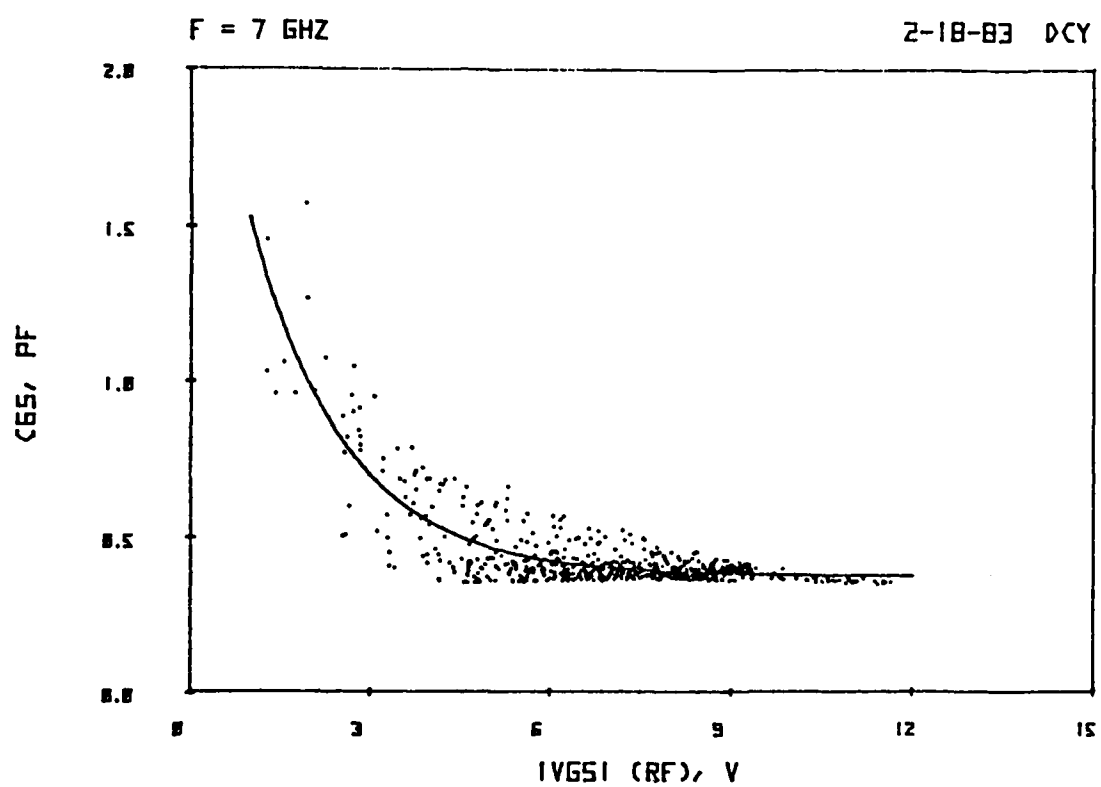


Fig. 4.8 Curve Fitted C_{gs} vs. RF Voltage $|V_{gs}|$ at 7 GHz.

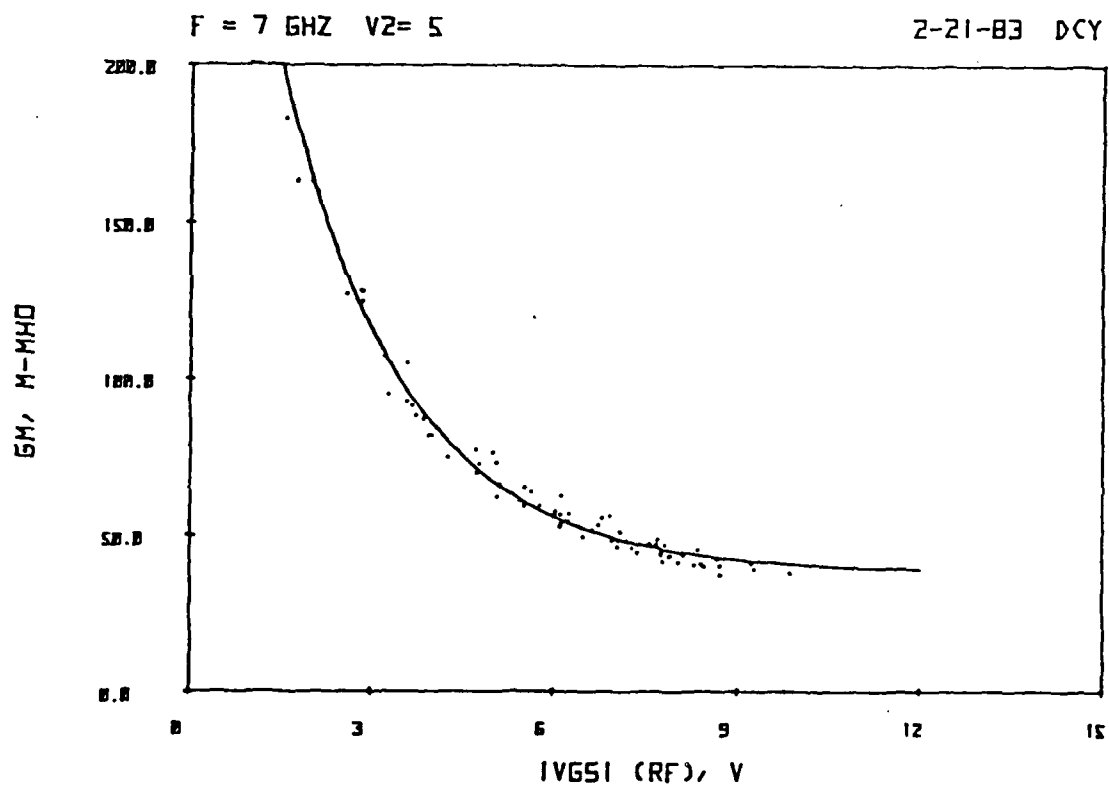


Fig. 4.7 Curve Fitted g_m vs. RF Voltage $|V_{gs}|$ with $|V_2| = 5$ V at 7 GHz.

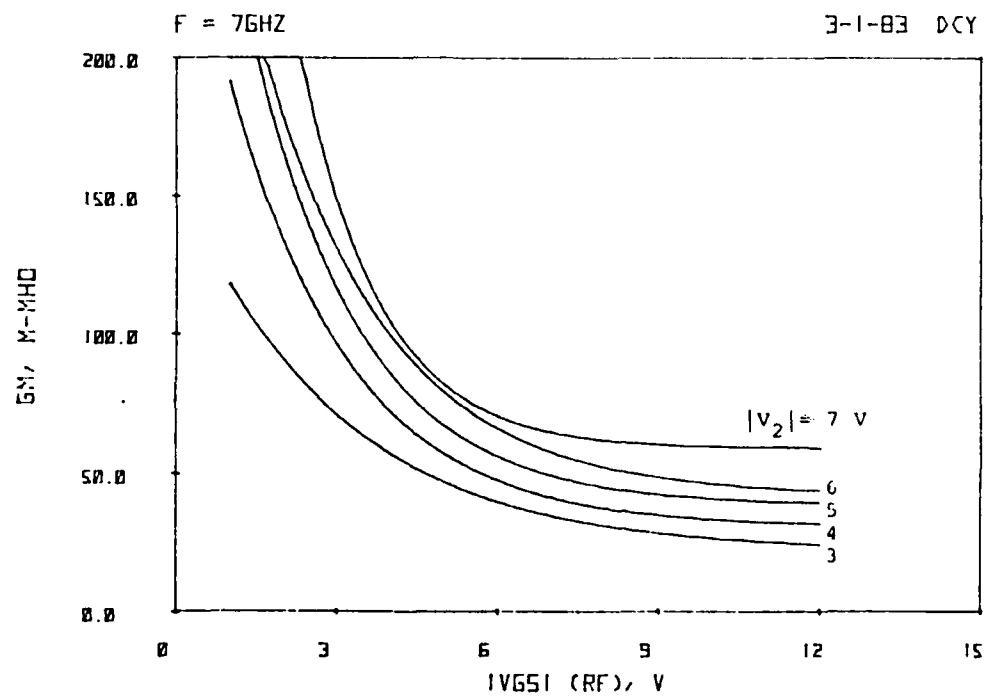


Fig. 4.8 Curve Fitted g_m vs. RF Voltage $|V_{gs}|$ at 7 GHz.

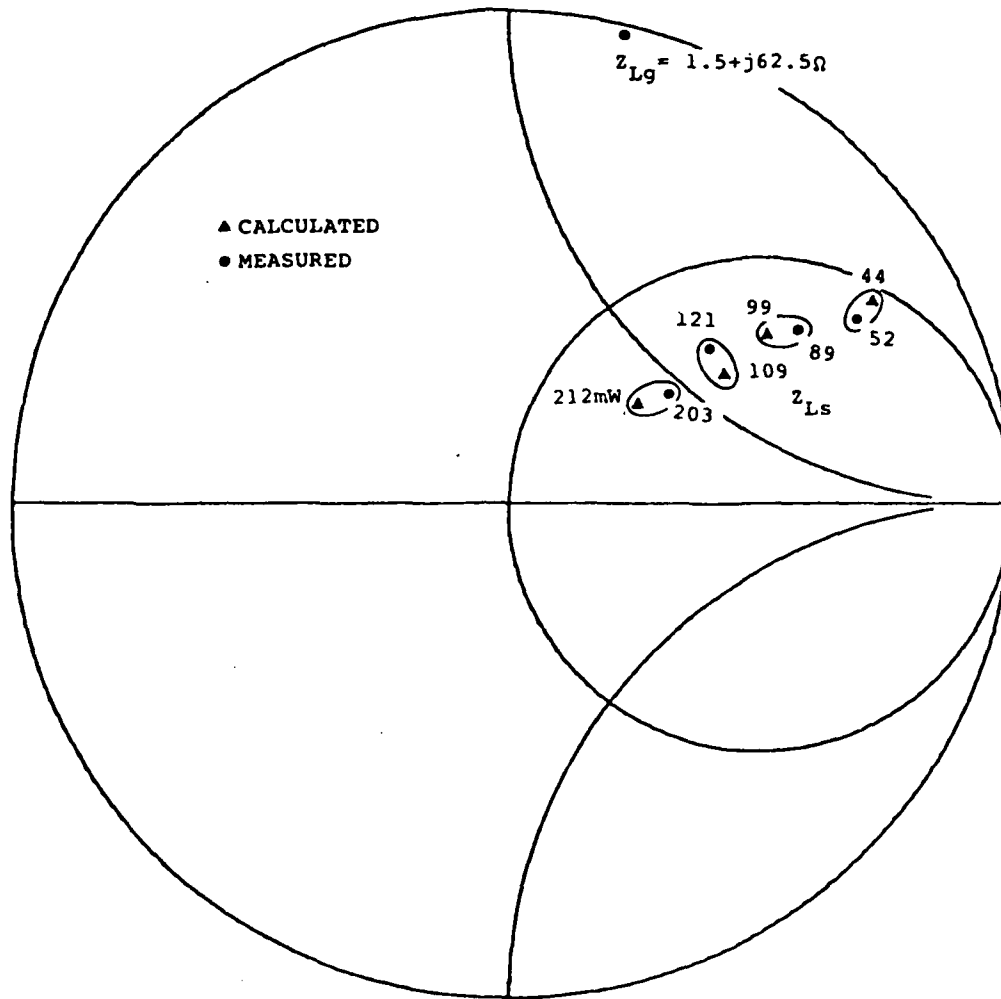


Fig. 4.9 Calculated vs. Measured Source Impedance and Output Power at 7 GHz.

At 8 GHz, $Z_{L1} = 5 + j45 \Omega$ was chosen. Four source load impedances and their corresponding power levels were calculated as shown in Fig. 4.10. The maximum output power measured in this case was 38 mW, the same as that calculated. For 9 GHz with $Z_{L1} = 1 + j43 \Omega$, the optimum output power at the source was measured at 50 mW while 55 mW was calculated. The results at 9 GHz is as shown in Fig. 4.11. A summary of these measured and calculated results are tabulated in Table 4.3.

4.3. Summary

A large-signal MESFET equivalent circuit model was developed. The nonlinear element values were calculated and curve fitted as functions of terminal RF voltages. Device performances calculated by using this model were in agreement with that of the measurement results.

This model was derived from a large amount of measured data to investigate the behavior of the various nonlinear elements. The results show that these element values are well behaved with RF voltage and can be fit to smooth function with low error. In principle, a smaller amount of data could be used to determine the element values for this large-signal model as long as these measurements cover the entire device operating range.

The large-signal MESFET equivalent circuit model presented in this chapter provides a simple way to investigate the large-signal performance of the device and to establish approximate circuit conditions. The model offers accurate prediction of device behavior because it is based on actual measured results. Although this model has limitations as described, it can be a very useful tool for designing large-signal MESFET circuits. Once such a model has been established for a given class of device, it can then be used as a design tool without having to perform additional characterization measurements.

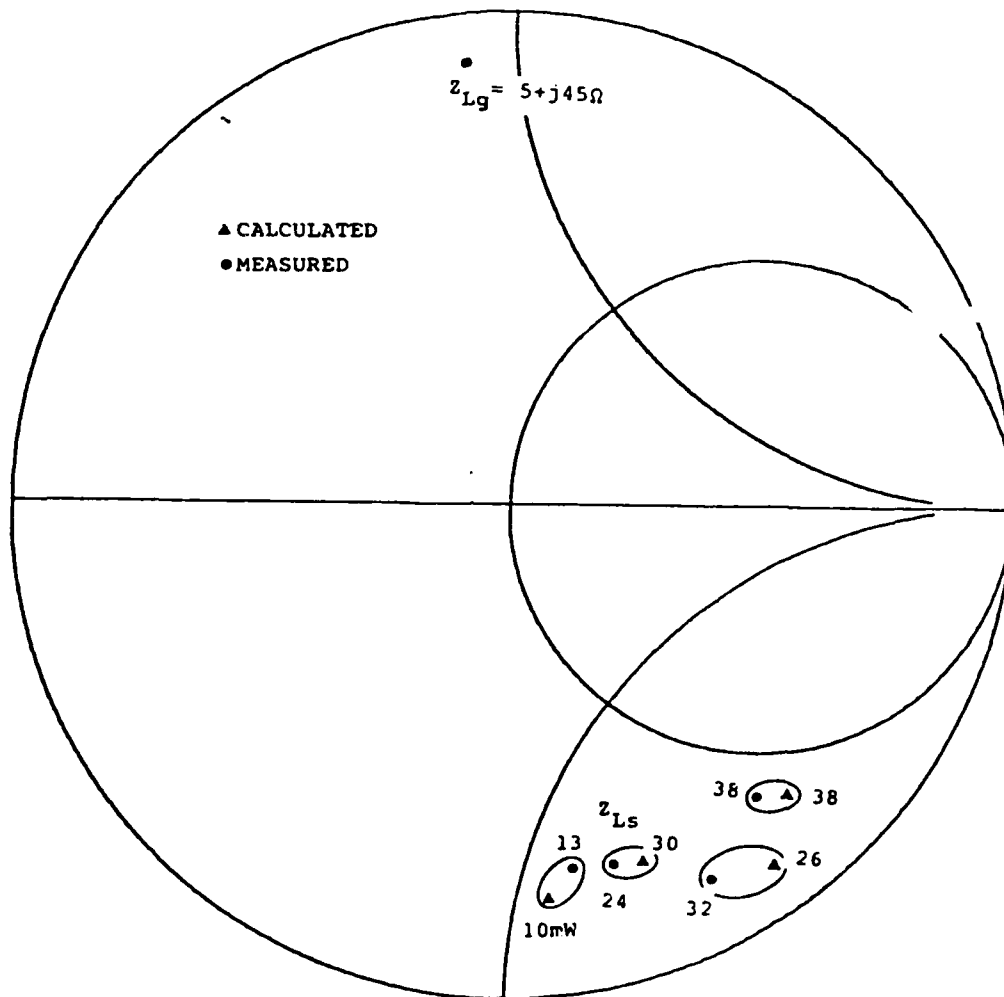


Fig. 4.10 Calculated vs. Measured Source Impedance and Output Power at 8 GHz.

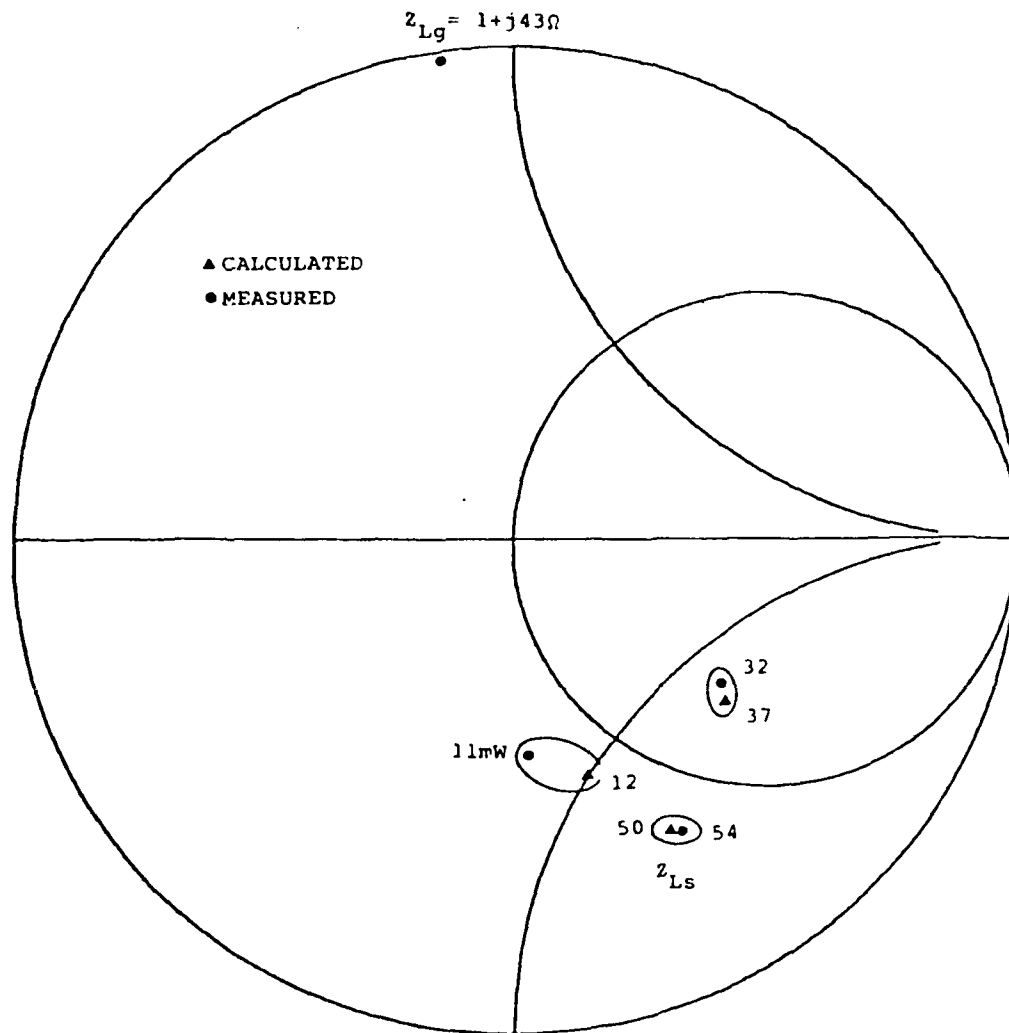


Fig. 4.11 Calculated vs. Measured Source Impedance and Output Power at 9 GHz.

TABLE 4.3

Calculated and Measured Source Impedances and Output Power

FREQUENCY = 7 GHz

ZLg = 1.5 + j62.5 Ohms

MEASURED

Re ZS	Im ZS	P (mW)
-----	-----	-----
-80.67	-68.54	121.00
-81.97	-42.80	203.00
-90.15	-116.15	89.00
-80.87	-160.70	52.00

CALCULATED

Re ZD	Im ZD	P (mW)
-----	-----	-----
-94.04	-66.40	109.00
-74.57	-34.21	212.00
-87.21	-97.21	99.00
-62.46	-168.50	44.00

FREQUENCY = 8 GHz

ZLg = 5 + j45 Ohms

MEASURED

Re ZS	Im ZS	P (mW)
-----	-----	-----
-17.21	57.07	10.00
-33.87	98.50	38.00
-18.80	63.47	24.00
-14.26	82.15	32.00

CALCULATED

Re ZD	Im ZD	P (mW)
-----	-----	-----
-11.94	54.22	13.00
-32.62	109.40	38.00
-19.52	68.80	30.00
-12.02	98.10	26.00

FREQUENCY = 9 GHz

ZLg = 1 + j43 Ohms

MEASURED

Re ZS	Im ZS	P (mW)
-----	-----	-----
-35.52	38.43	11.00
-85.63	67.10	32.00
-33.97	73.80	50.00

CALCULATED

Re ZD	Im ZD	P (mW)
-----	-----	-----
-39.00	50.10	12.00
-79.59	72.80	36.00
-34.10	71.30	55.00

CHAPTER V

CONCLUSIONS

5.1. Summary and Conclusions

The major contributions of this research include development of a large-signal characterization procedure for two-port nonlinear active networks, analysis of the large-signal properties of MESFETs, and establishment of a large-signal MESFET equivalent circuit model. The large-signal behavior of nonlinear two-port networks are always of great interest to circuit designers. A new approach was developed and reported in this dissertation, which has overcome several difficulties encountered by earlier methods.

In Chapter II, the problem of describing a nonlinear active two-port network was discussed. A set of parameters which uniquely describe the nonlinear two-port network was identified. A large-signal characterization technique for the nonlinear two-port networks was established. The measurement system consisted of two network analyzers, a desk-top calculator, and other necessary components for monitoring and leveling the test signal power and gathering test results. Computer programs were developed for controlling the measurement process and acquiring the measurement data. For implementing the characterization process, the GaAs MESFET was measured for its large-signal characteristics. The design and characterization of the MESFET test fixture were also presented.

The MESFETs were measured in both common drain and common source configurations. It was found that in the common drain configuration both the gate

and the source ports were active over a wide frequency range. This configuration facilitates the design of independent tuning and output circuits for oscillators. It is also ideal for wideband VCO applications because feedback circuits are not necessary. Therefore, the measurements concentrated on large-signal properties of common drain MESFETs.

Device characterization was made from 7 to 13 GHz at 1-GHz intervals. The measurement results were analyzed for common drain oscillator applications in Chapter III. Relationships between the available power and the load impedances at both ports were studied. The device performance as a VCO was also investigated. A single-frequency common drain MESFET oscillator was built to verify the measurement results.

A large-signal equivalent circuit model of the MESFET was presented in Chapter IV. It was found that the gate to source resistance and capacitance and the transconductance were the dominant terms contributing to the nonlinear behavior of the device. The values of these three elements vs. the terminal RF voltages were solved by using the measurement results, and smooth curves were fitted to the data. The device performance calculated by using the model was shown and compared to the measured data.

In conclusion, the properties of nonlinear active two-port networks were successfully characterized by the measurement technique outlined in this report. The network terminal conditions must be varied during the course of the measurement to characterize the network under various excitation levels. To achieve such measurement conditions, it is necessary to use two coherent test signals.

The measurement results for a common drain MESFET show clearly the single-frequency nonlinearity of the device. With the presented characterization technique, the device performance over the entire operating range was revealed,

technique, the device performance over the entire operating range was revealed, providing information which cannot be obtained by any other available measurement method. The optimum design of the nonlinear two-port network then can be achieved by using this data. Once accurate measurement data are obtained, the device model can be established easily and used as a tool for design and analysis of the two-port network.

5.2. Suggestions for Further Study

It is hoped that the research project presented here will pave the way for further study in several areas. One example is to use this large-signal method to characterize the harmonic properties of nonlinear two-port networks, such as harmonic frequency combiners and frequency multipliers. These networks usually operate at the fundamental frequency at one port and at a harmonic frequency at the other. It is extremely difficult to measure the network with fundamental and harmonic frequencies existing at the same time. With this method one test signal frequency can be the multiple of the other, thus providing a solution to this problem.

With the availability of new high power desk-top computers, it is possible to develop a measurement system to search for optimum operating conditions automatically. This can be achieved by incorporating an optimizing program into the measurement program. By evaluating the measured results, the optimizing program can predict the desired test signal power levels and phase setting for the next measurement. This process is then repeated until the optimum operating condition is reached. This will be a very powerful tool to determine the optimum operating point of almost any nonlinear two-port network.

All the large-signal MESFET models available are either derived from the device physics or from the measurement results. Since these previous large-

signal characterizations were made under restrictive conditions, models established by using these results were only of limited application. With the new two-port characterization technique presented in this report, a more complete description of the large-signal device properties can be obtained. It is hoped that a MESFET model using both the device physics and the measurement results could be developed. By closely relating the device physical parameters to the device performance, it will not only provide better understanding of the device but also reduce the amount of RF measurements. Furthermore, accurate large-signal characterization will ensure the model accuracy over the entire device operating range.

APPENDIX A

ADDITIONAL EXPERIMENTAL RESULTS AT 8 TO 11 GHz

The measured data of a 250-mW rated MESFET were analyzed for performance as a common drain oscillator as described in Chapter III. The gate and source load impedance pairs and their corresponding source output power are presented in this appendix. At 8 GHz, the measured device performance for three different gate loss levels of 0.5, 7.5, and 10 Ω are shown in Figs. A.1 through A.3, respectively. By combining the maximum output power curves at all different gate loss levels, a graph as shown in Fig. A.4 was obtained.

Measurement results at 9 GHz were sorted and curves for 0.5-, 3-, 5-, and 10- Ω gate losses are shown in Figs. A.5 through A.8. Figure A.9 shows a total picture of the device performance at 9 GHz. For 10 GHz, the load impedance pairs and their corresponding source output power were plotted as shown in Figs. A.10 through A.14. The same curves for data obtained at 11 GHz are shown in Figs. A.14 through A.16.

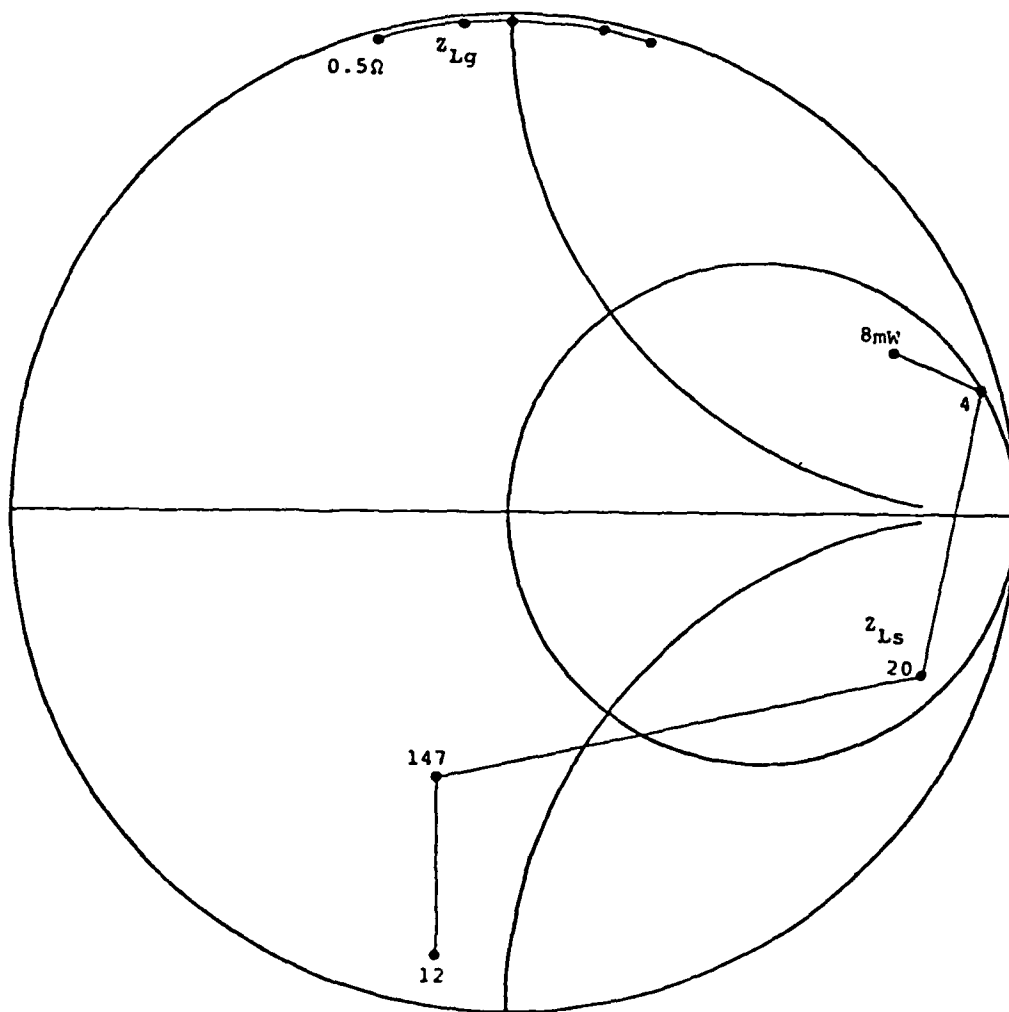


Fig. A.1 Gate and Source Loading Conditions for a Constant Gate Loss of 0.5Ω at 8 GHz.

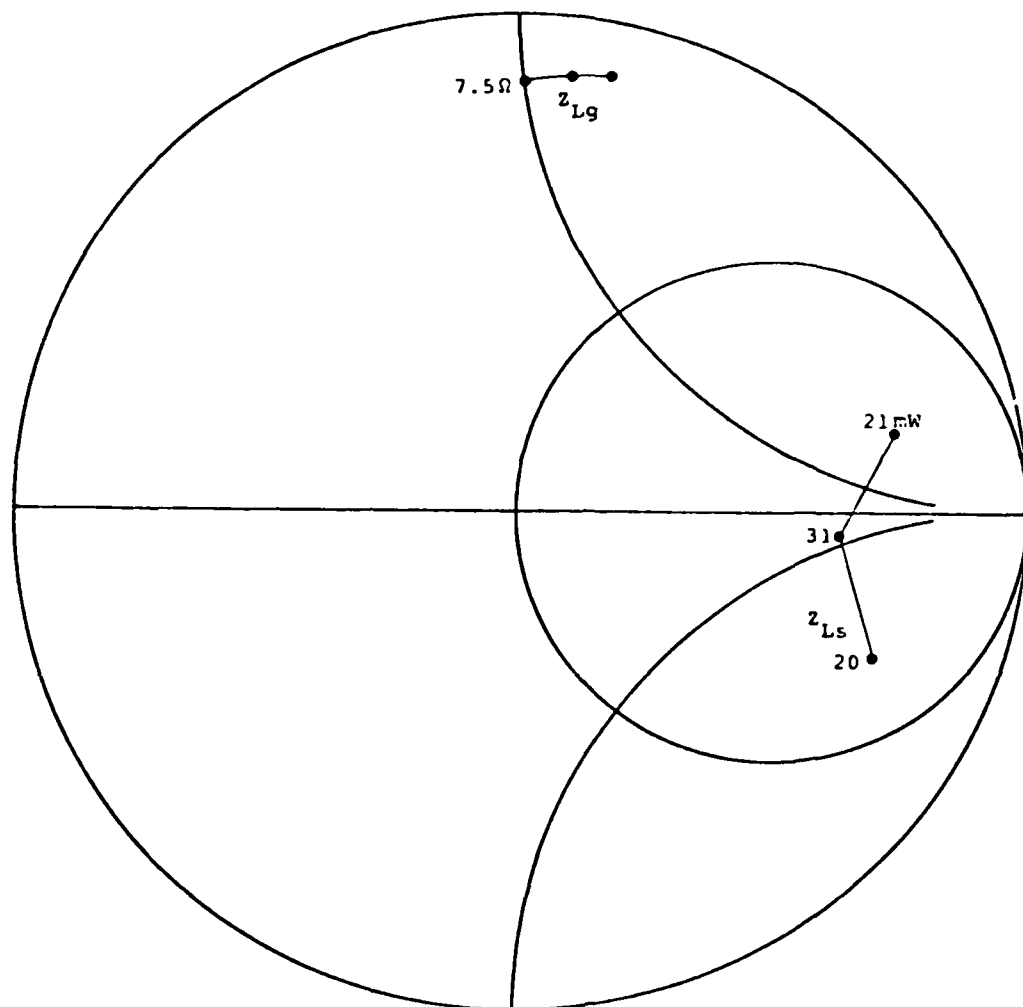


Fig. A.2 Gate and Source Loading Conditions for a Constant Gate Loss of 7.5Ω at 8 GHz.

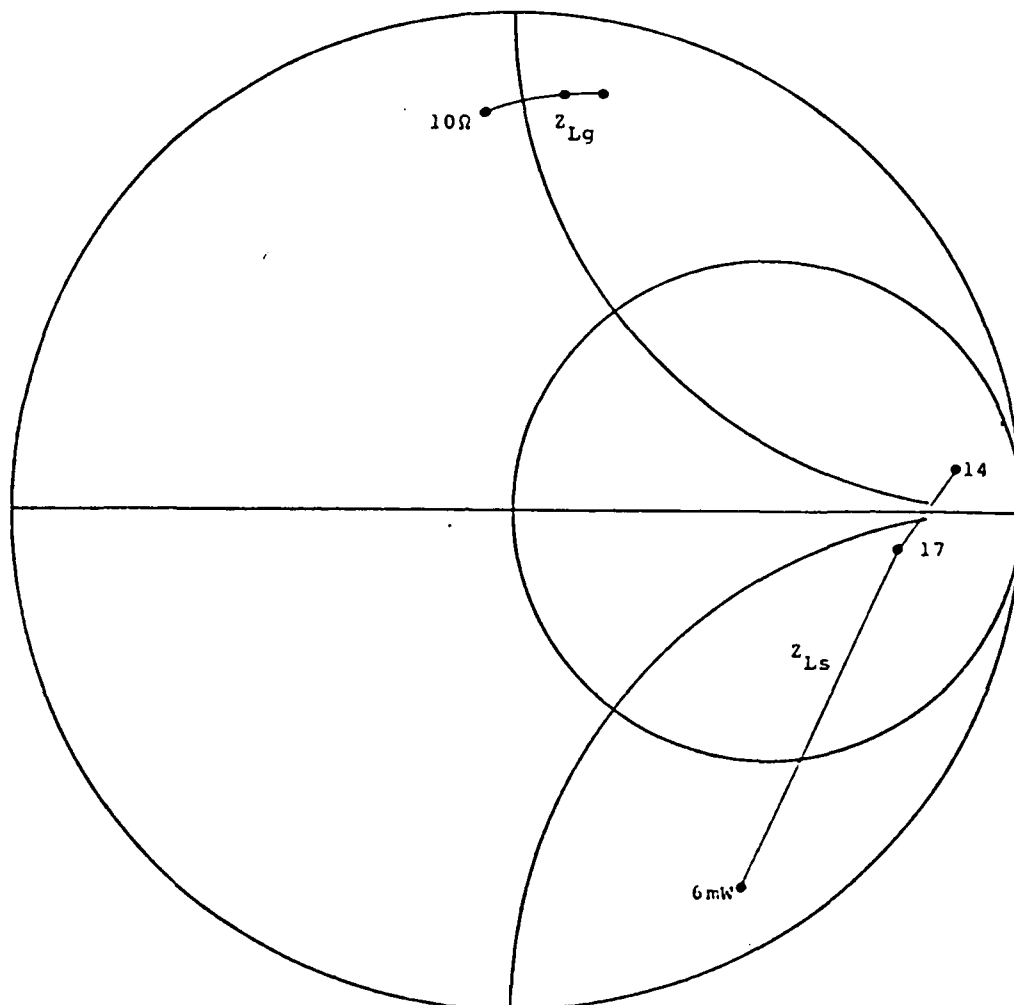


Fig. A.3 Gate and Source Loading Conditions for a Constant Gate Loss of $10\ \Omega$ at 8 GHz.

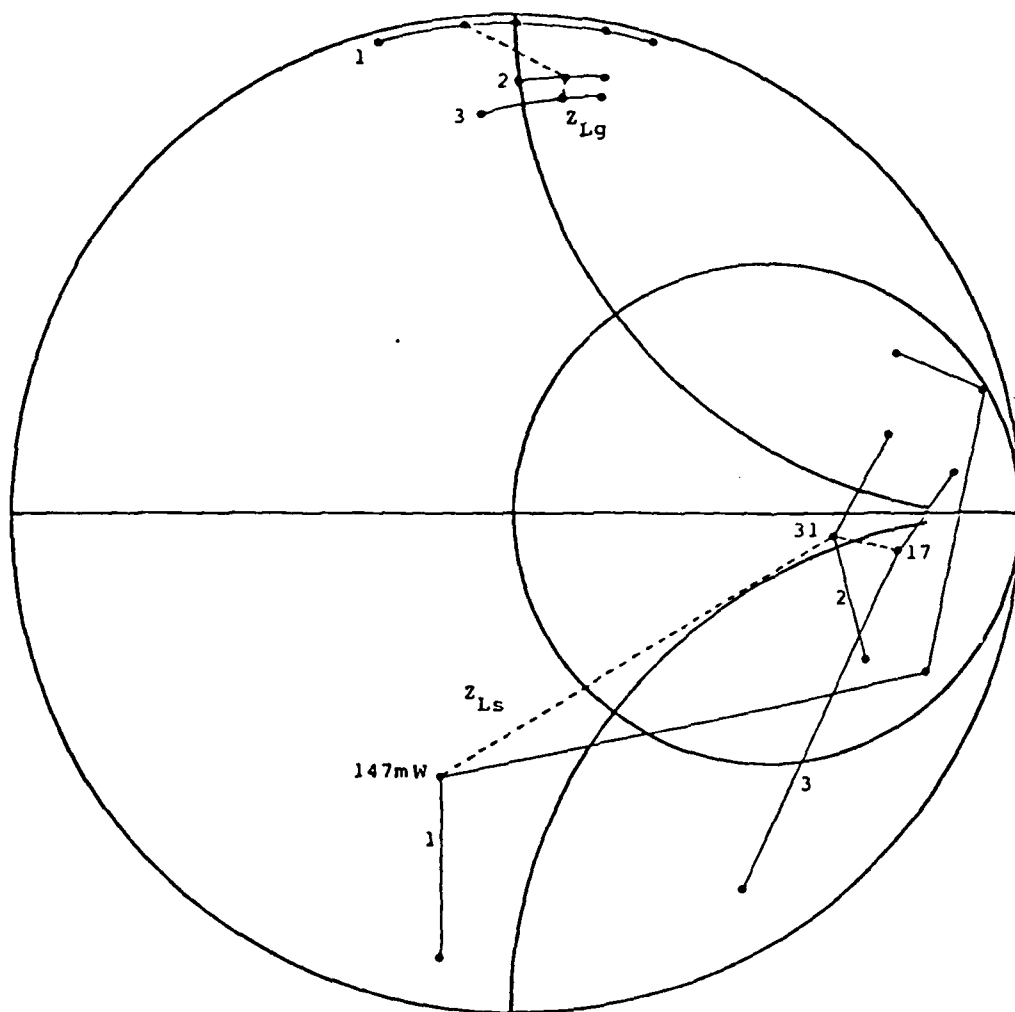


Fig. A.4 Gate and Source Loading Conditions vs. Output Power at 8 GHz.

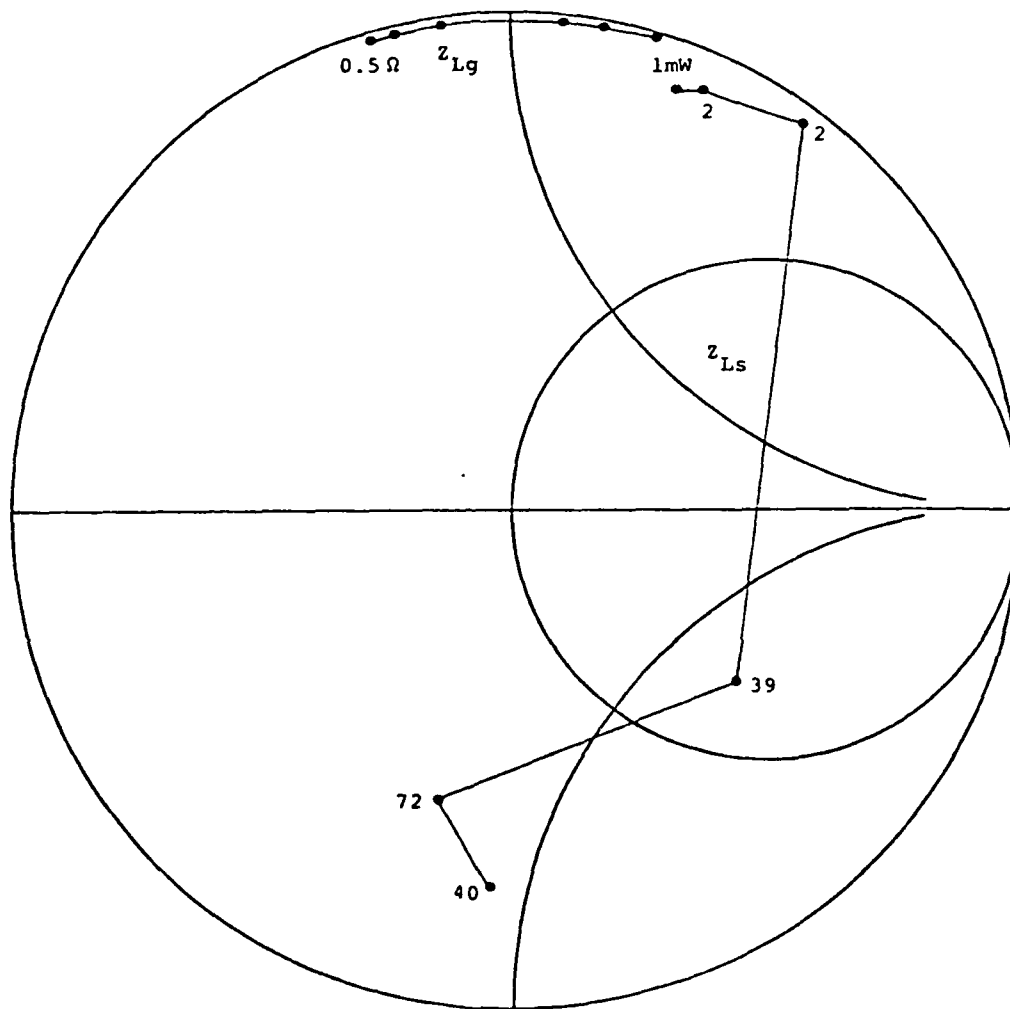


Fig. A.5 Gate and Source Loading Conditions for a Constant Gate Loss of 0.5Ω at 9 GHz.

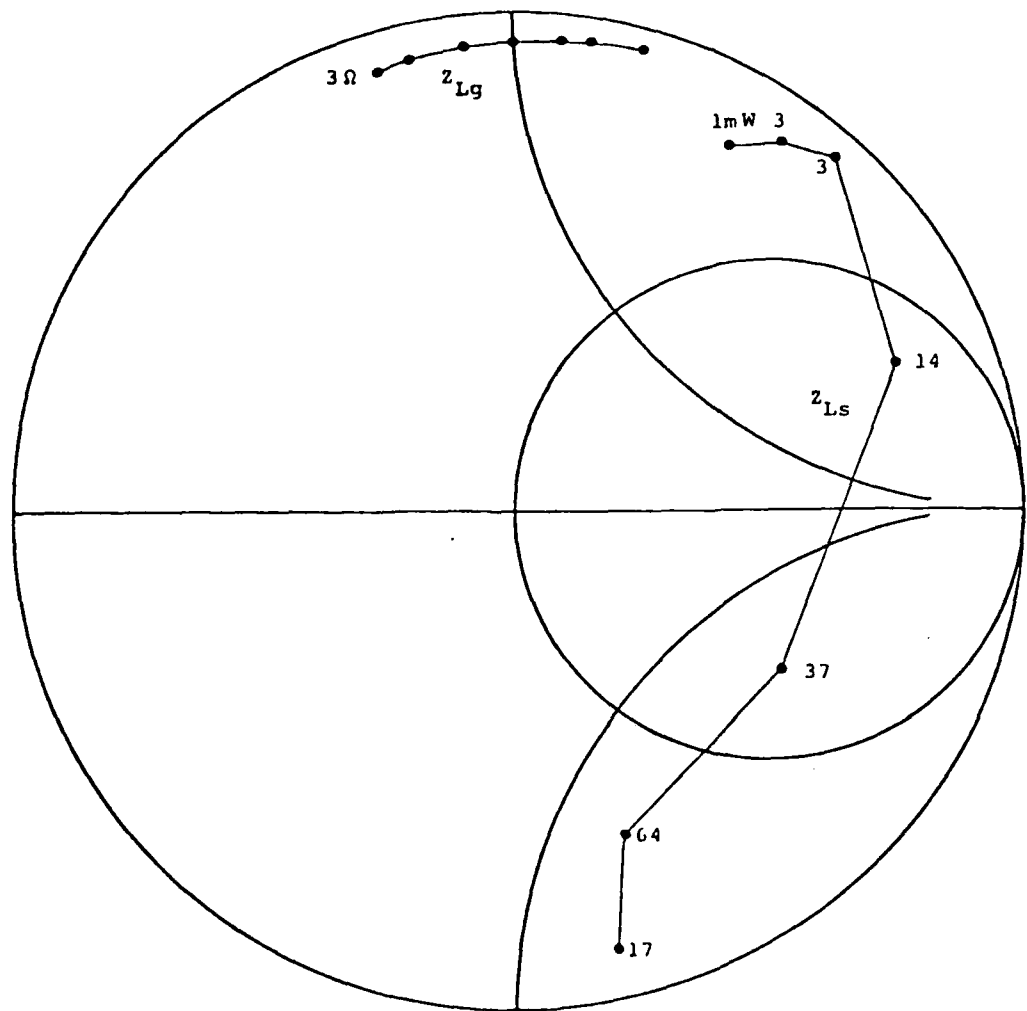


Fig. A.6 Gate and Source Loading Conditions for a Constant Gate Loss of 3Ω at 9 GHz.

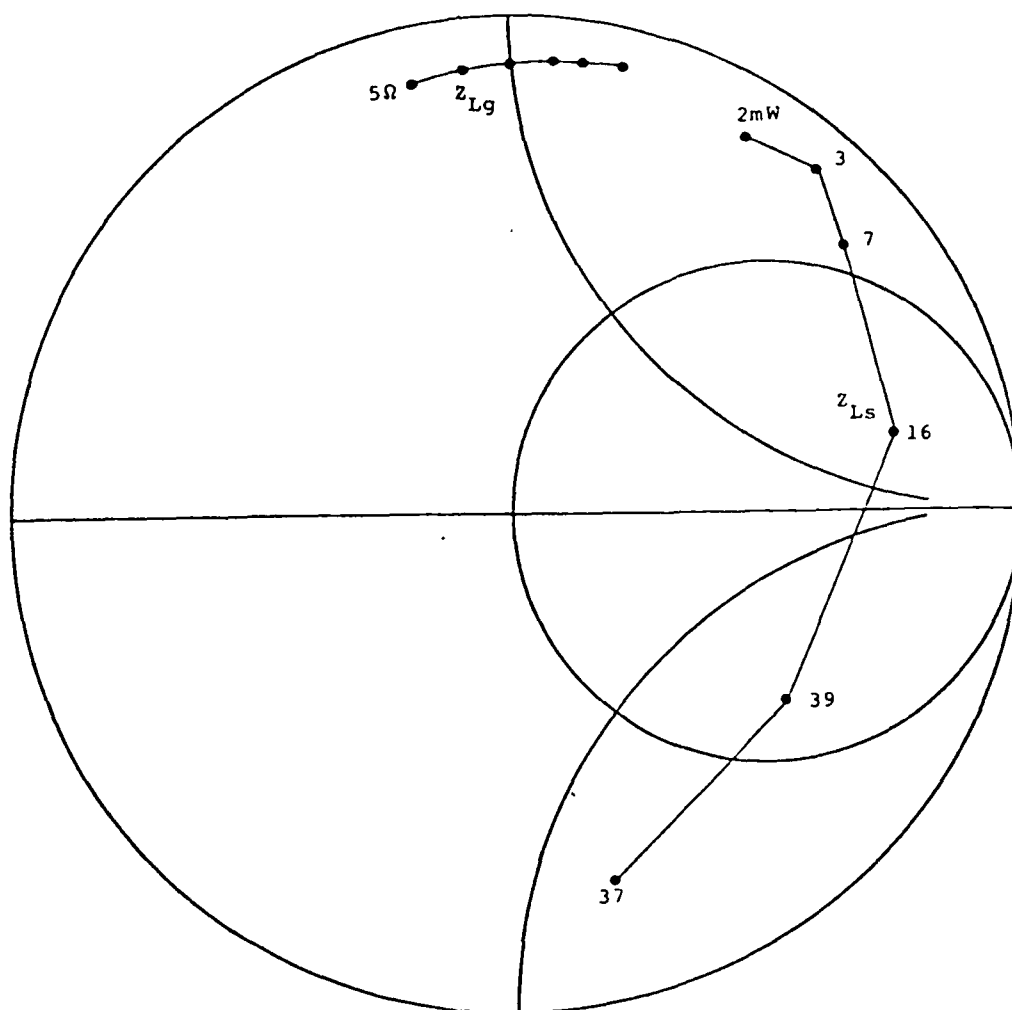


Fig. A.7 Gate and Source Loading Conditions for a Constant Gate Loss of 5Ω at 9 GHz.

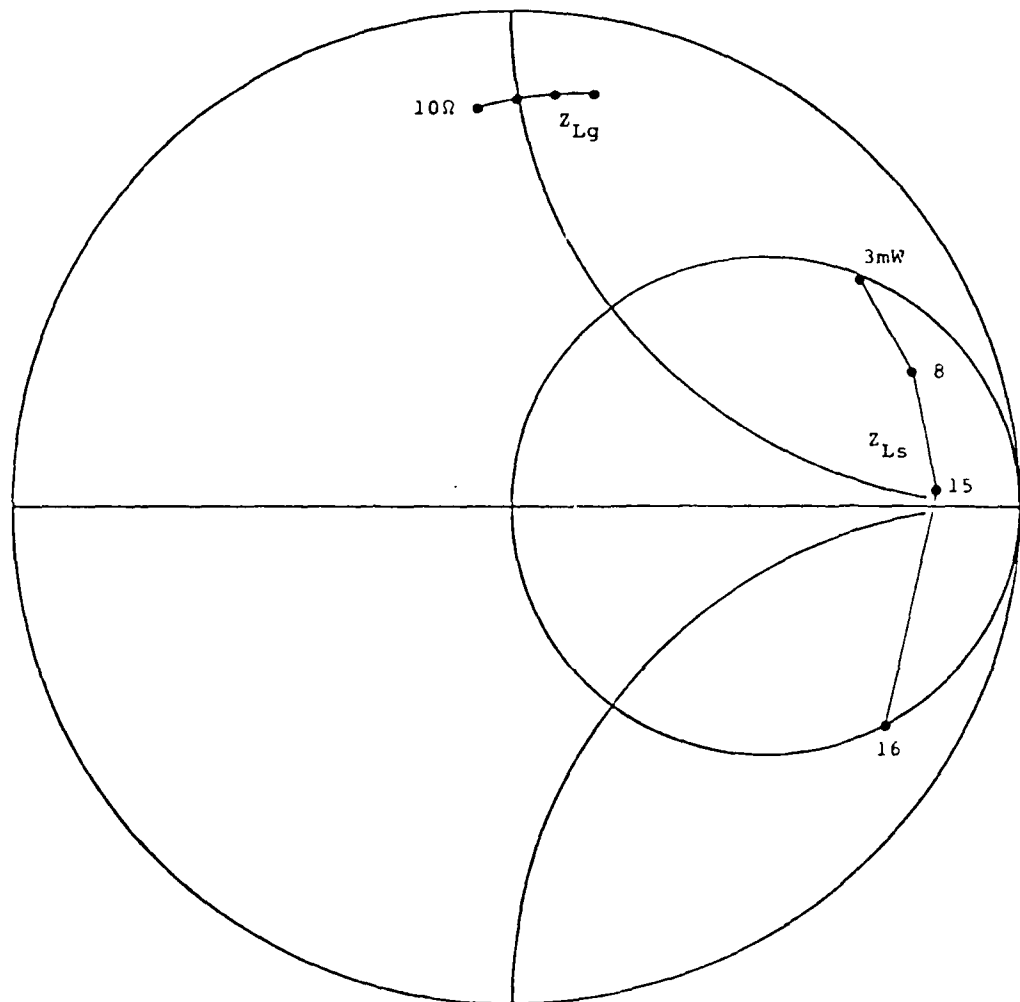


Fig. A.8 Gate and Source Loading Conditions for a Constant Gate Loss of $10\ \Omega$ at 9 GHz.

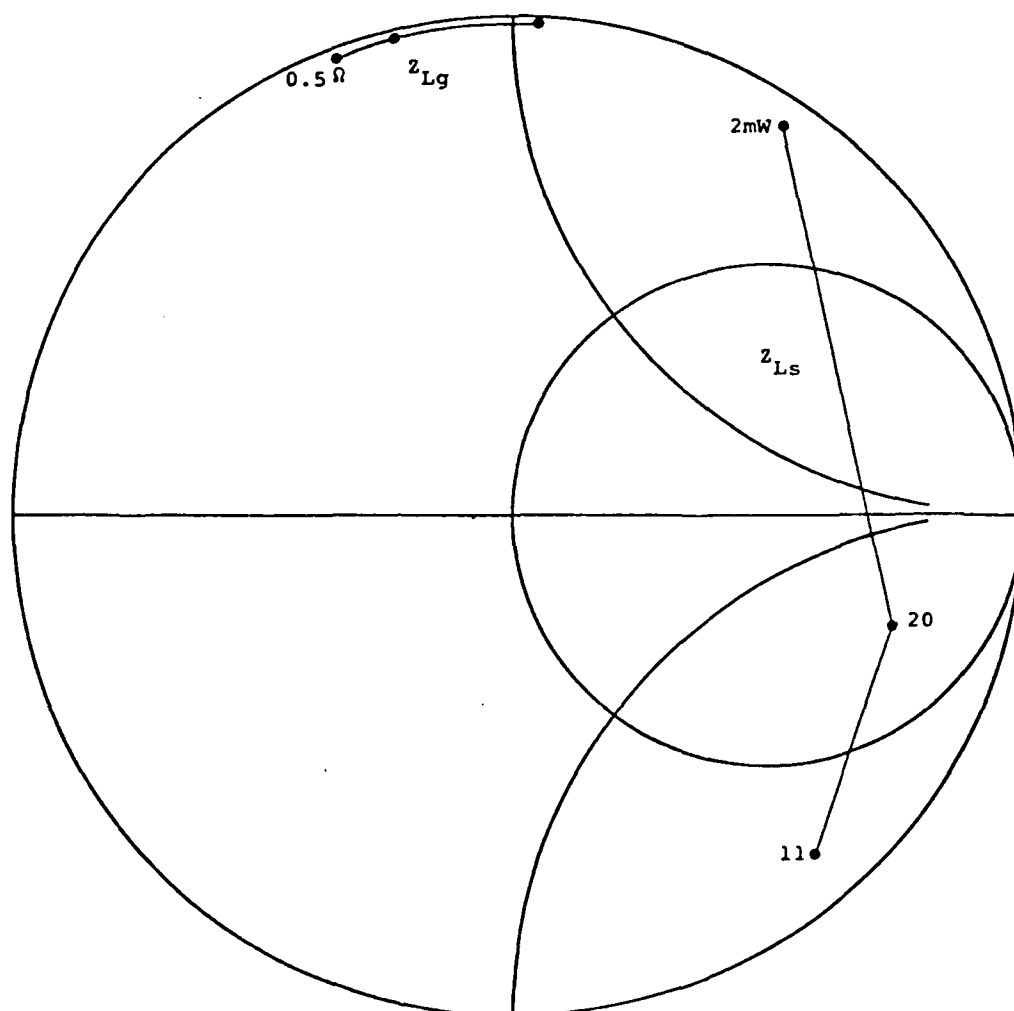


Fig. A.10 Gate and Source Loading Conditions for a Constant Gate Loss of 0.5Ω at 10 GHz.

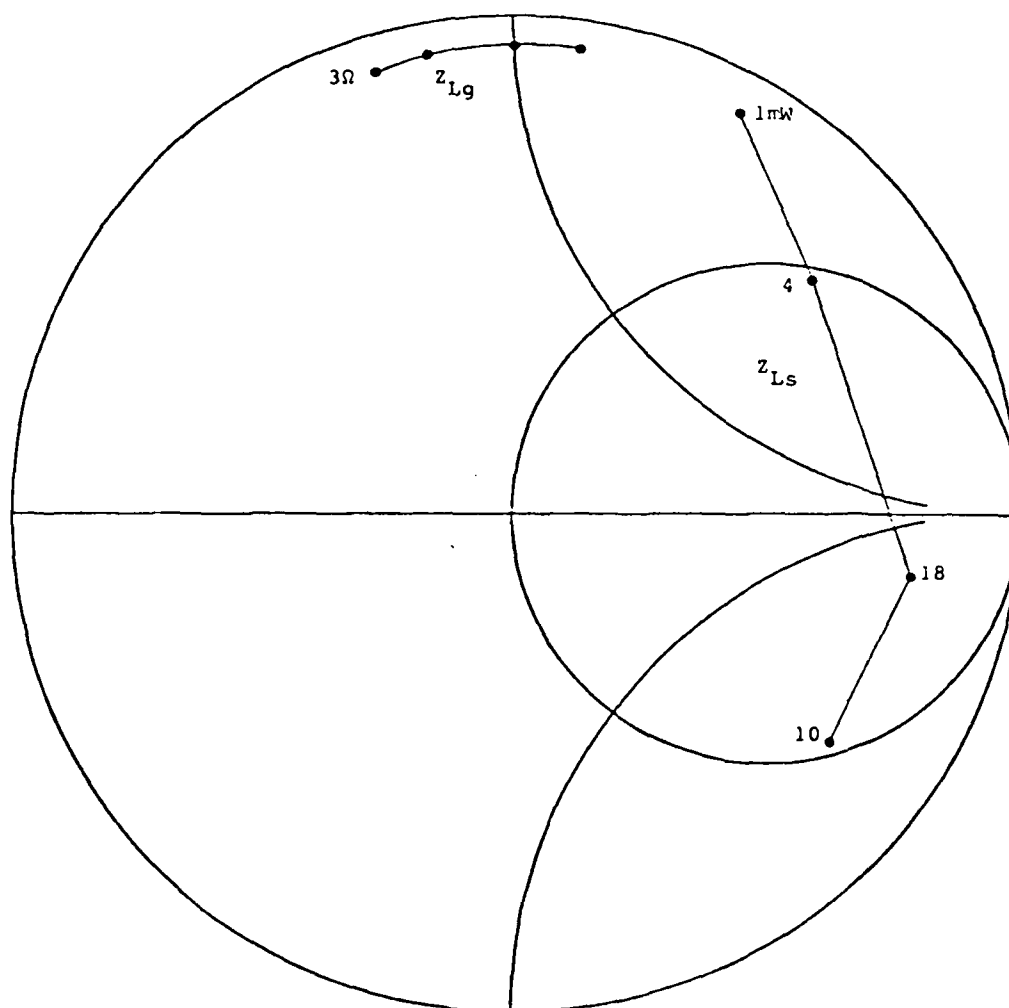


Fig. A.11 Gate and Source Loading Conditions for a Constant Gate Loss of $3\ \Omega$ at 10 GHz.

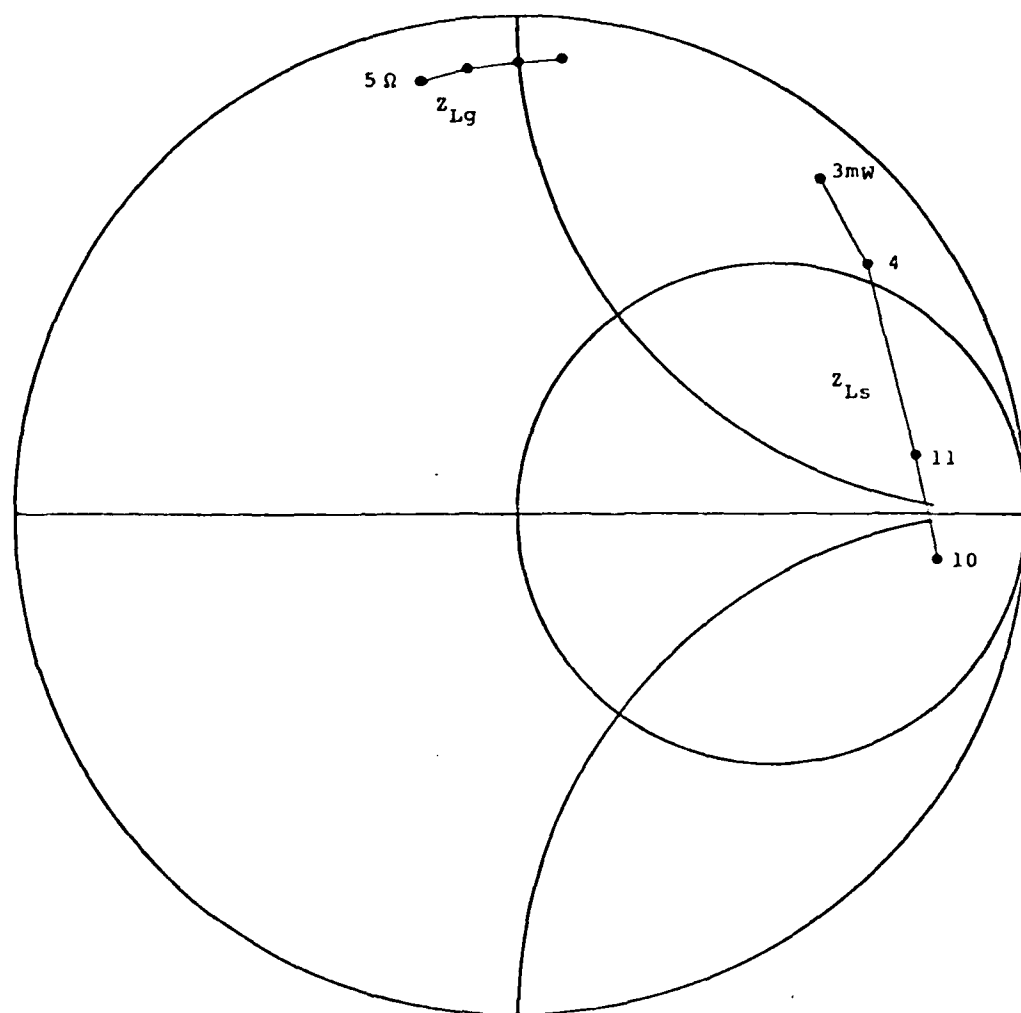


Fig. A.12 Gate and Source Loading Conditions for a Constant Gate Loss of 5Ω at 10 GHz.

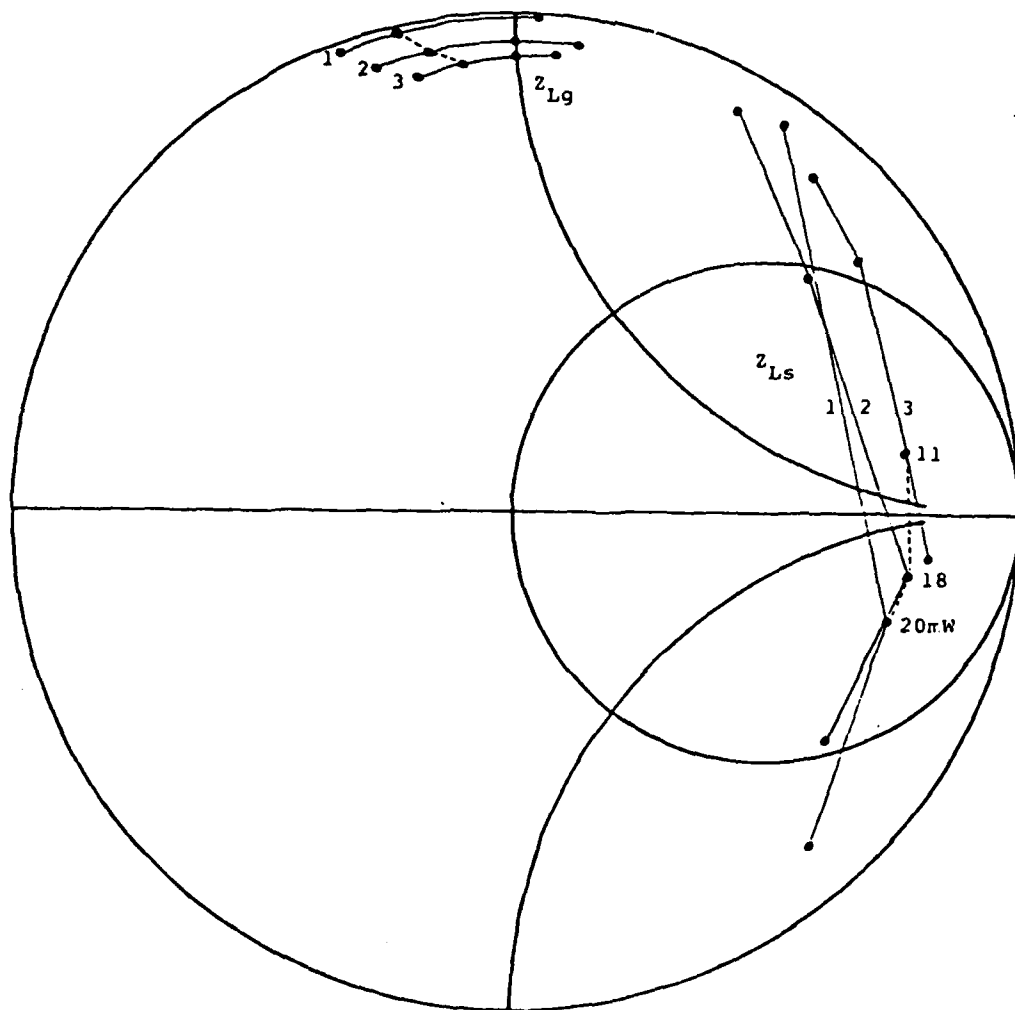


Fig. A.13 Gate and Source Loading Conditions vs. Output Power at 10 GHz.

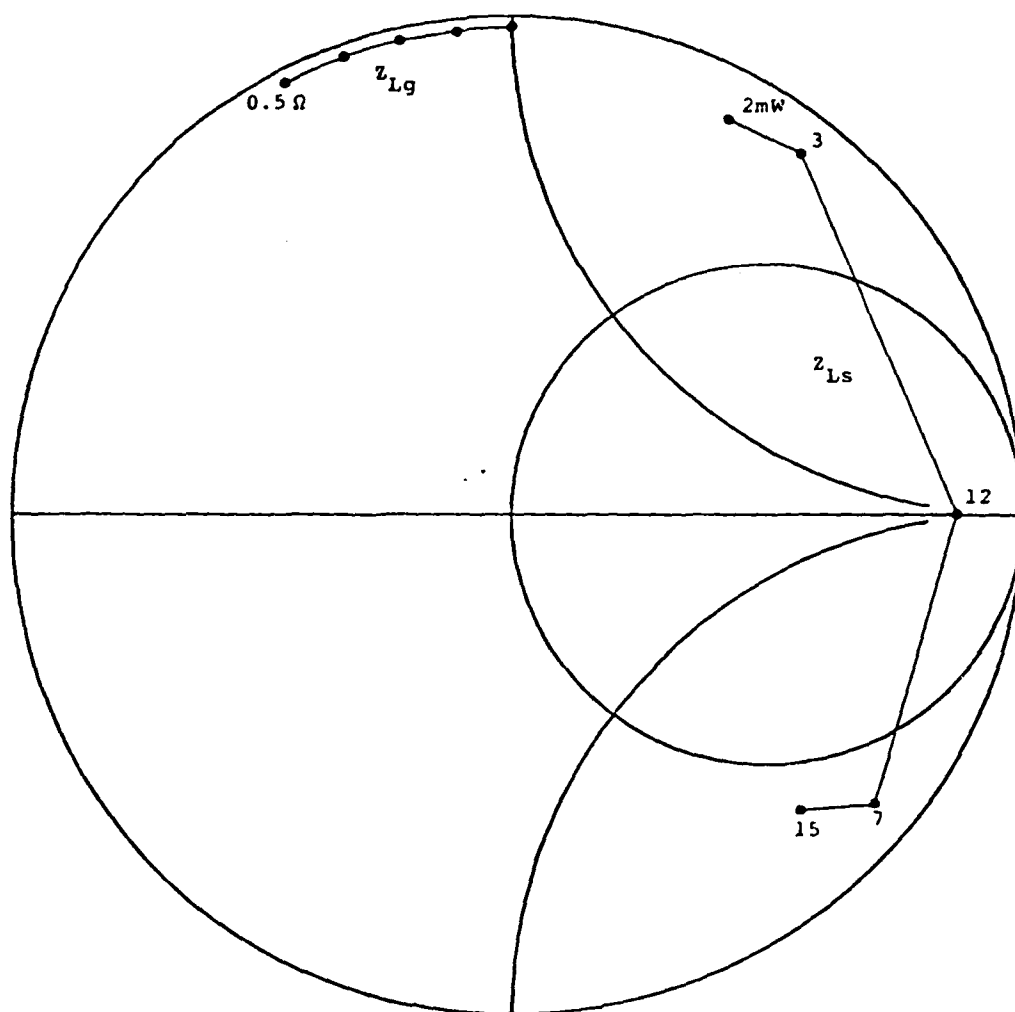


Fig. A.14 Gate and Source Loading Conditions for a Constant Gate Loss of 0.5Ω at 11 GHz.

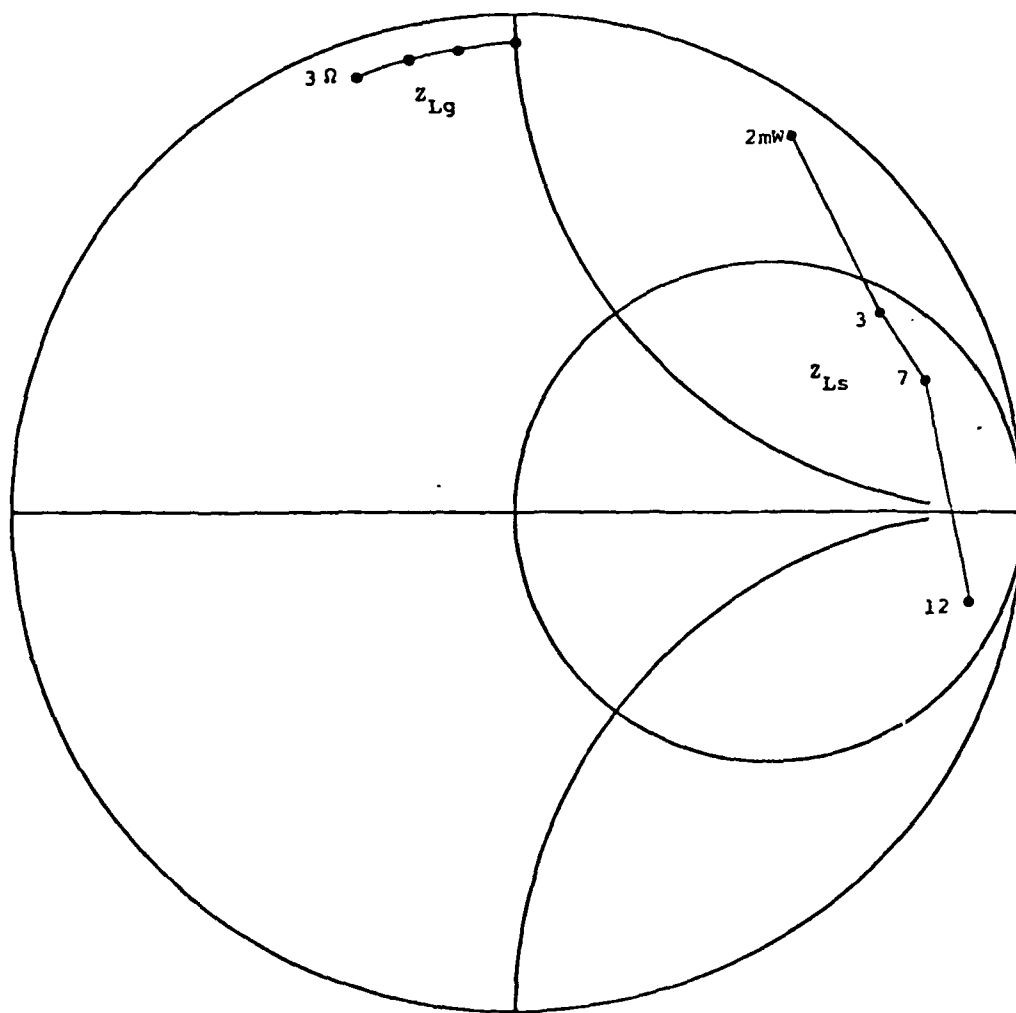


Fig. A.15 Gate and Source Loading Conditions for a Constant Gate Loss of $3\ \Omega$ at 11 GHz.

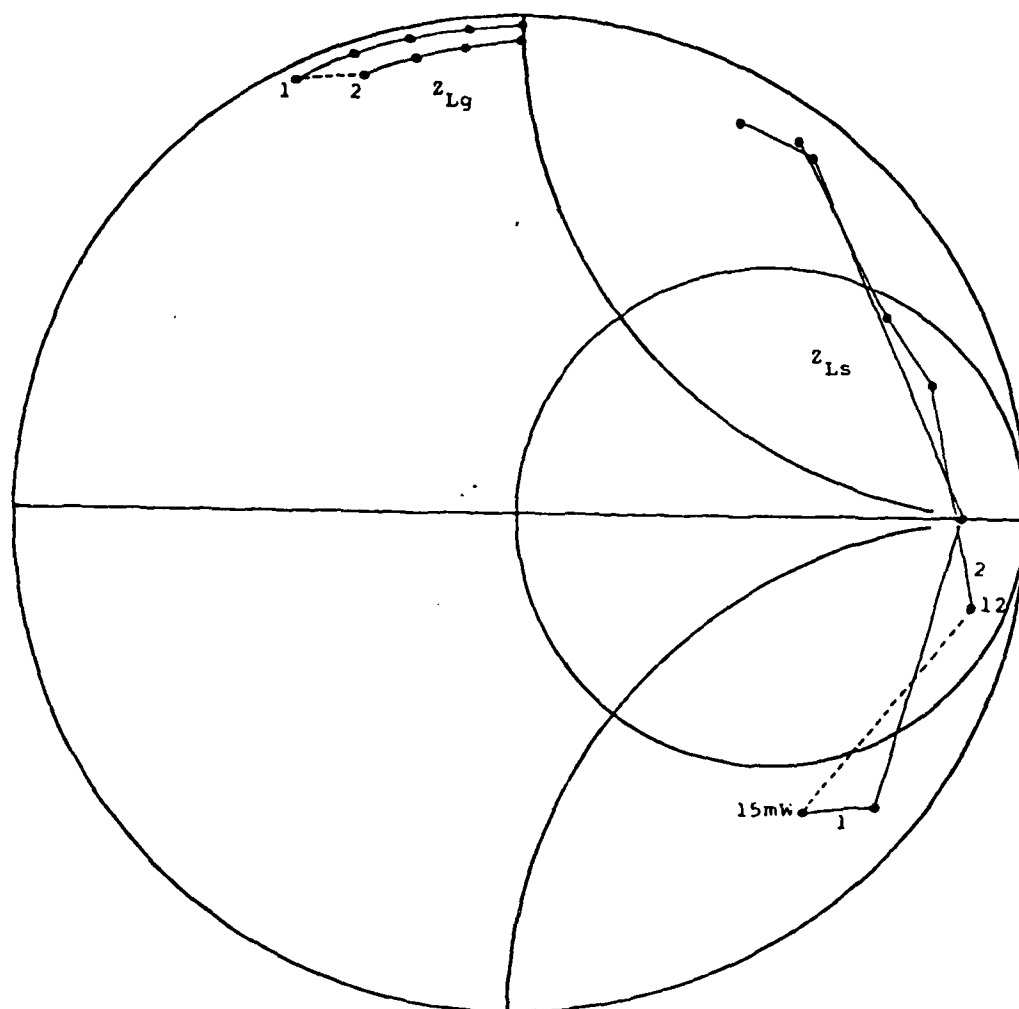


Fig. A.16 Gate and Source Loading Conditions vs. Output Power at 11 GHz.

APPENDIX B**MESFET MODEL ELEMENT VALUES AT 8 AND 9 GHz**

The MESFET equivalent circuit model element values were solved at three different frequencies: 7, 8, and 9 GHz. The values for each nonlinear element, i.e., the gate to source resistance R_{gs} , capacitance C_{gs} , and transconductance g_m were curve fitted as functions of the magnitude of the gate to source RF voltage $|V_{gs}|$ as described in Chapter IV. Results for the element values at 8 and 9 GHz are presented in this appendix. Figures B.1 and B.2 show the values of R_{gs} and C_{gs} as functions of $|V_{gs}|$, respectively, while g_m is shown in Fig. B.3. The element values at 9 GHz are shown in Figs. B.4 through B.6.

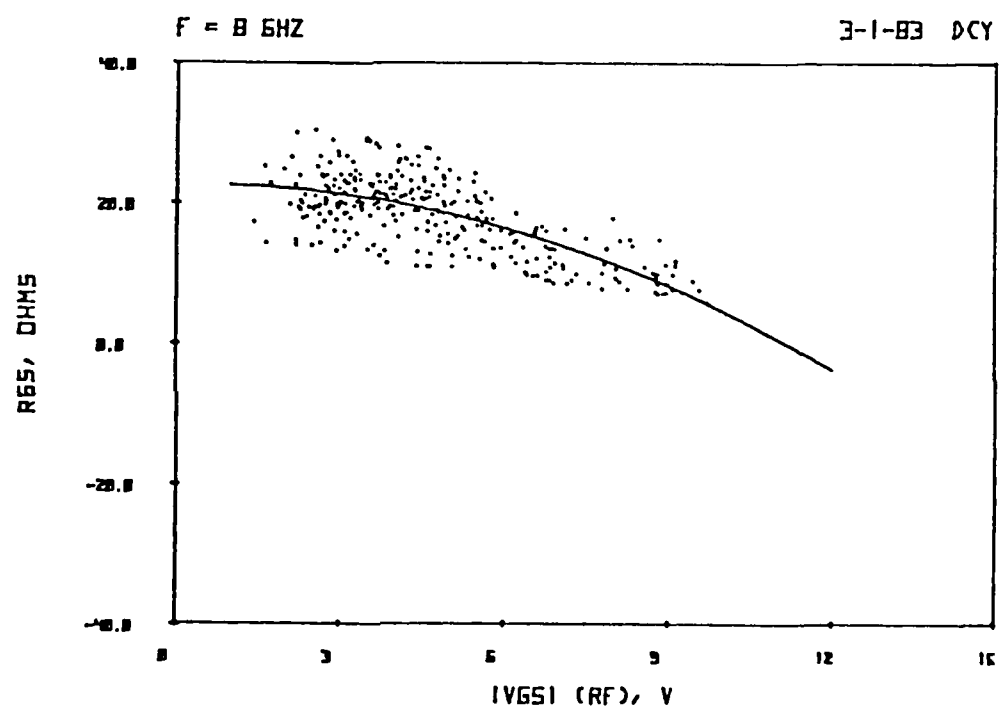


Fig. B.1 Curve Fitted R_{gs} vs. RF Voltage $|V_{gs}|$ at 8 GHz.

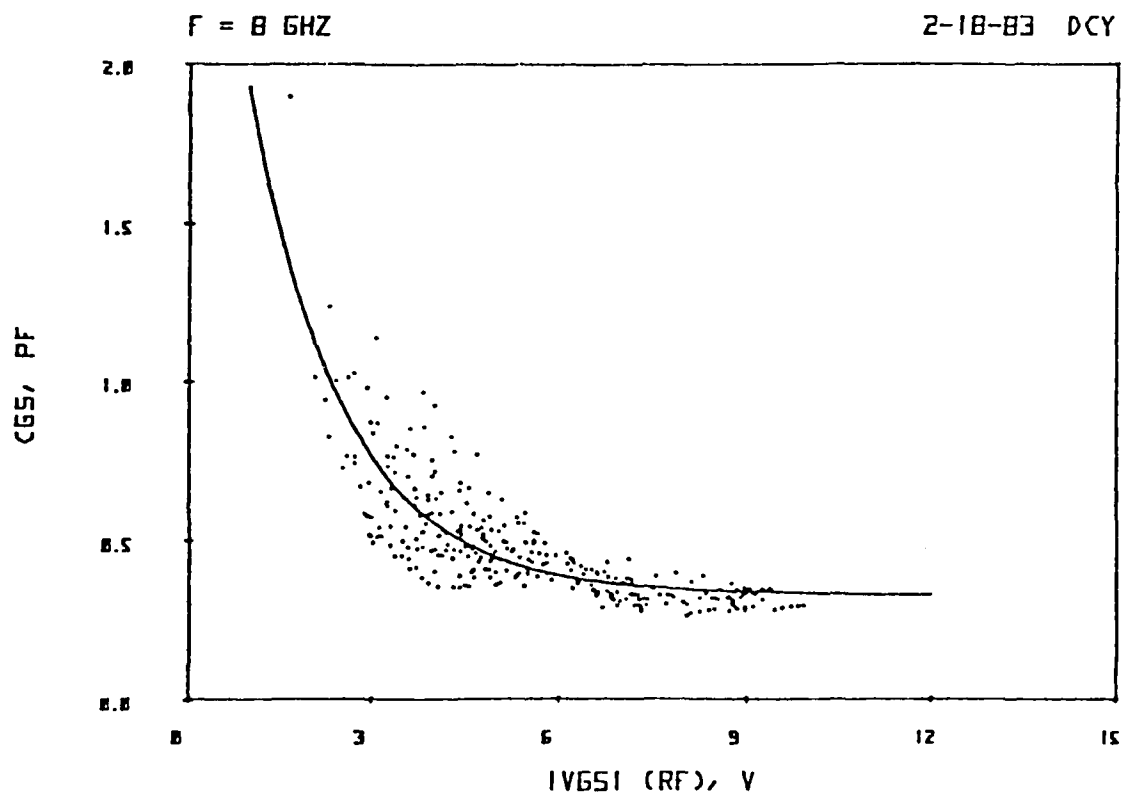


Fig. B.2 Curve Fitted C_{gs} vs. RF Voltage $|V_{gs}|$ at 8 GHz.

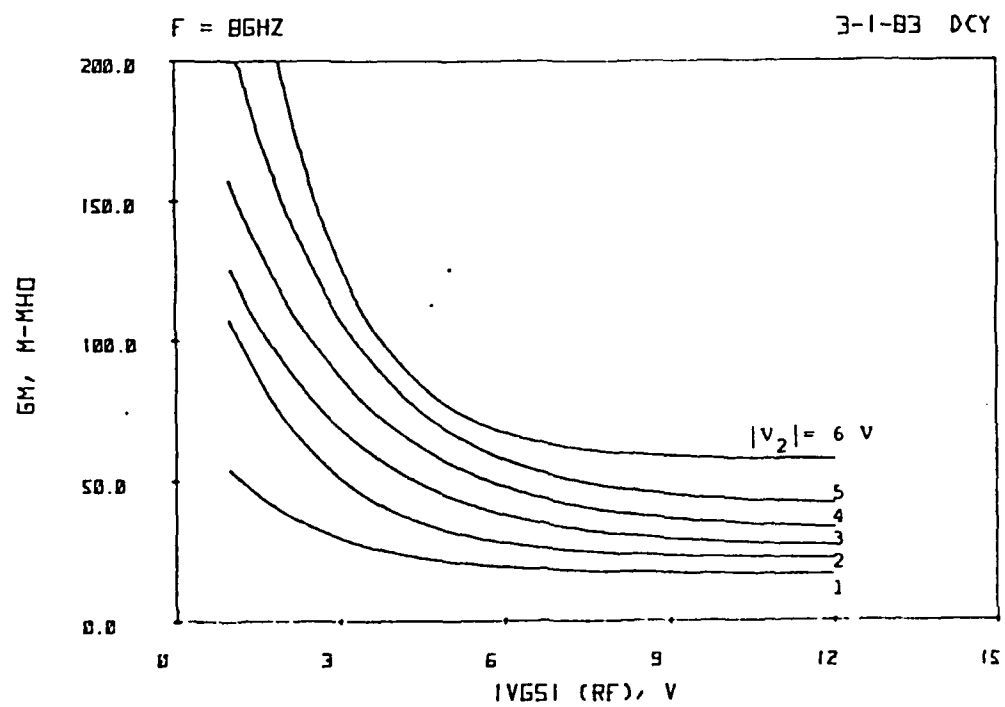


Fig. B.3 Curve Fitted g_m vs. RF Voltage $|V_{gs}|$ at 8 GHz.

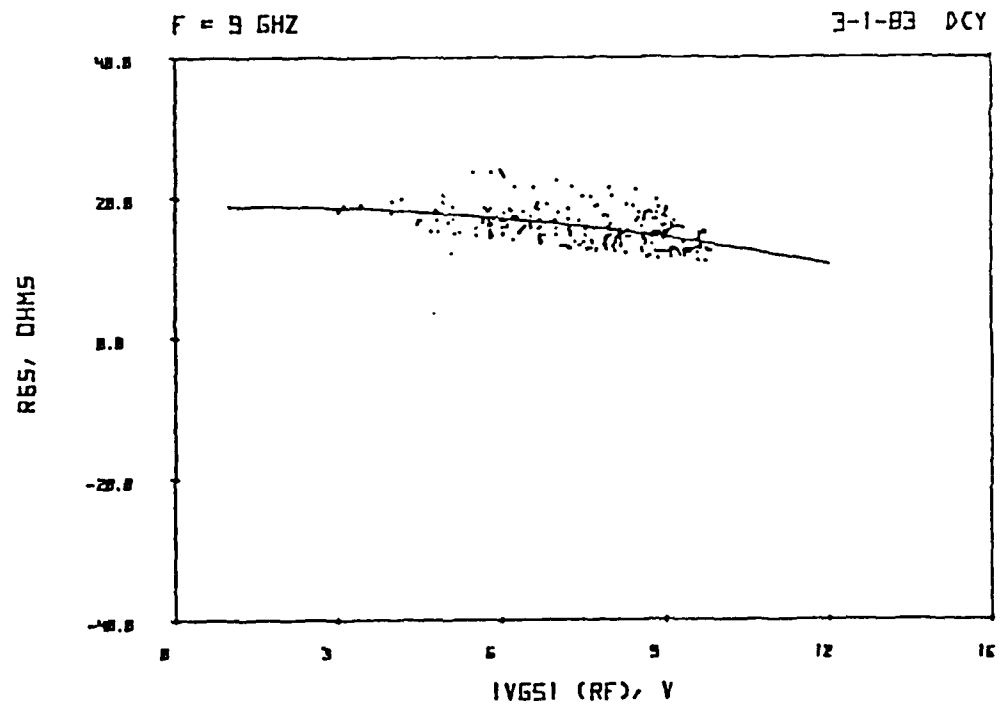


Fig. B.4 Curve Fitted R_{gs} vs. RF Voltage $|V_{gs}|$ at 9 GHz.

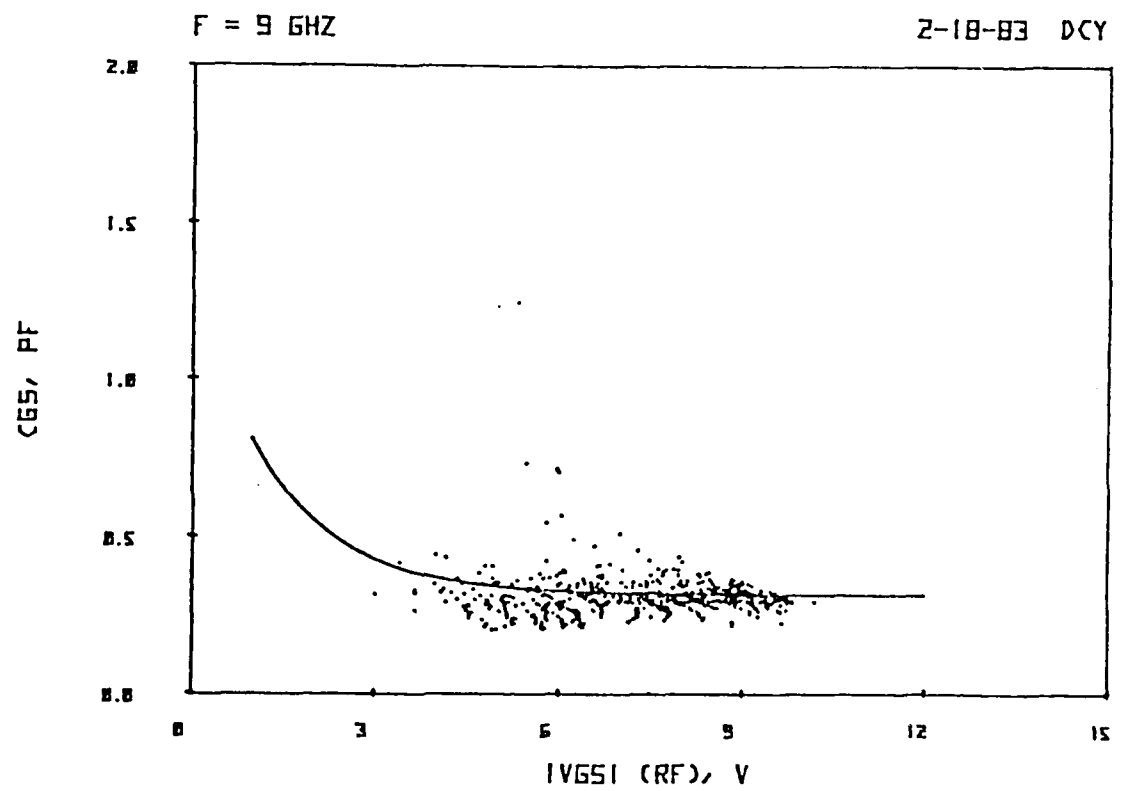


Fig. B.5 Curve Fitted C_{gs} vs. RF Voltage $|V_{gs}|$ at 9 GHz.

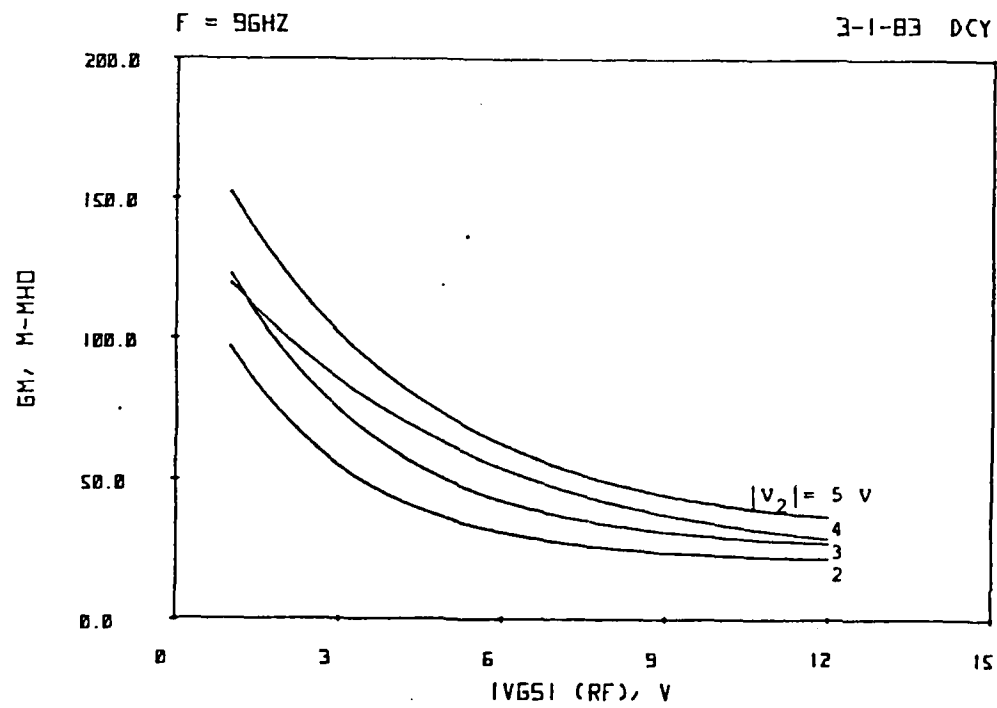


Fig. B.6 Curve Fitted g_m vs. RF Voltage $|V_{gs}|$ at 9 GHz.

REFERENCES

1. Basawapatna, G. R. and Stancliff, R. B., "A Unified Approach to the Design of Wide-Band Microwave Solid-State Oscillators," *IEEE Trans. on Microwave Theory and Techniques*, vol. MTT-27, No. 5, pp. 379-385, May 1979.
2. Camisa, R. L. and Sechi, F. N., "Common-Drain Flip-Chip GaAs FET Oscillators," *IEEE Trans. on Microwave Theory and Techniques*, vol. MTT-27, No. 5, pp. 391-394, May 1979.
3. Kotzebue, K. L., "Microwave Amplifier Design with Potentially Unstable FET's," *IEEE Trans. on Microwave Theory and Techniques*, vol. MTT-27, No. 1, pp. 1-3, January 1979.
4. Trew, R. J., "Design Theory for Broad-Band YIG-Tuned FET Oscillator," *IEEE Trans. on Microwave Theory and Techniques*, vol. MTT-27, No. 1, pp. 8-14, January 1979.
5. Papp, J. C. and Koyano, Y. Y., "An 8-18 GHz YIG-Tuned FET Oscillator," *IEEE Trans. on Microwave Theory and Techniques*, vol. MTT-28, No. 7, pp. 762-767, July 1980.
6. Abe, H. and Aono, Y., "11 GHz GaAs Power MESFET Load-Pull Measurements Utilizing a New Method of Determining Tuner Y Parameters," *IEEE Trans. on Microwave Theory and Techniques*, vol. MTT-27, No. 5, pp. 394-399, May 1979.
7. Nakatani, M., Kadowaki, Y. and Ishii, T., "A 12 GHz 1-W GaAs MESFET Amplifier," *IEEE Trans. on Microwave Theory and Techniques*, vol. MTT-27, No. 12, pp. 1066-1070, December 1979.
8. Zemack, D., "A New Load Pull Measurement Technique Eases GaAs FET Characterization," *Microwave J.*, vol. 23, No. 11, pp. 63-67, November 1980.
9. Sechi, F. N., "Design Procedure for High-Efficiency Linear Microwave Power Amplifiers," *IEEE Trans. on Microwave Theory and Techniques*, vol. MTT-28, No. 11, pp. 1157-1163, November 1980.
10. Ho, P. T., "A 7-Watt C-Band FET Amplifier Using Serial Power Combining Techniques," *1978 IEEE MTT-S Int. Microwave Symp. Digest, Ottawa, ON*, pp. 142-144, June 1978.

11. Cusack, J., "Automatic Load Contour Mapping for Microwave Power Transistor," *IEEE Trans. on Microwave Theory and Techniques*, vol. MTT-22, No. 12, pp. 1146-1152, December 1974.
12. Rauscher, C. and Willing, H. A., "Simulation of Nonlinear Microwave FET Performance Using a Quasi-Static Model," *IEEE Trans. on Microwave Theory and Techniques*, vol. MTT-27, No. 10, pp. 834-840, October 1979.
13. Willing, H. A., Rauscher, C. and DeSantis, P., "A Technique for Predicting Large-Signal Performance of a GaAs MESFET," *IEEE Trans. on Microwave Theory and Techniques*, vol. MTT-26, No. 12, pp. 1017-1023, December 1978.
14. Rauscher, C. and Willing, H. A., "Design of Broad Band GaAs FET Power Amplifiers," *IEEE Trans. on Microwave Theory and Techniques*, vol. MTT-28, No. 10, pp. 1054-1059, October 1980.
15. Willing, H. A., Rauscher, C. and DeSantis, P., "A Technique for Predicting Large-Signal Performance of a GaAs MESFET," *1978 IEEE MTT-S Int. Microwave Symp. Digest, Ottawa, ON*, pp. 132-134, June 1978.
16. Honjo, K., Takayama, Y. and Higashisaka, A., "Broad Band Internal Matching of Microwave Power GaAs MESFET's," *IEEE Trans. on Microwave Theory and Techniques*, vol. MTT-27, No. 1, pp. 3-8, January 1979.
17. Rauscher, C., "Optimum Large-Signal Design of Fixed-Frequency and Varactor-Tuned GaAs FET Oscillators," *1980 IEEE MTT-S Int. Microwave Symp. Digest, Washington, DC*, pp. 373-375, June 1980.
18. Rector, R. M. and Vendelin, G. D., "A 1.0 Watt GaAs MESFET Oscillator at X-Band," *1980 IEEE MTT-S Int. Microwave Symp. Digest, Washington, DC*, pp. 145-146, June 1980.
19. Mitsui, Y., Nakatani, M. and Mitsui, S., "Design of GaAs MESFET Oscillator Using Large-Signal S-Parameters," *1977 IEEE MTT-S Int. Microwave Symp. Digest, San Diego, CA*, pp. 270-272, June 1977.
20. Mitsui, Y., Nakatani, M. and Mitsui, S., "Microwave MESFET Oscillator Design Using Large-signal Scattering Parameter," *IEEE Trans. on Microwave Theory and Techniques*, vol. MTT-25, No. 12, pp. 981-984, December 1977.
21. Scanlan, S. O. and Young, G. P., "Error Considerations in the Design of Microwave Transistor Amplifiers," *IEEE Trans. on Microwave Theory and Techniques*, vol. MTT-28, No. 11, pp. 1163-1169, November 1980.

22. Johnson, K. M., "Large-Signal GaAs MESFET Oscillator Design," *IEEE Trans. on Microwave Theory and Techniques*, vol. MTT-27, No. 3, pp. 217-227, March 1979.
23. Mazumder, S. R. and Van Der Puije, P. D., "'Two-Signal' Method of Measuring the Large-Signal S-Parameters of Transistors," *IEEE Trans. on Microwave Theory and Techniques*, vol. MTT-26, No. 6, pp. 417-420, June 1978.
24. Berglung, C. D., "Large-Signal Characterization, Amplifier Design, and Performance of K-Band GaAs MESFETS," Tech. Report No. 586, Lincoln Laboratory, Massachusetts Institute of Technology, Lexington, December 11, 1981.
25. Yang, D. C. and Peterson, D. F., "Large-Signal Characterization of Two-Port Nonlinear Active Networks," *1982 IEEE MTT-S Int. Microwave Symp. Digest, Dallas, TX*, pp. 345-347, June 1982.
26. "Semi-Automatic Measurements Using the 8410B Microwave Network Analyzer and the 9825A Desk Top Computer," *HP Application Note 221, Hewlett Packard Company, Palo Alto, CA*, 1978.
27. Bauer, R. F. and Panfield, P., "De-Embedding and Unterminating," *IEEE Trans. on Microwave Theory and Techniques*, vol. MTT-22, No. 3, pp. 282-288, March 1974.
28. Tajima, Y., Wrona, B. and Mishima, K., "GaAs FET Large-Signal Model and Its Application to Circuit Design," *IEEE Trans. on Electron Devices*, vol. ED-28, No. 2, pp. 171-175, February 1981.
29. Madjar, A. and Rosenbaum, F. J., "A Large-Signal Model for the GaAs MESFET," *IEEE Trans. on Microwave Theory and Techniques*, vol. MTT-29, No. 8, pp. 781-788, August 1981.
30. Peck, D. E. and Peterson, D. F., "A Measurement Method for Accurate Characterization and Modeling of MESFET Chips," *1981 IEEE MTT-S Int. Microwave Symp. Digest, Los Angeles, CA*, pp. 310-312, June 1981.
31. Churchill, R. V., "Complex Variable and Applications," Second Edition, *McGraw Hill Book Company, Inc., New York*, 1960.

END

FILMED

8 24

10-11-10